AUTOMATED COMPUTATIONAL THERMOCHEMISTRY AND KINETICS FOR COMBUSTION

by

SARAH N. ELLIOTT

(Under the Direction of Henry F. Schaefer III)

ABSTRACT

Recent progress in theoretical methodologies and computational capabilities make highly-predictive, thermochemical kinetics computations possible. The foundation for these calculations is reliable fundamental properties for the reactants, products, and intermediates in a system, obtained with quantum chemistry methods. This dissertation provides an overview on common approaches to characterize a reaction system and demonstrates a high-level approach to quantum mechanics calculations through a study of the formylperoxy radical and kinetics computations through addition reactions of stabilized Criegee Intermediates. Carrying out these intensive protocols, however, is not manually feasible for a full combustion simulation. We describe Autochem: a large-scale, automated, combustion chemistry modeling software package that we have been developing over the last three years. It accurately predicts the thermochemical properties and temperature and pressure dependence of the thousands of gas phase reactions in a combustion mechanism by providing a unified interface for electronic structure and transition state theories, mechanism generation, classical trajectory simulations, the master equation, and uncertainty quantification methods. This dissertation showcases two studies that employ Autochem. The first uses the software to model branching ratios during the pyrolysis of arbitrary fuels. The second focuses on thermochemistry of core

combustion species. It benchmarks common electronic structure methods and several high-level treatments of a partition function.

INDEX WORDS: [combustion chemistry, atmospheric chemistry, thermochemistry, kinetics, computational chemistry, quantum chemistry, electronic structure theory, transition state theory, partition function, peroxy radical chemistry, stabilized Criegee intermediates]

AUTOMATED COMPUTATIONAL THERMOCHEMISTRY AND KINETICS FOR COMBUSTION

by

SARAH N. ELLIOTT

B.S., Bethel University, 2015

A Dissertation Submitted to the Graduate Faculty of the
University of Georgia in Partial Fulfillment of the Requirements for the Degree.

DOCTOR OF PHILOSOPHY

ATHENS, GEORGIA

2020

AUTOMATED COMPUTATIONAL THERMOCHEMISTRY AND KINETICS FOR COMBUSTION

by

SARAH N. ELLIOTT

Major Professor:	Henry F. Schaefer III
Committee:	Geoffrey Smith
	Henning Meyer

Electronic Version Approved:

Ron Walcott
Interim Dean of the Graduate School
The University of Georgia
May 2020

ACKNOWLEDGEMENTS

I wish to recognize the many incredible people who have propelled me forward in my pursuit of a doctorate degree and those who have helped me to gain confidence in my research. My parents David and Andrea and siblings Becky and Eric have been along for the entire ride. I am thankful that they exhibited and instilled in me the values of hard work, integrity, and intellectual curiosity.

My professors at Bethel University were instrumental towards developing my passion for science. I would like to acknowledge Profs. Beecken, Greenlee, Hoyt, Maddox, Neibergall, Neiwart, Rohly, Stein, and Winters and especially thank Profs. King and Lindquist who mentored me through my first research experiences. I would also like to acknowledge the extraordinary community of peers at Bethel University, and namely Andi Cragoe, Lauren Lahm, Angela Pascarella, and Ayriel Ash who kept me sane, or perhaps accompanied me in insanity, during the many hours in the labs and libraries.

Prof. Henry Schaefer III has been an incredible research advisor during my time at the University of Georgia. I would like to acknowledge the role my fellow research group members have had in making my graduate experience so positive – thank you to Adam, Andrew, Boyi, Bryan, Gustavo, Jared, Jonathon, Jonathon, Kevin, Matt, Mark, Megha, Michael, Mitchell, Preston, Dr. Turney, Walter, Xiao, and Zhi. I am particularly grateful for the camaraderie from Kevin Moore, Andreas Copan, Marissa Estep, Avery Weins, and James Morgan whom I count as both wonderful mentors

and dear friends. I appreciate the education I've received, as well, from Profs. Allen, Meyer, and Smith. I would also like to thank administrative staff who have saved me stress countless times: Amanda, Lauren, Kathryn, Kistie, and Sybil.

The Department of Energy Graduate Fellowship has been incredibly generous to me both financially and with opportunities. Through it I was able to discover my passion in computational thermochemistry and kinetics by working with the Chemical Science and Engineering division at Argonne National Laboratory. I would like to thank several members of the division: Drs. Klippenstein, Georgievskii, and Jasper. Finally I would like to thank the generosity of the ARCS Foundation.

CONTENTS

LIST OF FIGURES

LIST OF TABLES

CHAPTER 1

INTRODUCTION AND LITERATURE REVIEW

Combustion is the most important means of releasing stored energy. The sheer prevalence of and universal reliance on combustion processes escalate the need to track these pathways. Atmospheric impacts associated with the combustion process can be mitigated, and engine efficiency can be improved, if a combustion mechanism is properly understood and designed.

Each mechanism for a combustion process is comprised of its elementary chemical reactions, and their rate constants, as well as the thermodynamic and transport properties for each involved species. The mechanism is only as reliable as these parameters that constitute it. Many of the chemical intermediates in these chain branching reactions, however, are very transient in nature. For this reason, experimental study is proven difficult, especially at the high temperatures and pressures that are relevant to practical combustion devices. The massive number of reactions present in each combustion mechanism enlarges the hurdle. As such, significant ambiguity and uncertainty still exist in current combustion modeling.

Computational chemistry provides the wherewithal to study the combustion process. Recent progress in theoretical methodologies and computational capabilities has propelled the transforma-

tion of chemical kinetics computations from largely empirical to highly predictive. As a result, the fidelity of combustion modeling can dramatically improve.

1.1 Dissertation Structure

We are building a large-scale, high-level, and automated combustion chemistry modeling software package to facilitate the advancement of computational thermochemistry and kinetics. Through a series of drivers, this code provides a unified interface for mechanism generation, electronic structure theory, transition state theory, classical trajectory simulations, the master equation, and uncertainty analysis tools. The remaining sections of this introductory chapter, CHAPTER 1, deliver a brief overview of common approaches to these tasks. Each is, in itself, a tremendous undertakings. For instance, electronic structure calculations for combustion systems, which are largely made up of radical molecules, must be done carefully. CHAPTER 2 is a study on one such system.

CHAPTER 2

CHAPTER 2 in this dissertation is a study that characterizes the formylperoxy radical – an important combustion intermediate found in the atmosphere. In it, we see that, when done properly, electronic structure theory can solve disagreements in experimental studies. We also see the large number of calculations that are required to achieve reliable extrapolations and corrections on electronic energies, accurate diagnostics, and fundamental frequencies. This motivates our automation efforts. In a combustion system, the interconversion between two conformers of a peroxy radical is just one of thousands of reaction pathways that need to be accurately computed. As such, a combustion simulation undergoes a tremendous amount of quantum chemistry calculations, alone.

The most important conclusion to draw from CHAPTER 2, though, is that the success of this study demonstrates the ability of modern quantum chemistry techniques to achieve the accuracies on fundamental properties required to pursue predictive thermochemistry and kinetics.

CHAPTER 3

The focus of CHAPTER 3 is on demonstrating computational kinetics. It reviews two studies on addition reactions of stabilized Criegee Intermediates, one with ammonia and one with methanol. Criegee intermediates are significant to many hydrocarbon combustion pathways and their addition to atmospheric molecules, like those in these studies, have an important role in the composition of the atmosphere. These build upon the types of quantum chemistry computations demonstrated in CHAPTER 2 to calculate temperature dependent rate constants. Analogous to the computation of fundamental properties with quantum chemisry techniques, there are many steps to accurately compute thermochemical and kinetic parameters. These studies, for instance, carried out several techniques that will be described later in this chapter – e.g. hindered rotor treatment, intrinsic reaction coordinate analysis, and tunneling corrections – alongside the robust electronic structure calculations.

CHAPTER 4

The large number of calculations necessary to produce reliable thermochemical and kinetic parameters for even a single reaction pathway mean that it will prove difficult to manually investigate more than a few reactions at a time. CHAPTER 4, in turn, describes the workflow of Autochem as it carries out those tasks automatedly. The software, in its current state, can accurately predict the temperature and pressure dependence of the thousands of gas phase reactions in a combustion mech-

anism. The goal of the paper presented in CHAPTER 4 is to demonstrate the plethora of methods available to an Autochem user and the success of the Autochem program applied to pyrolysis.

CHAPTER 5

CHAPTER 5 presents a study that solves the thermochemistry for a set of > 300 core combustion molecules. Because it does so through the Autochem software, the study can automate the computations with a wide variety of electronic structure methods and approaches to building a partition function. This enables an analysis on cost-saving routines and a commentary on the performance of many commmon methods. The benchmark on methods of the study will aid future thermochemical study. The final database on core combustion molecules will provide the combustion community a reliable foundation with which to parameterize combustion models.

1.2 An Overview of Computational Thermochemistry

The first step towards determining thermochemistry of a molecule is to search for its stationary points. Quantum Chemistry (QC) methods provide a reliable means to find the geometries, energies, and rovibrational properties that parameterize the equations of SM used to calculate thermochemical properties. The bridge between QC and thermochemical properties is the Statistical Mechanics (SM) molecular partition function. Heat capacities, entropies, enthalpies, and free energies can be determined from various temperature derivatives of the partition function.

1.2.1 Quantum chemistry and *ab initio* electronic structure theory

Locating the minimum geometries on a potential energy surface for a species requires a description of the atom positions set in coordinate system, usually Cartesian or internal. At lowest level the

coordinates can be predicted with classical force fields or by computing energies using an affordable quantum chemical method at geometries chosen with a stochastic sampling or surface scan. At a higher level, the derivative of the species' energy with respect to the position of its atoms, which is known as the gradient, may be used with numerical methods (e.g. Newton-Raphson) to walk down the PES towards the stationary point. Once a stationary point is located, the Hessian matrix – or, the second derivatives of the energy to the atom positions – gives the curvature, which will identify if the coordinates describe a minimum. This Hessian matrix also provides the information required for a harmonic vibrational analysis. The affordable quantum chemical method of choice is typically density function theory (DFT).

Once a minimum is located, more rigorous methods are applied at that single point to solve for reliable energetics. Historically, computationalists have aimed to have uncertainties within thermochemical accuracy, which is 1 kcal mol^{-1} . This is possible by solving the energy with Hartee-Fock and treating the electron correlation perturbatively (MP2, MP3, MP4, ...), with configuration interaction (CIS, CISD, CISDT, ..., FCI) methods, or with coupled cluster (CCSD, CCSD(T), CCSDT, ...) methods. The most prevalent of these is the coupled cluster singles, doubles, and perturbative triples methods, which is often considered the gold standard.

Recently, the *ab initio* electronic structure community has heightened expectations for accuracy. This is largely due to the development of composite and extrapolation energy schemes. Methods such as the W4 [62], HEAT [48], and the Focal Point Approach [56] can yield uncertainties around 1 kJ mol^{-1} or less. When approaching this level of accuracy, the geometry is usually optimized on the CCSD(T) energy surface after the lower level DFT optimization. This allows for harmonic frequencies to be obtained at the CCSD(T) level as well. The single point energies are then solved with complete basis set extrapolations and corrections accounting for the effects of higher order

electronic excitations (such as the $\Delta_{T(Q)}$ correction for coupled-cluster methods [84]), vibrational anharmonicity (using second order vibrational perturbation theory, VPT2 [93], or vibrational configuration interaction, [139]), core-valence interactions (via a lower level all-electron energy minus frozen-core energy), scalar-relativistic effects (with X2C or Douglas-Kroll Hamiltonians [53, 142]), and adiabatic behavior (applying the diagonal Born-Oppenheimer correction [112]).

The absolute energies obtained during the *ab initio* electronic structure calculation need to be translated into heats – or enthalpies – of formation at 0 K, ΔH_{0K}. The most common method uses an atomic basis set to do so. In this case, the energy (including the zero-point vibrational energy, ZPVE) of each atom, calculated at the same level of theory as the target molecule, is subtracted from a reliable enthalpy, which is usually obtained experimentally. The result is multiplied by the number of times the atom appears in a molecule. This quantity, for each atom that constitutes the molecule, is subtracted from the absolute energy of the molecule to approximate the heat of formation. A better description of the heat of formation uses a molecular basis set instead of atomic. This better describes, or error cancels, the bonding character of the target molecule. Common approaches to this are the Generalized Bond Separation Reaction schemes and Connectivity Based Hierarchy[106, 138].

1.2.2 Partition functions

The molecular partition function describes the distribution of energy levels. More specifically, it indicates the number of states that are accessible to a molecule at a given temperature. A dependable partition function is essential not only for predicting the thermochemical properties of a single species, but also for describing the temperature dependence of the rate constant of a reaction. The latter will be discussed in section II.2. Entropies (S), heat capacities (C), and enthalpies (H) can be

found by taking temperature (T) derivatives of the partition function, Q (where k_B is the Boltzmann factor, N is Avogadro's number, and R is the gas constant).

$$S = \mathrm{N}k_\mathrm{B}\left[\frac{\partial}{\partial T}(T\ln Q) - \ln \mathrm{N} + 1\right]$$
$$C_v = \mathrm{N}k_\mathrm{B}\frac{\partial^2}{\partial T^2}(T\ln Q)$$
$$H(T) - H(0) = \frac{\mathrm{R}T^2}{Q}\frac{\partial Q}{\partial T} + \mathrm{R}T$$

The simplest description of a partition function relies on the rigid-rotor harmonic (RRHO) assumption. With it, the motions – or, degrees of freedom – for the molecule are fully separable in order to approximate the molecular partition function as the multiplicative combination of the vibrational, rotational, translational, and electronic partition functions. The RRHO partition function is sensitive to the electronic structure method used, because the energy levels found for both the electronic and vibrational partition functions depend on the method. Different levels of *ab initio* theory can easily cause factors of two changes in the partition function [65]. Computational methods for the electronic energy level have already been discussed in section 1.2.1.

A common improvement to the RRHO partition function is treating the vibrational anharmonicity. While in kinetics, which depends on ratio of partition functions, the effect of anharmonicity often cancels out, in absolute thermochemistry it may cause error at a factor of 1.03^n, where n is the number of vibrational degrees of freedom [57]. An improved description of the vibrational anharmonicity would require computing higher order derivatives of the energy of a species with respect to its atomic positions. The anharmonicity may then be described by approximating to the anharmonic vibrational frequencies with methods like VPT2. Alternatively, the anharmonic x-matrix can be a direct parameter when computing the partition function [144].

Similarly, accurate treatment of the torsional modes plays a large effect on the vibrational partition function. The separability of the vibrational modes, that RRHO assumes, begins to break down when there are large amplitude motions, which usually occur along the internal rotor modes. The simplest, improved description is to hold the assumption that all modes are separable, and then treat the rotor modes as free internal rotors; there are simple analytic expressions for their partition function. Many rotors, however, are hindered. At low and high temperatures, one-dimensional treatment of a hindered torsional mode is often effective. Each rotor's energy profile, in this treatment, is either approximated as a cosine function or computed by finding the configuration's energy after incrementing its angle and performing either a relaxed or constrained optimization. This profile is used in the molecular partition function and the rotor's corresponding frequency is projected out of the Hessian matrix so it no longer contributes directly to the vibrational partition function [143]. At intermediate temperatures, when there is significant coupling between different torsional modes, or when the frequencies of non-torsional modes may be strongly impacted by altering the torsional configuration, the one-dimensional hindered rotor treatment may not be sufficient. CHAPTER 3 discusses alternative partition functions for these cases.

1.3 An Overview of Computational Kinetics

To achieve rate constants for each chemical transformation in a combustion process, QC must locate the stationary points along its reaction pathway or potential energy surface (PES). This determines the reaction barrier. Transition state theory (TST) and SM can then calculate temperature dependent rate coefficients for each reaction. We will discuss both pressure independent and pressure dependent rate constants. Many abstraction and addition reactions are largely independent

of pressure. Their rate coefficient, k, can be determined with canonical TST, which gives the high-pressure limit of the rate constant.

$$k(T) = \kappa \frac{\mathrm{k_B} T}{\mathrm{h}} \frac{Q^{\dagger}}{Q_{reacs}} \exp \frac{\Delta E}{\mathrm{k_B} T}$$

The Boltzmann, tunneling, and Plank factors are $\mathrm{k_B}$, κ, and h, respectively. The Boltzmann factor, in effect, accounts for the probability of having enough energy to cross the barrier of height ΔE. The reactant partition functions, $\mathrm{Q_{reacs}}$, is described in the previous section. For the transition state partition function, $\mathrm{Q}^{\dagger}$, the vibrational mode along the reactant coordinate, i.e. the imaginary frequency, is not included in the vibrational partition function. Thus, identifying the correct transition state geometry, energy, and partition function is essential to predicting a correct reaction rate of the reaction.

The search for a transition state structure can follow geometry optimization procedures described in section 1.2.1, where the Hessian matrix should correspond to the curvature of a saddle point instead of a well. The resulting imaginary mode will describe the motion along the reactant coordinate. A subsequent intrinsic reactant coordinate (IRC) [39] computation can validate that the transition state does, indeed, connect the reactants to the products. This computation finds single point energies along the steepest descent path down from a transition state on a potential energy surface.

The saddle point does not always, however, perfectly correspond to the transition state. The proper definition of the transition state is the dividing surface that separates reactants from products and minimizes the reactive flux crossing it [122]. When the barrier is flat, or at high temperatures, the effects of changing entropy may influence the position of minimum flux. Variational TST

(VTST) computes frequencies at points along the reaction path surrounding the saddle point. There, the partition functions are evaluated and VTST can identify the true dividing surface.

In some instances, the barrier for a bimolecular reaction is actually submerged below that of the reactants. In this case, there must be two (or more) transition states contributing to the kinetics [44]. In addition to the transition state described previously, which determines the chemical transformation, these reactions have a long-range transition state that corresponds to the formation of a weak van der Waals complex. For these systems, a steady state analysis is necessary to describe the flow from the reactants through the stabilized complex and over the reaction barrier.

The remaining parameter for the pressure independent, temperature dependent, rate constants is the tunneling factor, κ. The simplest correction is that of Wigner [140], which depends only on the imaginary frequency of the saddle point. The Eckart correction improves on this by including an estimate for the barrier curvature and the reaction energies [59]. By including energy calculations along the reaction coordinate, i.e. IRC computation, treatments like small curvature, large curvature, and WKB tunneling corrections are possible [38, 114].

Pressure dependence is achieved through the Master Equation. Small molecules can deviate significantly from the high-pressure limit when at low pressure and high temperature. This is because the rate of collision between an excited molecule and its bath gas effects the distribution of its energy states, and thereby its rate constant. When at high pressures, a simple Boltzmann distribution can describe the thermal equilibration. At lower pressures, the collision rates may not be high enough to maintain the distribution. The master equation provides a physically correct treatment of the reaction process by incorporating a microcanonical rate constant, collision frequency, and energy transfer model. Common approaches to the collision frequency are the hard sphere model or Lennard-Jones potential. The collisional energy transfer is typically evaluated with empirical pa-

rameters or classical trajectory simulations. RRKM theory provides a microcanonical approach to the rates, which equilibrates the reactants in a fixed-total-energy ensemble. The rate computed with RRKM will collapse into the canonical TST result when integrating over a Boltzmann distribution for reactants [122].

CHAPTER 2

THE *cis*- AND *trans*-FORMYLPEROXY RADICAL: FUNDAMENTAL VIBRATIONAL FREQUENCIES AND RELATIVE ENERGIES OF THE $\tilde{X}^2A''$ AND $\tilde{A}^2A'$ STATES[1]

[1]Elliott, S. N.; Turney, J. M; and Schaefer, H. F. 2015. *RSC Advances*, 5 (130), 107254-107265. Reprinted with permission of the publisher.

2.1 Abstract

Acylperoxy radicals [RC(O)OO$^\bullet$] play an important catalytic role in many atmospheric and combustion reactions. Accordingly, the prototypical formylperoxy radical [HC(O)OO$^\bullet$] is characterized here using high-level *ab initio* coupled-cluster theory. Important experiments have been carried out on this system, but have not yet comprehensively described the properties of even the ground electronic state structure. We report *cis* and *trans* geometries for the ground ($\tilde{X}\,^2A''$) and first excited ($\tilde{A}\,^2A'$) state equilibrium conformers and the torsional saddle point on the ground state surface at the CCSD(T)/ANO2 level of theory. Relative energies of these ground- and excited-state stationary points were obtained using coupled cluster theory with up to perturbative quadruple excitations, extrapolated from the sextuple zeta basis set to the complete basis set limit. These methods predict conformational energy differences ΔE(*trans*-$\tilde{X}$ $\rightarrow$*cis*-$\tilde{X}$) = 2.35 kcal mol^{-1} and ΔE(*trans*-$\tilde{A}$ $\rightarrow$*cis*-$\tilde{A}$) = $-$2.95 kcal mol^{-1}. On the $\tilde{X}$ surface, the transition state for the conformational change lies 8.09 kcal mol^{-1} above the *trans* ground state minima. The adiabatic electronic excitation energies from the ground state isomers are predicted to be of 18.17 $\pm$ 0.10 (*trans*) and 13.03 $\pm$ 0.10 kcal mol^{-1} (*cis*). The former is in excellent agreement with the 18.1 $\pm$ 1.4 kcal mol^{-1} transition found by Lineberger and coworkers. Additionally, transition properties between the $\tilde{X}\,^2A''$ and $\tilde{A}\,^2A'$ states are reported for the first time, using the equation of motion (EOM)-CCSD method, which predicts lifetimes for *trans*-$\tilde{A}\,^2A'$ HC(O)OO$^\bullet$ of 5.4 ms and *cis*-$\tilde{A}\,^2A'$ HC(O)OO$^\bullet$ of 20.5 ms. Second-order vibrational perturbation theory was utilized to elucidate the fundamental frequencies at the CCSD(T)/ANO2 level of theory for the *cis* and *trans* conformers of the $\tilde{X}$ and $\tilde{A}$ states and five ground state isotopologues of both conformers: H^{13}C(O)OO$^\bullet$, HC(^{18}O)OO$^\bullet$, HC(O)^{18}O^{18}O$^\bullet$, DC(O)OO$^\bullet$, and DC(O)^{18}O^{18}O$^\bullet$. These studies provide high accuracy predictions of vibrational

frequencies that have large experimental uncertainties and disagreements. Furthermore, we characterize experimentally unassigned vibrational frequencies and transition properties.

2.2 Introduction

The formyl radical ($HC^{\bullet}O$) is a chain branching intermediate produced during methane oxidation, a common process in fuel combustion and in the lower atmosphere. In the early stages of the oxidative process, $HC^{\bullet}O$ is formed from formaldehyde – either by photodissociation, or via reaction with a variety of open-shell species.[26, 32, 82, 104, 121] The nature of formyl radical reactivity is relevant to understanding atmospheric chemistry in polluted environments due to its liberation of $H^{\bullet}$ to yield CO and the reaction of $H^{\bullet}CO$ with O_2 to furnish $HO_2{}^{\bullet}$. The current research is concerned with characterization of the formylperoxy radical, an intermediate in the latter reaction, shown explicitly below (Reaction R1). [82, 121]

$$HC^{\bullet}O + O_2 \longrightarrow [HC(O)OO^{\bullet}] \longrightarrow HO_2{}^{\bullet} + CO \qquad \text{(R1)}$$

Interest in R1 is derived from the harmful effects of its product $HO_2{}^{\bullet}$, which is known to propogate photochemical smog throughout the troposphere.[31, 96] Osif and Heicklen (1976) were the first to experimentally investigate $HC(O)OO^{\bullet}$ as an intermediate in R1 (Ref. [99]) following observation of the $HO_2{}^{\bullet}$ product via laser magnetic resonance spectroscopy of formyl radical oxidation.[105] Their support of an $HC(O)OO^{\bullet}$ intermediate, through gas chromotography monitored formaldehyde irradiation, was quickly followed by both spectroscopic and theoretical reports.[33, 73, 123] Infrared spectroscopy on formaldehyde in solid oxygen displayed absorption peaks at 1790 and 1090 cm^{-1}. [123] The experimentalists, Lee and Diem, attributed these peaks to $HC(O)OO^{\bullet}$ formed dur-

ing reaction R1. Unscaled restricted Hartree Fock (RHF) computations with the 6-31G(*d,p*) basis set found these to originate from the C=O and C–O stretching motions of *trans*-HC(O)OO$^\bullet$.[33]

These early results concerning R1 were expanded upon using the G2M restricted coupled cluster (RCC) composite method, along with Rice-Ramsperger-Kassel-Marcus (RRKM) theory for kinetic rate predictions.[50] Hsu, Mebel, and Lin concluded that the major channel proceeds through the *trans*-HC(O)OO$^\bullet$ association product in a concerted manner to $HO_2^\bullet$ and CO. [4, 50, 73, 146] Alternatively, the hydrogen of *trans*-HC(O)OO$^\bullet$ may migrate from the carbon to the terminal oxygen, forming an $^\bullet$C(O)OOH transition state, before dissociating to CO_2 and HO$^\bullet$ or, 35 kcal mol^{-1} less favorably, to $HO_2^\bullet$ and CO$^\bullet$ (R2).

$$\tilde{X}\,^2A'' \text{ HC(O)OO}^\bullet \longrightarrow {}^\bullet\text{C(O)OOH} \longrightarrow CO_2 + HO^\bullet \qquad \text{(R2)}$$

$$\longrightarrow CO + HO_2^\bullet$$

Though the barrier for the CO_2 and HO$^\bullet$ reaction is high, the 36 kcal mol^{-1} exothermic formation of the HC(O)OO$^\bullet$ is assumed to be sufficiently energetic to drive the reaction (possibly after progressing back through the hydroperoxo-oxomethyl radical complex).[3, 4, 91, 133] Reactions of the hydrogen migration product, hydroxyformyl radical [$^\bullet$C(O)OOH], are pivotal to low temperature autoignition chemistry,[148] and the hydroxyl radical (HO$^\bullet$) has been identified as the most important intermediate in the consumption of olefins in the atmosphere.[96]

By 1975, Winter and Goddard [141] had already proposed a different possibility for the reaction of HCO and O_2; the association may be sufficiently exothermic for internal conversion to the first excited state ($\tilde{A}\,^2A'$) HC(O)OO$^\bullet$. Upon formation, the *trans*-$\tilde{A}\,^2A'$ state of HC(O)OO$^\bullet$ undergoes

a highly exothermic (-54 kcal mol^{-1}) decomposition (R3) to CO_2 and HO$^\bullet$.

$$\tilde{A}\,^2A'\ HC(O)OO^\bullet \longrightarrow CO_2 + HO^\bullet \qquad \text{(R3)}$$

The close energy spacing between the $\tilde{X}$ and $\tilde{A}$ states of peroxy radicals often necessitates examination of both electronic states. Within the last decade, the HC(O)OO$^\bullet$ radical has been further characterized experimentally and qualitatively using density functional theory (DFT). Formylperoxy radical may exist in two conformers, with the terminal oxygen either *trans* or *cis* to the carbonyl. The *trans* isomer was predicted to be 1.9 kcal mol^{-1} lower in energy than the *cis*, with a barrier height of 8.8 kcal mol^{-1} at the B3LYP/6-311++G(*d,p*) level at 0 K.[91] To ensure that $HO_2^\bullet$ was not present in their characterization of HC(O)OO$^\bullet$, which they suspected of earlier studies, Yang, Yu, Zeng and Zhou [147] reported the infrared spectra and vibrational frequency assignments of the formylperoxy radical in an argon matrix. Aided by B3LYP and MP2 calculations with the 6-311++G(*d,p*) basis, Yang et al. reported the experimental C=O and C$-$O stretching vibrations to be 1821.5 and 957.3 cm^{-1}, and attributed them to the *trans* isomer. Recently, the isolated formylperoxy radical has been studied experimentally by Villano, Eyet, Wren, Ellison, Bierbaum, and Lineberger.[132]. Gas phase measurements have been made via photodetachment from the formylperoxy anion.[132] The experimental ν_4, ν_5, and ν_6 frequencies were found to be 1098 $\pm$ 20, 973 $\pm$ 20, and 574 $\pm$ 35 cm^{-1}, respectively and were assigned to the *trans* isomer. The gap between experimental and previous results is $\geq$50 cm^{-1} for several fundamentals. That, combined with the large uncertainty in the four experimentally measured frequencies, calls for a higher level theoretical study.

Ever-increasing interest in peroxyacyl systems provides additional motivation for HC(O)OO$^\bullet$ study. This class of molecules plays a large role in the distribution of oxygen, ozone, hydroxyl radical, and $NO_x^\bullet$ in the atmosphere.[97] Distinct from alkylperoxy radicals, peroxyacyl radicals offer inductive stabilization by the carbonyl group to peroxyacyl nitrates, facilitate HO$^\bullet$ recycling via the carbonyl oxygen, and are more abundant in the atmosphere. These attributes make the characterization of acylperoxy radicals critical to atmospheric chemistry.

Herein, we provide a characterization of the ground-state conformers of the formylperoxy radical and their $\tilde{A} \leftarrow \tilde{X}$ excitation products using high-level *ab initio* methods. The relative energies of the *cis* and *trans* conformers, and the barrier height to interconversion between them, are predicted using coupled-cluster (CC) methods extrapolated to the complete basis set (CBS) limit. Anharmonic vibrational frequencies of both structures in the ground and first excited states, including various isotopologues of the ground state, are computed for the first time, using coupled-cluster methods with second-order vibrational perturbation theory (VPT2). The structures of the excitation products of the *cis* and *trans* rotamers, their transition properties, as well as adiabatic excitation energies extrapolated to the CBS limit, are also reported.

2.3 Theoretical Methods

Computations were performed using the CFOUR [1, 47], MRCC [60], and PSI4 (Ref. [127]) programs. At the coupled cluster singles, doubles, and perturbative triples [CCSD(T)] level of theory, optimized geometries were determined for the *cis* and *trans* conformers in both the $\tilde{X}\ ^2A''$ and $\tilde{A}\ ^2A'$ states. The computations employed the correlation-consistent, polarized valence, quadruple zeta (cc-pVQZ) basis sets of Dunning[28]. Concurrently, the full atomic natural orbital (ANO)

basis set of Almlöf and Taylor, ANO2, geometries were obtained for the vibrational frequency computations.[6]. The ANO sets, while sharing nearly identical Gaussian function contraction patterns, have greater numbers of primitive functions for *sp* and polarization functions than the comparably sized Dunning basis sets. These basis set have been found to outperform correlation consistent basis sets for some vibrational frequencies.[80]

In all cases, an unrestricted Hartree-Fock (UHF) determinant was used as the reference wave function, which allowed for the use of analytic second derivatives in vibrational frequency computations.[117] The accuracy of this reference is influenced by the degree of spin-contamination and static correlation in the system. The commonly used $\mathscr{T}_1$ diagnostic[58, 75, 136] correlates the magnitude of orbital-relaxation effects in the CCSD wave function to multireference requirements, and sometimes advises a multireference approach for $\mathscr{T}_1 > 0.02$. While each of the conformers for the formylperoxy radical have $\mathscr{T}_1 = 0.05$ (see Table 2.1), for open-shell systems the $\mathscr{T}_1$ diagnostic has a less well-defined threshold. This is because large orbital-relaxation effects may be attributed to dynamic correlation rather than the static correlation.[20] Instead, the largest T_2 amplitude (max t_{ij}^{ab}) has been found to be a better description of the character of these systems.[20] The max t_{ij}^{ab} of $0.04 - 0.05$, and the $\langle \hat{S}^2 \rangle_{\text{UHF}}$ values of 0.76 for each system (which have minimal deviation from the expected value of 0.75 for a doublet state) indicate that the wave function is sufficiently described to zeroth order by a single UHF reference determinant.

Table 2.1: Diagnostics on the single reference UHF determinant for the isomers of formylperoxy radical. With $\mathscr{T}_1 = \sqrt{\frac{|t_1^{\alpha\alpha}|^2 + |t_1^{\beta\beta}|^2}{N_{\text{corr}}}}$ and max t_{ij}^{ab} is the maximum value in the T_2 amplitudes.

	$\tilde{\text{X}}$ A″			$\tilde{\text{A}}$ A′	
	trans	*cis*	TS	*trans*	*cis*
$\langle \hat{S}^2 \rangle_{UHF}$	0.76	0.76	0.76	0.76	0.76
$\mathscr{T}_1$	0.040	0.039	0.042	0.034	0.032
max t_{ij}^{ab}	0.05	0.05	0.04	0.05	0.05

The focal point analysis (FPA) scheme of Allen and co-workers was employed to determine relative energies to a high degree of reliability.[5, 23, 29, 42] After computation of the stationary point geometries at CCSD(T) using the cc-pVQZ[28] the electronic energy at these geometries was extrapolated to the CBS limit of the CCSDT(Q) (coupled cluster with single, double, triple, and perturbative quadruple excitations)[11, 60, 61] method using the cc-pVnZ ($n = 2,3,4,5,6$) basis sets. These basis sets were selected due to their facilitation toward convergence. The frozen-core approximation was utilized in all optimizations (i.e., excitations from 1s-like molecular orbitals of second row atoms were omitted in post-Hartree-Fock procedures). Core correlation corrections to the valence focal-point analysis were computed as:

$$\Delta E_{\text{core}} = E^{\text{cc-pCVQZ}}_{\text{CCSD(T)(AE)}} - E^{\text{cc-pCVQZ}}_{\text{CCSD(T)(FC)}} \tag{2.1}$$

where AE notates that correlation extends to all electrons and FC denotes use of the frozen core approximation. Including one- and two-electron Darwin terms and mass velocity contributions [21, 71] accounted for scalar relativistic effects at first order. These were obtained at the all-electron CCSD(T)/aug-cc-pCVTZ level, as advocated for first row atoms, and additional second order Douglas-Kroll corrections were considered negligible.[8, 25] As a test for non-adiabatic effects, we used the diagonal Born-Oppenheimer correction (DBOC) computed at HF/aug-cc-pVTZ. [46, 111]

Harmonic vibrational frequencies were determined analytically at the CCSD(T)/ANO2 level of theory. Second order vibrational perturbation theory (VPT2) computed anharmonic corrections ($\delta\nu$) with the CCSD(T)/ANO1 method. The VPT2 method employs the full cubic force field and the semi-diagonal part of the quartic force field. Numerical differentiation of the harmonic

frequencies with respect to normal coordinates ascertained these force fields. We also include a correction for orbital-relaxation effects ($\delta\omega$), computed as the difference between Brueckner-[17, 115] and CCSD(T)/ANO1 harmonic frequencies. Addition of these corrections to CCSD(T)/ANO2 harmonic vibrational frequencies (ω) resulted in final frequencies (ν), $\nu = \omega + \delta\omega + \delta\nu$. These geometries and frequencies were obtained via single-point energy computations interfaced with PSI4's optimization and finite-difference codes. [127]

2.4 Results and Discussion

2.4.1 Geometries

The formylperoxy radical has two conformers which are labeled *cis* and *trans* based on the direction of the O′O″ bond with respect to the carbonyl (see Figure 2.1). Each has an electron configuration in the ground state of $(1a')^2(2a')^2...(13a')^2(3a'')$. The term symbols for the ground ($\tilde{X}$) and first excited ($\tilde{A}$) states are $^2A''$ and $^2A'$, respectively. Depicted in Figure 2.2, the $13a'$ and $3a''$ orbitals correspond predominantly to the in-plane and out-of-plane π^* orbitals of O_2.

Figures 2.1a and 2.1b show the optimized geometries for the $\tilde{X}$ $^2A''$ *cis* and *trans* isomers computed at the CCSD(T)/ANO2 and CCSD(T)/cc-pVQZ levels of theory. The $\tilde{A}$ $^2A'$ *cis* and *trans* isomers optimized geometries, at the same level, are shown in Figures 2.1c and 2.1d. The optimized geometries for both basis sets agree to within 0.001 Å for all bond lengths and 0.1° for all angles. The excited states are structurally similar to the ground state geometries, but differ from them, in both conformers, with a 0.06 Å longer O′O″ bond and 0.03 Å shorter CO bond. In the *trans* isomer, the HCO′ and CO′O″ angles increase by about 3° each from the $^2A''$ to the $^2A'$ state at the expense of the OCO′ angle. Contrarily, the angles of the *cis* isomer, constrained by carbonyl

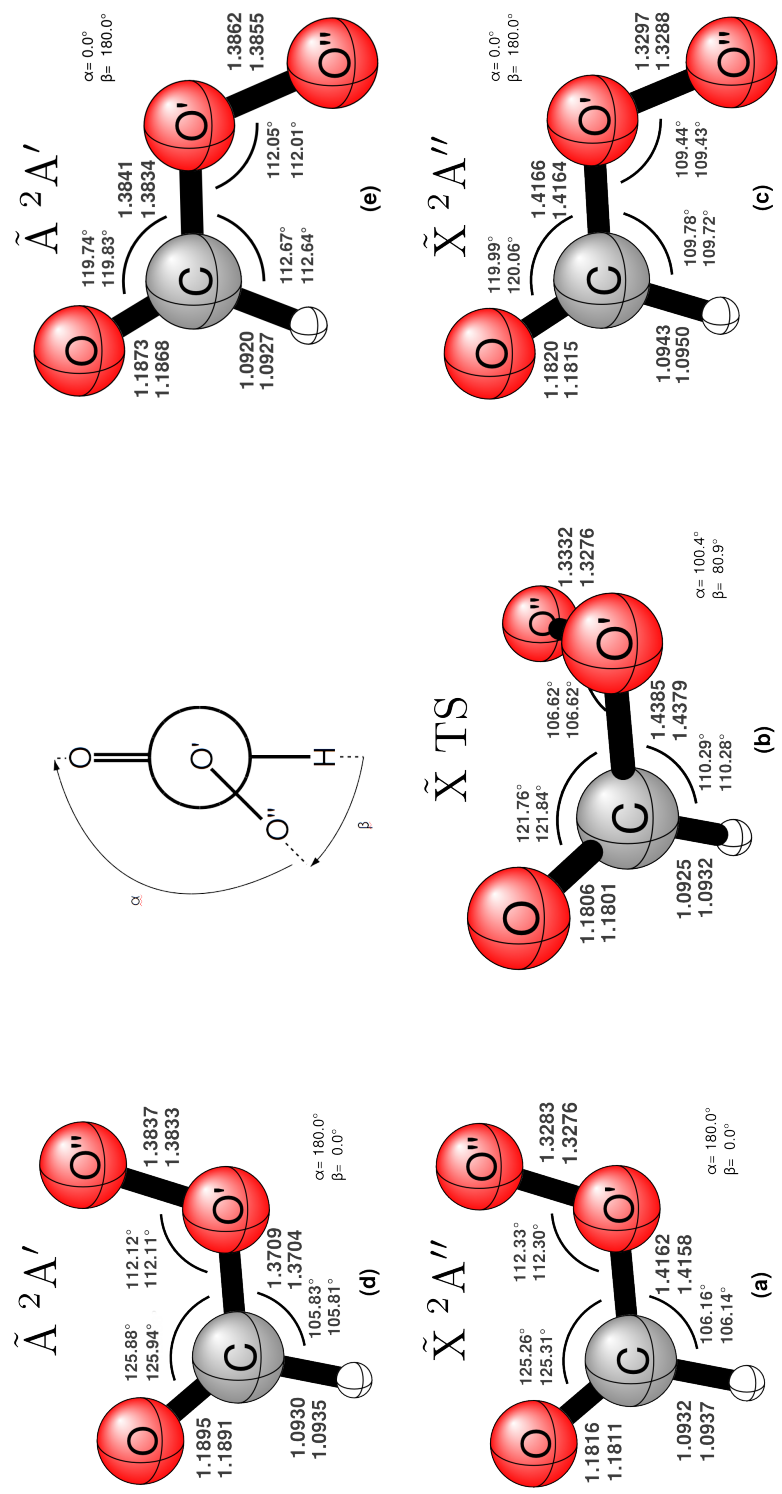

Figure 2.1: The CCSD(T)/ANO2 (top) and CCSD(T)/cc-pVQZ (bottom) optimized geometries for (a) the $\tilde{X}\,^2A''$ *cis* structure; (b) the $\tilde{X}$ torsional transition state (c) the $\tilde{A}\,^2A'$ *cis* structure; (d) the $\tilde{X}\,^2A''$ *trans* structure; and (e) the $\tilde{A}\,^2A'$ *trans* structure.

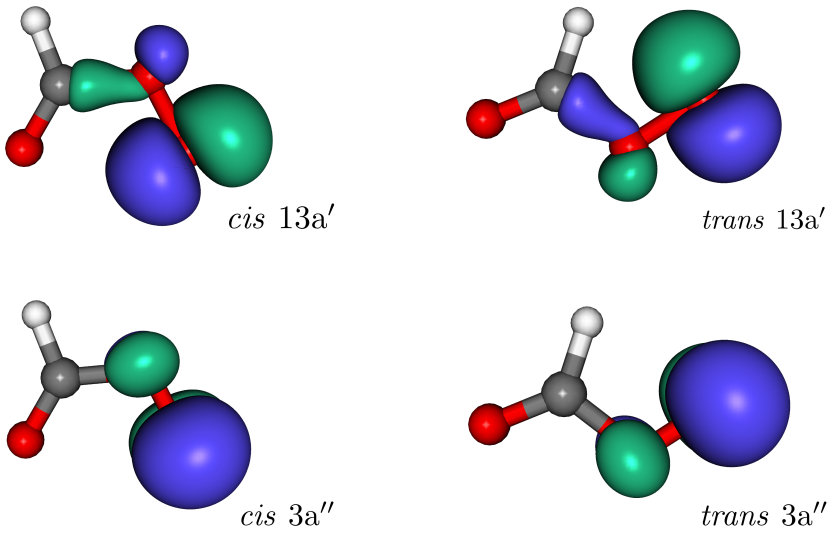

Figure 2.2: CASSCF/cc-pVDZ ground and first excited state averaged 13a' and 3a'' orbitals (the HOMO and SOMO, respectively) for HC(O)OO$^{\bullet}$.

oxygen-terminal oxygen interaction, are not significantly affected by excitation of an electron from the lone pair to the singly occupied out-of-plane π^* orbital ($n \rightarrow \pi^*$).

The significant elongation of the O−O bond distance between structures of the ground and first-excited states is characteristic of the $\tilde{X}$ and $\tilde{A}$ states of RO_2 species and has been theoretically recognized in similar systems [$C_2H_5O_2^\bullet$, $CH_3O_2^\bullet$,$CH_3C(O)O_2^\bullet$, and $HO_2^\bullet$][19, 20, 52, 76]. Our O−O equilibrium distances are roughly 1.33 Å for the ground state stationary points (Figs. 2.1a, 2.1b, and 2.1c), considerably shorter than the ≈1.39 O−O Å bond found for the excited state structures (Figs. 2.1d and 2.1e). The O−O bond lengths match the related theoretical $\tilde{A}$ and $\tilde{X}$ $CH_3C(O)O_2^\bullet$ lengths (to within 0.002 Å and 0.008 Å, respectively).[20] Comparison to the peroxyl bond of HO_2 (Ref. [126]) reveals a difference of only 0.001 Å and 0.01 Å. This experimental molecular geometry was determined from the rotational constants measured in the reaction of O/O_2 and CD_3OD or CH_3OH in a discharge flow system. Tuckett, Freedman, and Jones used interferometric spectrometry to determine the constants by an independent state fit of the combination differences in the spectra of HO_2 and DO_2.

2.4.2 Relative Energies

To further characterize the $\tilde{X}$ and $\tilde{A}$ potential energy surfaces of formylperoxy radical, we have computed thermodynamic relationships between all of the conformers in Figure 2.1. In particular, we have determined relative electronic energies assuming the CCSD(T)/cc-pVQZ geometries and using coupled-cluster theory with up to perturbative quadruple excitations [CCSDT(Q)], extrapolated to the CBS limit. The relative energy between the *cis* and *trans* ground state conformers is shown in Table 2.2. Excellent convergence emerges in the focal-point treatment, using up to the cc-pV6Z basis set. Here, basis set uncertainty is 0.01 kcal mol^{-1} on the ground state surface and

0.02 kcal mol^{-1} on the excited state surface at CCSDT(Q). Similarly, the correlation treatment converges towards the full CI limit very nicely. Contributions of perturbative quadruples at the CBS limit are 0.01 (for the *trans*-$\tilde{\mathrm{X}}\,^2\mathrm{A}'' \rightarrow$ *cis*-$\tilde{\mathrm{X}}\,^2\mathrm{A}''$ transition), 0.03 (for the *trans*-$\tilde{\mathrm{X}}\,^2\mathrm{A}'' \rightarrow \tilde{\mathrm{X}}$ TS), 0.04 (for the *trans*-$\tilde{\mathrm{X}}\,^2\mathrm{A}'' \rightarrow$ *trans*-$\tilde{\mathrm{A}}\,^2\mathrm{A}'$), 0.08 (for the *cis*-$\tilde{\mathrm{X}}\,^2\mathrm{A}'' \rightarrow$ *cis*-$\tilde{\mathrm{A}}\,^2\mathrm{A}'$), and 0.05 kcal mol^{-1} (for the *trans*-$\tilde{\mathrm{A}}\,^2\mathrm{A}' \rightarrow$ *cis*-$\tilde{\mathrm{A}}\,^2\mathrm{A}'$). Bearing in mind both the basis set and correlation uncertainties, the estimated uncertainty to the final energy (Δ_e) for all structures is within thermochemical accuracy (0.1 kcal mol^{-1}).[110] Focal point treatment of the ground state relative energy between the CCSD(T)/ANO2 conformers resulted in the same basis set and correlation uncertainties as well as the same final electronic energy as for the CCSD(T)/cc-pVQZ.

Core (Δ_{core}), relativistic (Δ_{rel}), and non-adiabatic (Δ_{DBOC}) corrections are shown in Table 2.3. These considerations affect the final energies by 0.00–0.04 kcal mol^{-1}, indicating that the corresponding approximations are appropriate for this system. The harmonic zero-point vibrational energy corrections (Δ_{ZPVE}) were found at CCSD(T)/cc-pVQZ. These corrections, with anharmonic contributions obtained via VPT2 at CCSD(T)/ANO1, are reported in Table 2.3, ranging from 0.04–0.26 kcal mol^{-1}.

The final, corrected relative energies ($\Delta H_{0\mathrm{K}}$) are given in Table 2.3 and shown schematically in Figure 2.3. It is interesting to note that whereas the *trans* isomer is predicted to lie 2.41 kcal mol^{-1} lower in energy than the *cis* isomer, the energetic ordering is reversed in the excited state, where the *cis*-$\tilde{\mathrm{A}}\,^2\mathrm{A}'$ conformer is 2.73 kcal mol^{-1} lower in energy than the *trans*-$\tilde{\mathrm{A}}\,^2\mathrm{A}'$. One possible explanation for this difference is that the long-range interaction between the terminal oxygens of the O=COO$^\bullet$ back-bone are repulsive when the 13a$'$ in-plane orbital (see Figure 2.2) is doubly occupied. This effect favors the *trans* conformer of the ground electronic state. The interaction

is less repulsive when the 13a$'$ orbital is only singly occupied, favoring the *cis* conformer, in the excited state.

Table 2.2: Relative electronic energies (kcal mol^{-1}) for formylperoxy radical conformers extrapolated to the complete basis set limit [CCSDT(Q)/CBS].

			Coupled-Cluster				
n	UHF	δMP2	δSD	δSD(T)	δSDT	δSDT(Q)	SDT(Q)
1. Ground state							
			trans ($\tilde{\text{X}}$ A$''$) $\rightarrow$ *cis* ($\tilde{\text{X}}$ A$''$)				
D	+0.35	+1.47	–0.13	+0.08	+0.07	+0.01	+1.85
T	+0.93	+1.42	–0.19	+0.12	+0.04	+0.01	+2.33
Q	+1.04	+1.39	–0.20	+0.12	[+0.04]	[+0.01]	[+2.40]
5	+1.04	+1.35	–0.20	+0.11	[+0.04]	[+0.01]	[+2.36]
6	+1.05	+1.34	[–0.20]	[+0.11]	[+0.04]	[+0.01]	[+2.36]
∞	[+1.05]	[+1.33]	[–0.20]	[+0.11]	[+0.04]	[+0.01]	**[+2.35]**
2. Isomerization barrier							
			trans ($\tilde{\text{X}}$ A$''$) $\rightarrow$ $\tilde{\text{X}}$ TS				
D	+9.23	+0.66	–1.09	+0.14	+0.01	–0.01	+8.93
T	+8.78	+1.05	–0.99	+0.07	[–0.33]	[–0.02]	[+8.56]
Q	+8.70	+1.15	–0.96	+0.04	[–0.33]	[–0.02]	[+8.59]
5	+8.69	+1.13	–0.95	+0.03	[–0.33]	[–0.02]	[+8.55]
6	+8.69	+1.13	[–0.95]	[+0.03]	[–0.33]	[–0.02]	[+8.55]
∞	[+8.69]	[+1.14]	[–0.95]	[+0.03]	[–0.33]	[–0.02]	**[+8.56]**
3. Adiabatic excitation energies							
			trans ($\tilde{\text{X}}$ A$''$) $\rightarrow$ *trans* ($\tilde{\text{A}}$ A$'$)				
D	+13.23	+4.82	–0.27	+0.26	–0.10	+0.03	+17.98
T	+13.14	+4.93	–0.34	+0.46	–0.16	+0.04	+18.06
Q	+13.21	+5.05	–0.34	+0.49	[–0.16]	[+0.04]	[+18.30]
5	+13.21	+5.09	–0.34	+0.51	[–0.16]	[+0.04]	[+18.34]
6	+13.21	+5.11	[–0.34]	[+0.51]	[–0.16]	[+0.04]	[+18.36]
∞	[+13.21]	[+5.13]	[–0.34]	[+0.51]	[–0.16]	[+0.04]	**[+18.38]**
			cis ($\tilde{\text{X}}$ A$''$) $\rightarrow$ *cis* ($\tilde{\text{A}}$ A$'$)				
D	+8.48	+3.88	+0.25	+0.32	–0.04	+0.06	+12.96
T	+8.29	+3.83	+0.23	+0.50	–0.06	+0.08	+12.86
Q	+8.33	+3.91	+0.24	+0.53	[–0.06]	[+0.08]	[+13.02]
5	+8.32	+3.93	+0.24	+0.55	[–0.06]	[+0.08]	[+13.06]
6	+8.32	+3.95	[+0.24]	[+0.55]	[–0.06]	[+0.08]	[+13.07]

∞	[+8.31]	[+3.97]	[+0.25]	[+0.56]	[–0.06]	[+0.08]	**[+13.09]**
4. Excited state relative energies							
			cis ($\tilde{A}$ A') → *trans* ($\tilde{A}$ A')				
D	+4.40	–0.53	–0.39	–0.14	–0.14	–0.04	+3.16
T	+3.93	–0.33	–0.39	–0.16	–0.13	–0.05	+2.88
Q	+3.85	–0.25	–0.39	–0.16	[–0.13]	[–0.05]	[+2.88]
5	+3.85	–0.19	–0.39	–0.15	[–0.13]	[–0.05]	[+2.92]
6	+3.84	–0.18	[–0.39]	[–0.15]	[–0.13]	[–0.05]	[+2.93]
∞	[+3.84]	[–0.17]	[–0.39]	[–0.15]	[–0.13]	[–0.05]	**[+2.95]**

Brackets indicate values obtained by extrapolations or additivity assumptions rather than direct computations. Final CCSDT(Q)/CBS values are shown in bold. The column labeled *n* refers to the cardinality of the basis set, cc-pV*n*Z, where *n* = ∞ is the CBS limit.

Table 2.3: Enthalpies (H_{0K}) at 0 K from the addition of auxiliary core [CCSD(T)/cc-pCVQZ] (Δ_{core}), one and two-electron Darwin and mass velocity relativistic [CCSD(T)/aug-cc-pCVTZ] (Δ_{rel}), diagonal Born-Oppenheimer [HF/aug-cc-pVTZ] (Δ_{DBOC}), and anharmonic zero-point vibrational energy [CCSD(T)/cc-pVQZ] (Δ_{ZPVE}) corrections to the energy extrapolated to the CBS limit (E_{CBS}). All values are in kcal mol^{-1}.

	E_{CBS}	Δ_{core}	Δ_{rel}	Δ_{DBOC}	Δ_{ZPVE}	H_{0K}
cis ($\tilde{X}$ A″) → *trans* ($\tilde{X}$ A″)	2.35	−0.01	0.00	0.01	0.06	2.41
trans ($\tilde{X}$ A″) → $\tilde{X}$ TS	8.56	0.01	0.00	0.01	−0.49[a]	8.09
trans ($\tilde{X}$ A″) → *trans* ($\tilde{A}$ A′)	18.38	0.02	0.00	0.00	−0.24	18.17
cis ($\tilde{X}$ A″) → *cis* ($\tilde{A}$ A′)	13.09	0.02	−0.05	0.00	−0.04	13.03
trans ($\tilde{A}$ A′) → *cis* ($\tilde{A}$ A′)	2.95	−0.01	0.05	−0.01	−0.26	2.73

[a] The reported value does not include anharmonic contributions, as the transition state was not amenable to VPT2 treatment.

The energy of the *trans*-$\tilde{X}^2A''$ → *trans*-$\tilde{A}^2A'$ excitation was reported through photoelectron spectroscopy of the peroxyformate ion by Lineberger and coworkers[132] as 18.1 ± 1.4 kcal mol^{-1}. They identified this value via a 3.27 eV eBE peak in the photoelectron spectrum that could be assigned only to *trans*-$\tilde{A}^2A'$ HC(O)OO. The uncertainty is due to their inability to distinguish if the peak (which is 18.0 kcal mol^{-1} higher than the 2.48 eV ground state band origin) was from the *trans*-$\tilde{A}^2A'$ CO′O″ bend or electronic band origin. We predict the *trans*-$\Delta H_{0K,\tilde{A}\leftarrow\tilde{X}}$ to be 18.17 ± 0.1 kcal mol^{-1}, well within the error bars of the experimental value. No evidence for the *cis* isomer of the formylperoxy radical has been presented experimentally, though the reaction barrier $\Delta H_{0K,cis-\tilde{X}\leftarrow trans-\tilde{X}}$ is determined in this work to be only 8.09 kcal mol^{-1}.

Vertical transition properties for *cis* and *trans* $\tilde{A} \leftarrow \tilde{X}$ were computed with the EOM-CCSD/ANO2 method (Table 2.4). The $\tilde{X}^2A''$ state equilibrium geometries were used for the purpose of finding absorption properties. The reciprocal of Einstein's transition probability coefficient ($\mathscr{A}$) is the maximum possible mean lifetime for a given state, when the only mechanism of deactivation is spontaneous emission to the lower state.[116] In this manner, the *trans* excited state lifetime is

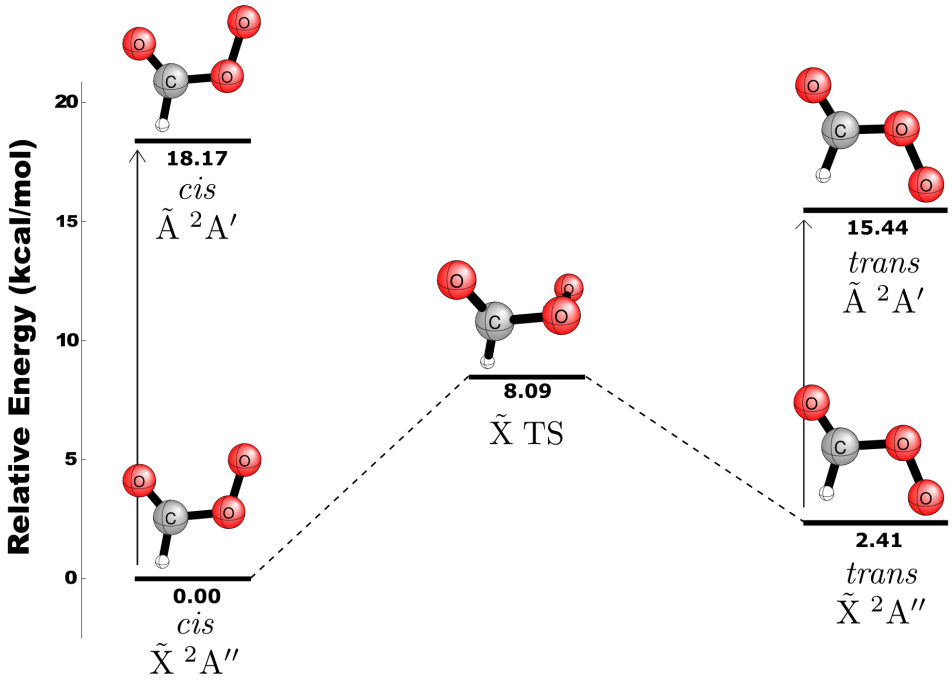

Figure 2.3: Potential energy diagram for formylperoxy radical including core, relativistic, DBOC, and ZPVE corrections (in kcal mol^{-1}). The electronic energies are extrapolated to the CBS limit.

Table 2.4: Transition properties for $\tilde{A}\,^2A' \leftarrow \tilde{X}\,^2A''$ predicted at the EOM-CCSD/ANO2 level of theory. The quantity $\tilde{\nu}_A$ is the vertical excitation energy in kcal mol^{-1}, $|\langle\tilde{X}|\hat{\mu}|\tilde{A}\rangle|$ is the transition dipole moment in Debye, f_A is the oscillator strength, and the Einstein Coefficients $\mathscr{A}$ and $\mathscr{B}$ are given in units of Hz and m^3 J^{-1} s^{-2}, respectively.

	trans		*cis*	
	$\tilde{X}$ A$''$	$\tilde{A}$ A$'$	$\tilde{X}$ A$''$	$\tilde{A}$ A$'$
$\tilde{\nu}_A$	20.61	16.96	14.90	11.65
$\lvert\langle\tilde{X}\lvert\hat{\mu}\rvert\tilde{A}\rangle\rvert$	0.065	0.053	0.057	0.048
f_A	14.2×10^{-6}	7.8×10^{-6}	8.0×10^{-6}	4.4×10^{-6}
Coefficient	$\mathscr{B}=7.92\times10^{16}$	$\mathscr{A}=184$	$\mathscr{B}=6.11\times10^{16}$	$\mathscr{A}=48.8$

predicted to be $\tau_{\tilde{A}} \approx 5.4$ ms and the *cis* excited state has $\tau_{\tilde{A}} \approx 20.5$ ms. Neither the *cis* nor *trans* $\tilde{A}\,^2A'$ electronic state lifetime has yet been observed experimentally.

2.4.3 Fundamental Vibrational Analysis

Frequencies for the $\tilde{X}\,^2A''$ *trans* and *cis* isomers, with VPT2 treatment at the CCSD(T)/ANO2 level, are shown in Table 2.5. The most intense peak is the $\nu_2(a')$ C=O stretch (240 km mol^{-1} *trans*/ 197 km mol^{-1} *cis*) followed by the $\nu_5(a')$ C–O$'$ stretch (226 km mol^{-1} *trans*/ 182 km mol^{-1} *cis*). For the ground state conformers, the *cis* O$'$–O$''$ stretch is significantly greater in intensity than the *trans* (26 km mol^{-1} *trans*/ 75 km mol^{-1}). Table 2.5 provides frequencies for the excited $\tilde{A}\,^2A'$ state as well. The O$'$–O$''$ stretch IR intensity is notably weaker in the excited state than in the ground, and this fundamental experiences the greatest shift from its ground state frequency of all the modes – at a nearly 200 cm^{-1} lower frequency in the excited state than in the ground for both conformers.

Table 2.5: Vibrational frequencies (cm^{-1}) and IR intensities (km mol^{-1}) for the *cis* and *trans* isomers with harmonic frequencies (ω), anharmonic corrections ($\delta\nu$), and Brueckner corrections ($\delta\omega$).

		trans					*cis*				
Mode	**Description**	ω^a	$\delta\nu^b$	$\delta\omega^c$	ν^d	**Intensity**^{e}	ω^a	$\delta\nu^b$	$\delta\omega^c$	ν^d	**Intensity**^{e}
$\tilde{X}\,^2A''$											
$\nu_1(a')$	CH str	3099	−152	−1	2946	9	3107	−153	−1	2953	19
$\nu_2(a')$	CO str	1866	−31	0	1835	240	1860	−18	0	1842	197
$\nu_3(a')$	HCO bend	1333	−35	−1	1296	1	1373	−34	−1	1338	1
$\nu_4(a')$	O′O″ str	1144	−20	−5	1119	26	1109	−28	−2	1079	75
$\nu_5(a')$	CO′ str	1016	−15	−1	1000	226	906	−27	−2	877	182
$\nu_6(a')$	OCO′ bend	604	−13	−1	590	11	800	−18	−1	780	6
$\nu_7(a')$	CO′O″ bend	414	−3	−1	410	15	335	−7	0	328	3
$\nu_8(a'')$	wag	1014	−22	0	991	< 1	986	−28	−1	957	< 1
$\nu_9(a'')$	torsion	171	−4	0	167	18	238	−6	0	233	16
$\tilde{A}\,^2A'$											
$\nu_1(a')$	CH str	3108	−153	0	2955	11	3108	−158	−1	2949	16
$\nu_2(a')$	CO str	1833	−33	0	1800	334	1815	−35	1	1780	279
$\nu_3(a')$	HCO bend	1395	−33	−2	1360	1	1380	−41	−1	1337	1
$\nu_4(a')$	O′O″ str	957	−1	−7	949	21	895	−6	−5	884	29
$\nu_5(a')$	CO′ str	1054	−35	−4	1015	354	1063	−36	−6	1021	273
$\nu_6(a')$	OCO′ bend	599	−8	−2	589	7	773	−9	−2	762	10
$\nu_7(a')$	CO′O″ bend	333	−5	0	328	13	255	−3	−1	251	1
$\nu_8(a'')$	wag	1008	−19	−1	988	<1	1012	−23	−1	989	1
$\nu_9(a'')$	torsion	192	−3	0	189	13	375	−12	0	363	17

[a] Computed with CCSD(T)/ANO2.
[b] Computed with CCSD(T)/ANO1.
[c] BCCSD(T)/ANO1 − UHF-CCSD(T)/ANO1 harmonic vibrational frequencies.
[d] $\omega + \delta\nu + \delta\omega$.
[e] CCSD(T)/ANO2 harmonic IR intensities.

The computed $\tilde{X}\,^2A''$ fundamental frequencies are consistent with experiment, as portrayed in Table 2.6. Comparison of this work to the experiment supports previous claims[132, 147] that all experimentally determined bands are those of the *trans* isomers. Only the ν_2, ν_4, ν_5, and ν_6 modes have been identified experimentally. The ν_2 (1790.2 cm^{-1}) and ν_5 (1089.9 cm^{-1}) stretches were determined by Tso and Lee[124] via UV photooxidation of solid O_2 *trans*-$H_2C_2O_2$ at 13K. Tso and Lee concluded that these features may not represent isolated $HC(O)OO^{\bullet}$, because the latter may complex to both HO_2 and CO. Yang et al. provide more reliable results for ν_2 (1821.5 cm^{-1}) and ν_5 (957.3 cm^{-1}) through solid Ar matrix isolation infrared spectroscopy. They suggested that the discrepancy between the two experimental results is due to their successful isolation of $HC(O)OO^{\bullet}$ by condensation of CH_3OH/Ar and O_2/Ar via high-frequency discharge.[147] For the protonated species [HC(O)OOH], the Ar matrix shift for C=O is 7 cm^{-1}, O−O is 11 cm^{-1}, and C−O is 2 cm^{-1}.[54]. With a 13 cm^{-1} gap from the Ar measurement,[147] the anharmonic CCSD(T)/ANO2 *trans*-$\tilde{X}\,^2A''$ ν_2 (1835 cm^{-1}) lies just outside the Ar matrix shift for C=O (7 cm^{-1}), but within the standard deviation of Ar matrices (16 cm^{-1})[55]. The photoelectron spectrum of peroxyformate ion produced from the reaction of HOO^- with ethyl formate, identifies ν_4 (1098 $\pm$ 20 cm^{-1}), ν_5 (973 $\pm$ 20 cm^{-1}), and ν_6 (574 $\pm$ 35 cm^{-1}) for the formylperoxy radical.[132]

Table 2.6: Summary of previous and present research on the vibrational frequencies of the *trans* and *cis* conformations of the formylperoxy radical.

Method	$\nu_1(a')$	$\nu_2(a')$	$\nu_3(a')$	$\nu_4(a')$	$\nu_5(a')$	$\nu_6(a')$	$\nu_7(a')$	$\nu_8(a'')$	$\nu_9(a'')$
FTIR in O_2 matrix (*trans*)[a]		1788/1787			1091				
FTIR in Ar matrix (*trans*)[b]		1822			957				
Gas Phase Experiments (*trans*)[c]				1078 ± 20	966 ± 20	574 ± 35			
CCSD(T)/ANO2 (*trans*-$\tilde{X}\,^2A''$)[d]	2946	1835	1296	1119	1000	590	410	991	167
CCSD(T)/ANO2 (*cis*-$\tilde{X}\,^2A''$)[d]	2953	1842	1338	1079	877	780	328	957	233
CCSD(T)/ANO2 (*trans*-$\tilde{A}\,^2A'$)[d]	2955	1800	1360	949	1015	589	328	988	189
CCSD(T)/ANO2 (*cis*-$\tilde{A}\,^2A'$)[d]	2949	1780	1337	884	1021	762	251	989	363

[a] Tso and Lee (Ref. [124].)

[b] Yang et al. (Ref. [147]).

[c] Lineberger and coworkers (Ref. [132]).

[d] Anharmonic corrected frequencies found in this work.

In the computation of the *cis*-$\tilde{X}\,^2A''$ C=O stretch fundamental frequency, which is roughly twice the C$-$O$'$ stretch, a potential Fermi resonance had to be considered. A standard procedure, provided by Nielson[92], modifies the VPT2 treatment, in instances when $\nu_r \approx \nu_s + \nu_t$, by computing a replacement term for the anharmonic constant x_{rs}. Rather than eliminate the cubic force field terms from the first-order Hamiltonian by performing a contact transformation on the (ν_r, $\nu_s + \nu_t$) interaction, the correction becomes

$$\frac{\phi_{rst}^2 \nu_r(\nu_r^2 - \nu_s^2 - \nu_t^2)}{(\nu_r + \nu_s + \nu_t)(\nu_r + \nu_s - \nu_t)(\nu_r - \nu_s + \nu_t)(\nu_r - \nu_s - \nu_t)}$$

$$\rightarrow \frac{1}{4}\left[\frac{1}{(\nu_r + \nu_s + \nu_t)} + \frac{1}{(\nu_r - \nu_s + \nu_t)} + \frac{1}{(\nu_r + \nu_s - \nu_t)}\right]$$

Next, the first-order Hamiltonian's remaining resonance interaction is treated by explicitly diagonalizing the 2×2 matrix

$$\begin{bmatrix} \nu_r & \frac{\phi_{rst}}{\sqrt{8}} \\ \frac{\phi_{rst}}{\sqrt{8}} & \nu_s + \nu_t \end{bmatrix}$$

where the matrix element of the anharmonic potential across the zeroth-order, quasidegenerate states (ν_r and $\nu_s + \nu_t$) is most affected by the off-diagonal element of the cubic force constant ϕ_{rst}. A cutoff of ($\phi \geq 80$ cm^{-1} and $\delta \leq 50$ cm^{-1}) prevents exclusion of any interactions other than the (ν_2, $\nu_5 + \nu_5$), which occurred only in the *cis*-$\tilde{X}\,^2A''$ isomer. In this work, the Nielson correction for the Fermi resonance altered the VPT2 anharmonic correction by up to 27 cm^{-1} [for the *cis* HC(^{18}O)OO isotopologue].

2.4.4 Isotopologues

The equilibrium internuclear distances (r_e) and vibrationally averaged equilibrium parameters ($r_{g,0K}$), at 0 K, for both the states and conformers of the parent molecule and the five ground state isotopologues are reported in Table 2.7. Copan and coworkers [19] laid out a method to expand each distance in the leading terms of its normal coordinate Taylor expansion and average with respect to the ground vibrational state:[22, 70]

$$r_{g,0K} = \langle r \rangle_{g,0K} \approx r_e + \sum_s \left(\frac{\partial r}{\partial Q_s}\right)_e \langle Q_s \rangle_{0K} + \frac{1}{2} \sum_s \left(\frac{\partial^2 r}{\partial Q_s^2}\right)_e \langle Q_s^2 \rangle_{0K} \tag{2.2}$$

In Equation 2.2, $\langle Q_s \rangle$, the linear term, is averaged with respect to the VPT2 anharmonic vibrational wave function, and $\langle Q_s^2 \rangle$, the quadratic term, is averaged with respect to the harmonic vibrational wave function. The equilibrium geometries were obtained with the CCSD(T)/ANO2 method and vibrational corrections predicted at CCSD(T)/ANO1. These vibrationally-averaged internuclear separations experience increases as great as 0.02 Å from the equilibrium distance, in the case of the C−H bond length. The increase is not unexpected, as the modes of the C–H bond are associated with the highest degree of anharmonicity in the system (with $\delta\nu_1 = 150\ \mathrm{cm}^{-1}$).

Tables 2.8 and 2.9 show the VPT2-corrected CCSD(T)/ANO2 vibrational frequencies for various isotopologues of the $\tilde{\mathrm{X}}\,^2\mathrm{A}''$-*cis* and $\tilde{\mathrm{X}}\,^2\mathrm{A}''$-*trans* formylperoxy radical. Isotopic frequency shifts from the parent isomer are presented in Table 2.10.

Table 2.7: Equilibrium bond lengths (r_e) optimized at CCSD(T)/ANO2 and vibrationally averaged ($r_{g,0K}$) computed at CCSD(T)/ANO1 in Ångstrom for both the *trans*- and *cis*-$\tilde{X}\,^2A''$ formylperoxy radicals and five of their isotopologues along with the $\tilde{A}\,^2A'$ formylperoxy parent radicals.

$\tilde{X}\,^2A''$		$HC(O)O_2$	$DC(O)O_2$	$H^{13}C(O)O_2$	$HC(^{18}O)O_2$	$HC(O)^{18}O_2$	$DC(O)^{18}O_2$	$\tilde{A}\,^2A'$	
	r_e	$r_{g,0K}$						r_e	$r_{g,0K}$
					trans				*trans*
r(C-H)	1.0943	1.1157	1.1099	1.1157	1.1157	1.1157	1.1100	1.0920	1.1132
r(C=O)	1.1920	1.1967	1.1967	1.1966	1.1965	1.1967	1.1967	1.1873	1.1919
r(C-O′)	1.4166	1.4286	1.4281	1.4284	1.4286	1.4284	1.4278	1.3841	1.3942
r(O′-O″)	1.3297	1.3358	1.3359	1.3358	1.3358	1.3354	1.3356	1.3862	1.3932
					cis				*cis*
r(C-H)	1.0932	1.1146	1.1089	1.1146	1.1146	1.1146	1.1089	1.0930	1.1145
r(C=O)	1.1816	1.1863	1.1863	1.1862	1.1863	1.1861	1.1863	1.1895	1.1941
r(C-O′)	1.4162	1.4276	1.4271	1.4274	1.4273	1.4276	1.4269	1.3709	1.3810
r(O′-O″)	1.3283	1.3351	1.3351	1.3351	1.3347	1.3351	1.3347	1.3837	1.3918

Table 2.9: Vibrational frequencies (cm^{-1}) and IR intensities (km mol^{-1}) of various isotopologues of the $^2A''$ *trans* formylperoxy radical. Harmonic frequencies (ω), anharmonic corrections ($\delta\nu$), and fundamentals (ν) are reported.[a]

Mode	**Description**	ω	$\delta\nu$	ν	**Intensity**
$H^{13}C(O)OO$					
$\nu_1(a')$	CH str	3088	−155	2934	9
$\nu_2(a')$	CO str	1826	−29	1796	224
$\nu_3(a')$	HCO bend	1332	−34	1297	1
$\nu_4(a')$	O′O″ str	1143	−21	1122	28
$\nu_5(a')$	CO′ str	994	−20	974	214
$\nu_6(a')$	OCO′ bend	600	−12	588	11
$\nu_7(a')$	CO′O″ bend	412	−4	408	15
$\nu_8(a'')$	wag	1000	−36	964	0
$\nu_9(a'')$	torsion	170	−3	166	17
$HC(O)^{18}O^{18}O$					
$\nu_1(a')$	CH str	3099	−149	2950	9
$\nu_2(a')$	CO str	1866	−32	1834	242
$\nu_3(a')$	HCO bend	1331	−33	1298	1
$\nu_4(a')$	O′O″ str	1083	−16	1067	23
$\nu_5(a')$	CO′ str	992	−24	968	218
$\nu_6(a')$	OCO′ bend	589	−11	578	11
$\nu_7(a')$	CO′O″ bend	399	−1	398	14
$\nu_8(a'')$	wag	1012	−22	990	0
$\nu_9(a'')$	torsion	167	−4	163	19
$HC(^{18}O)OO$					
$\nu_1(a')$	CH str	3099	−158	2941	9
$\nu_2(a')$	CO str	1825	−29	1796	234
$\nu_3(a')$	HCO bend	1329	−32	1297	1
$\nu_4(a')$	O′O″ str	1144	−19	1125	26
$\nu_5(a')$	CO′ str	1015	−31	984	225
$\nu_6(a')$	OCO′ bend	590	−11	579	10
$\nu_7(a')$	CO′O″ bend	410	−2	408	15
$\nu_8(a'')$	wag	1012	−22	990	0
$\nu_9(a'')$	torsion	169	−4	165	18
DC(O)OO					

$\nu_1(a')$	CH str	2323	−75	2247	24
$\nu_2(a')$	CO str	1815	−27	1788	235
$\nu_3(a')$	HCO bend	1011	−15	996	165
$\nu_4(a')$	O′O″ str	1143	−20	1123	27
$\nu_5(a')$	CO′ str	980	−19	961	48
$\nu_6(a')$	OCO′ bend	600	−11	589	10
$\nu_7(a')$	CO′O″ bend	402	−4	398	14
$\nu_8(a'')$	wag	848	−14	833	2
$\nu_9(a'')$	torsion	162	−4	158	13
DC(O)^{18}O^{18}O					
$\nu_1(a')$	CH str	2322	−75	2247	24
$\nu_2(a')$	CO str	1815	−28	1787	237
$\nu_3(a')$	HCO bend	1004	−10	994	103
$\nu_4(a')$	O′O″ str	1081	−17	1064	22
$\nu_5(a')$	CO′ str	960	−22	938	104
$\nu_6(a')$	OCO′ bend	585	−11	574	10
$\nu_7(a')$	CO′O″ bend	388	−4	384	13
$\nu_8(a'')$	wag	846	−14	832	2
$\nu_9(a'')$	torsion	158	−3	154	13

[a] See Table 2.5 and Theoretical Methods for additional information.

H^{13}C(O)OO

As the mass of carbon increases by 8% from ^{12}C to ^{13}C, the modes involving ^{13}C experience 2-3% frequency attenuation from the parent frequencies. Specifically, the C=O stretch shifts by -39 cm^{-1}, the C–O′ stretch by -26 cm^{-1}, and the C–H stretch by -13 cm^{-1} in the *trans* isotopomer. For the *cis* isotopomer, the shifts from the parent are -40 cm^{-1}, -24 cm^{-1}, and -12 cm^{-1}, respectively. The wag motion decreases by twice as much from ^{13}C substitution in the *trans* isomer,

Table 2.8: Vibrational frequencies (cm^{-1}) and IR intensities (km mol^{-1}) of various isotopologues of the $^2A''$ *cis* formylperoxy radical. Harmonic frequencies (ω), anharmonic corrections ($\delta\nu$), and fundamentals (ν) are reported.[a]

Mode	Description	ω	$\delta\nu$	ν	Intensity
$H^{13}C(O)OO$					
$\nu_1(a')$	CH str	3096	−154	2942	17
$\nu_2(a')$	CO str	1819	−17	1802	185
$\nu_3(a')$	HCO bend	1371	−34	1337	0
$\nu_4(a')$	O′O″ str	1108	−28	1080	68
$\nu_5(a')$	CO′ str	883	−27	855	180
$\nu_6(a')$	OCO′ bend	796	−18	779	5
$\nu_7(a')$	CO′O″ bend	335	−7	328	3
$\nu_8(a'')$	wag	972	−28	945	0
$\nu_9(a'')$	torsion	236	−6	230	15
$HC(O)^{18}O^{18}O$					
$\nu_1(a')$	CH str	3107	−154	2953	19
$\nu_2(a')$	CO str	1860	−23	1837	198
$\nu_3(a')$	HCO bend	1370	−33	1338	1
$\nu_4(a')$	O′O″ str	1049	−26	1023	78
$\nu_5(a')$	CO′ str	894	−25	869	166
$\nu_6(a')$	OCO′ bend	768	−18	750	8
$\nu_7(a')$	CO′O″ bend	324	−7	318	2
$\nu_8(a'')$	wag	985	−40	945	0
$\nu_9(a'')$	torsion	232	−5	227	16
$HC(^{18}O)OO$					
$\nu_1(a')$	CH str	3107	−161	2946	19
$\nu_2(a')$	CO str	1818	−58	1761	193
$\nu_3(a')$	HCO bend	1369	−33	1335	0
$\nu_4(a')$	O′O″ str	1109	−29	1080	74
$\nu_5(a')$	CO′ str	905	−27	878	182
$\nu_6(a')$	OCO′ bend	790	−18	772	5
$\nu_7(a')$	CO′O″ bend	327	−7	320	2
$\nu_8(a'')$	wag	984	−29	955	0
$\nu_9(a')$	torsion	209	−4	205	10

[a] See Table 2.5 and Theoretical Methods for abbreviations and details.

Table 2.10: Isotopic shifts (cm^{-1}) for the $^2A''$ *trans* and *cis* formylperoxy radicals. Predicted results are from CCSD(T)/ANO1 VPT2-corrected CCSD(T)ANO2 frequencies.

	HC(O)OO	H^{13}C(O)OO	HC(^{18}O)OO	HC(O)^{18}O^{18}O	DC(O)OO	DC(O)^{18}O^{18}O
trans						
$\nu_1(a')$	0	−13	−6	+3	−700	−700
$\nu_2(a')$	0	−39	−39	−1	−47	−48
$\nu_3(a')$	0	0	0	0	−301	−304
$\nu_4(a')$	0	−2	+1	−58	−1	−60
$\nu_5(a')$	0	−26	−17	−32	−40	−62
$\nu_6(a')$	0	−3	−12	−13	−2	−17
$\nu_7(a')$	0	−2	−2	−13	−13	−27
$\nu_8(a'')$	0	−27	−2	−1	−158	−159
$\nu_9(a'')$	0	−2	−1	−5	−22	−27

the frequency of which is -27 cm^{-1} from its parent, than in the *cis*, which is -13 cm^{-1} from its parent.

HC(^{18}O)OO

The modes of the *cis* and *trans* conformers react differently to substituting the carbonyl oxygen to ^{18}O. For example, substitution of the carbonyl oxygen in the *cis* isotopomer causes an 81 cm^{-1} decrease to the C=O frequency in comparison to the 39 cm^{-1} frequency shift from the parent isotopomer for the *trans* conformer. This substitution, however, causes a much lower shift to the *cis* is the case for the *trans* conformer for the C$-$O$'$ stretch. The mode of the former experiences a 1 cm^{-1} decrease, and the latter a 17 cm^{-1}. From these two stretches, the *cis* isomer appears to localize the effects of the mass change to directly interacting modes of the substituted atom, whereas the *trans* isomer experiences smaller change in those modes. The mass change effects, rather, are spread out across the system. Such dispersion across the *trans* system supports the conclusion that the lower energy of the *trans* conformer may be attributed to greater hyperconjugation effects in its system than in the *cis*.

HC(O)^{18}O^{18}O

Substitution of both peroxy oxygens with ^{18}O diminishes the frequencies of modes involved with that group by 1-5%. Most significantly, the O′–O″ stretch of both conformers decreases by 58 cm^{-1}. The ^{17}O→^{18}O C–O′ stretch decreases by 32 cm^{-1} in the *trans* conformer and, contrastingly, by 10 cm^{-1} in the *cis*. The *cis* structure, however, experiences a greater shift to the O=C–O′ bend due to the peroxy substitution than does the *trans*, with -31 cm^{-1} and -13 cm^{-1} shifts, respectively. This mode, in the *cis* conformer, may expose atoms O and O′ to more repulsive effects that are not present in the *trans* structure, making the *trans* structure the more malleable of the conformers for the O=C–O′ bend frequency.

DC(O)OO

The H→D substitution is the most impactful of those considered due to the significant relative mass change. For the *trans* species, substitution to DC(O)OO greatly diminishes the C–H stretch and HCO bend modes (by 700 cm^{-1} and 301 cm^{-1}, respectively). The *cis* conformer experiences even greater frequency shifts as a result of the deuterium substitution, with isotopic shifts of 709 cm^{-1} (ν_1, C–D stretch) and 343 cm^{-1} (ν_3, DCO bend). Shifts for both species arise in the out-of-plane wag motion as well. The ν_8 wag mode has a 158 cm^{-1} decrease for the *trans* and 147 cm^{-1} for the *cis*. A previous theoretical study on the methylperoxy radical noted the same decrease of $>$20% in the magnitude of fundamental frequencies when deuterium replaced the hydrogens of the parent isotopologue.[2]. For DC(O)OO, even the C=O stretch is 40 cm^{-1} lower for the deuterated structure than in the parent species. Here we see the significance of the hydrogen mass increase – it causes a greater impact on the C=O stretch than does changing the mass of either the participating oxygen or carbon atoms. The IR intensities experience a large impact from deuterium substitution as well.

While the HCO bend IR intensities are $\leq$1 km mol^{-1}, the DCO intensities drastically rise to be the second or third most prominent, at up to 165 km mol^{-1}.

DC(O)^{18}O^{18}O

H$\rightarrow$D in conjunction with O$'$O$''\rightarrow^{18}$O$'^{18}$O$''$ substitutions evoke similar changes to the frequencies as the deuterium substitution does by itself. For the *trans* species, the DC(O)^{18}O^{18}O frequencies shift from HC(O)OO by 700 cm^{-1} (ν_1, C–D stretch), 304 cm^{-1} (ν_3, DCO bend), and 159 cm^{-1} (ν_8, wag). The frequencies of *cis* conformer decrease after substitution with these three isotopes by 701 cm^{-1} (ν_1, C–D stretch), 347 cm^{-1} (ν_3, DCO bend), and 149 cm^{-1} (ν_8, wag). These are all within 3 cm^{-1} of the shifts due solely to deuterium substitution (DC(O)OO). The DC(O)^{18}O^{18}O shifts vary from DC(O)OO, as expected, most significantly for the O$'$–O$''$ stretch ($-$60 cm^{-1} in *trans* and $-$26 cm^{-1} in *cis*), which is more closely aligned to the HC(O)^{18}O^{18}O shifts. Many of these isotopic substitutions have been achieved in experiment to aid both mode and isomer identification in the spectroscopic studies.[124, 147] While Tso and Lee did not find an O$'$–O$''$ stretch for the parent isotopomer, they assigned the O$'$–O$''$ fundamental for DC(O)OO$^\bullet$ (ν_4, 1143.4 cm^{-1}) and DC(O)^{18}O^{18}O$^\bullet$ (ν_4, 1125.6 cm^{-1}).[124] We report the stretches for DC(O)OO$^\bullet$ (ν_4, 1123 cm^{-1}) and DC(O)^{18}O^{18}O$^\bullet$ (ν_4, 1064 cm^{-1}). Though the agreement is poor, it should be noted that the experimental fundamentals of Tso and Lee[123] differed from gas phase measurements of Lineberger and coworkers[132] by 100 cm^{-1} on their only mutually assigned frequency, the ν_5 mode.

Table 2.11 compares the isotopic vibrational frequency shifts to experimental findings[125, 147], for the two highest IR intensity modes (ν_2, C=O stretch and ν_5, C–O$'$ stretch). For each isotopic substitution of the *trans* isomer, which is the only experimentally reported conformer, the

computed shift from the parent vibrational frequency for the C=O stretch is within 4 cm^{-1} from the isotopic shift collected in the Ar matrix. For the C–O′ stretch, the computed shift from the frequencies of the parent isotopologue for each isotopic substitution is found to be 7-13 cm^{-1} larger than those measured in the Ar matrix. Though this deviation from experiment is large in contrast to the precision of the C=O stretch, it falls within the bounds of Ar matrix standard deviation (which affords uncertainty of 9 cm^{-1} for the parent C–O′ stretch and $\approx$8 cm^{-1} for that of the isotologues)[55].

Table 2.11: Summary of previous and current research on isotopic frequency shift (cm^{-1}) with respect to HC(O)OO.

	$H^{13}C(O)OO$	$HC(^{18}O)OO$	$HC(O)^{18}O^{18}O$	DC(O)OO	$DC(O)^{18}O^{18}O$
C=O stretch					
Matrix-isolated in O_2-*trans*[a]	−40	−69	−1	−31	−32
FTIR in solid Ar-*trans*[b]	−38	−39	−5	−46	
CCSD(T)/ANO2-*trans*[c]	−39	−39	−1	−47	−48
CCSD(T)/ANO2-*cis*[c]	−40	−81	−5	−61	−61
C–O stretch					
Matrix-isolated in O_2-*trans*[a]	−22	−1	−22		
FTIR in solid Ar-*trans*[b]	−19	−4	−24		
CCSD(T)/ANO2-*trans*[c]	−26	−17	−32	−40	−62
CCSD(T)/ANO2-*cis*[c]	−24	−1	−10	−49	−59

[a] Tso et al. (Ref. [125]).

[b] Yang et al. (Ref. [147]).

[c] Anharmonic corrected shift found in this work.

2.5 Conclusions

Important experimental studies of the formylperoxy radical still leave many many important questions unanswered.[91, 123–125, 132, 146, 147] The only experimental fundamentals are those for the *trans*-$\tilde{X}\,^2A''$ electronic state. There are no experimental fundamentals for the *trans*-$\tilde{A}\,^2A'$. *cis*-$\tilde{X}\,^2A''$, or *cis*-$\tilde{A}\,^2A'$ structures. In fact, there is no experimental information concerning the *cis* $\tilde{X}$ and $\tilde{A}$ states. The only experimental result for the *trans*-$\tilde{A}\,^2A'$ state is the $\tilde{X} \rightarrow \tilde{A}$ excitation energy determined from a single peak in the photoelectron spectrum, of Lineberger and coworkers.[132].

In this research, stationary points on the ground ($\tilde{X}$) and first excited ($\tilde{A}$) electronic state surfaces of the formylperoxy radical have been examined using coupled-cluster methods. On the $\tilde{X}$ surface, we find two minimum energy conformers connected by internal rotation of the terminal peroxy, designated *cis* and *trans*. These conformers are predicted to be separated by 2.41 kcal mol^{-1} with *trans* being lower in energy, and the isomerization barrier lies 8.09 kcal mol^{-1} above the *trans* in energy. Adiabatic electronic transitions to the excited state ($\tilde{A} \leftarrow \tilde{X}$) for the *cis* and *trans* conformers are predicted to be 13.03 kcal mol^{-1} and 18.17 kcal mol^{-1}, respectively. Our theoretical excitation energy is in excellent agreement with the experimental value of 18.1 $\pm$ 1.4 kcal mol^{-1} of Lineberger and coworkers.[132] Upon electronic excitation, the $O'O''$ bond length increases as expected for peroxy species. The energetic ordering of the *cis* and *trans* conformers is reversed in the $\tilde{A}\,^2A'$ excited state, possibly due to the long-range intramolecular interaction between terminal oxygen atoms. We predict lifetimes of $\tau_{\tilde{A}} \approx 5.4$ ms and $\tau_{\tilde{A}} \approx 20.5$ ms for the *trans* and *cis* electronic excited states, respectively. To aid in spectral characterization, we also predict the anharmonic vibrational frequencies of the two ground state minima and find agreement within the expected bounds of Ar matrix experiments and outside of gas-phase ν_4 and ν_5 modes by 20 cm^{-1}. We provide rigorous predictions for the four modes lacking experimental assignment. Frequency analyses

for $H^{13}C(O)OO^{\bullet}$, $HC(^{18}O)OO^{\bullet}$, $HC(O)^{18}O^{18}O^{\bullet}$, $DC(O)OO^{\bullet}$, and $DC(O)^{18}O^{18}O^{\bullet}$ isotopologues show excellent agreement with experimental values for the ν_2 (C=O stretch) and ν_5 (C–O′ stretch) modes.

2.6 Acknowledgement

This research was supported by the Department of Energy, Basic Energy Sciences, Division of Chemical Sciences, Fundamental Interactions Team, Grant No. DEFG02-97-ER14748. We thank Dr. Jay Agarwal and Andreas V. Copan for helpful discussions.

CHAPTER 3

PRESSURE INDEPENDENT RATE CONSTANTS FOR THE ADDITION OF ATMOSPHERIC MOLECULES TO CRIEGEE INTERMEDIATES

Criegee intermediates (CI) have gained much attention in hydrocarbon combustion and atmospheric chemistry due to their role in a prominent degradation pathway of alkenes through ozonolysis. Collisions with other gas-phase species stabilize a significant fraction of these CIs, depending on their substituents[27]. Bimolecular reactions of the resulting, stabilized CIs (sCI) have attracted significant interest, as reviewed[83, 98, 118, 119, 131]. They have a significant role in sulfuric acid formation[51, 72, 79, 101], aerosol formation[109, 150], NO_2 depletion and reformation[13, 130], hydroxyl radical formation[30, 89], and formic acid formation[34, 87, 90]. We provide reliable rate constants at the high pressure limit for several addition reactions of sCI, which will enable more accurate quantification of the environmental effects of CIs.

3.1 Comment on the Electronic Structure Methods used to Study Criegee Intermediiates

sCIs are particularly sensitive to the treatment of electron correlation. This observation is usually attributed to the mildly multireference character of the Criegee intermediates, as they can be viewed as either a Zwitterions or biradical molecules. By employing the Focal Point Approach[56] to extrapolate to the FCI limit, as described in CHAPTER 2, and then applying the $\Delta T(Q)=\Delta E_{CCSDT(Q)}$-$\Delta E_{CCSDT}$ correction, suggested by Fang *et al.*[30], we have successfully modeled addition reactions of Criegee intermediates with atmospheric molecules and biofuels[7, 85]. In these examples, the inclusion of the perturbative quadruples correction can qualitatively change the PES. Take for example our study of the reaction of methanol with two sCIs: formaldehyde oxide and acetone oxide[7]. The PES for the reaction is shown in (Figure 3.1). Here, we display the sensitivity of the PES for reactions of sCIs to the computational method. An error of $\frac{1}{2}$ kcal mol^{-1} results in the prediction of a submerged barrier. Uncertainty in the relative energy between the transition state and reactants, moreover, can invalidate assumptions we take in the kinetic model. The $\Delta T(Q)$ approach provides the accuracy required by these systems.

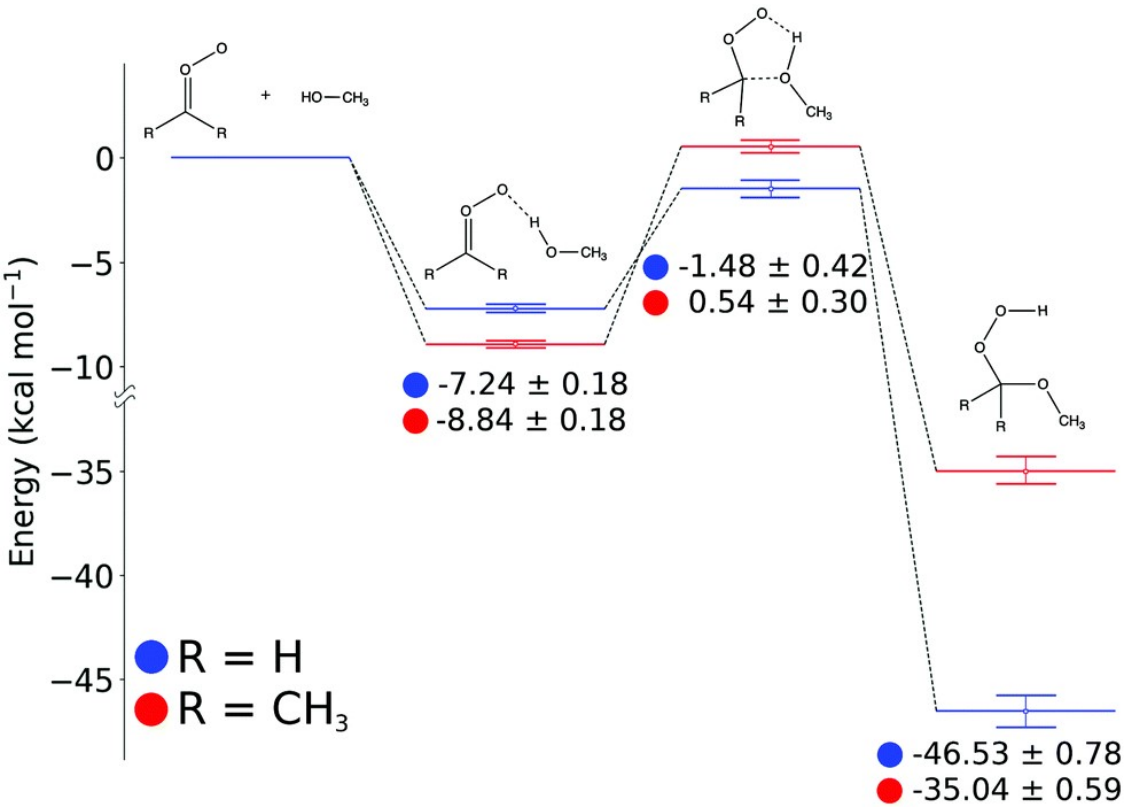

Figure 3.1: Some features of the potential energy surface along the reaction path of the addition of methanol to a Criegee intermediate. Uncertainties are taken as the interval between the CCSD(T)/CBS+Δ and CCSD(T)/CBS+Δ + ΔT(Q) methods, whereas central values are the average of them. Here, $\Delta = \Delta\text{ZPVE}_{\text{ANO1}} + \Delta\text{CORE} + \Delta\text{DBOC} + \Delta\text{REL}$.

3.2 Kinetic Model for Addition Reactions of Criegee Intermediates

The addition reactions for sCI can often be described by a simple kinetic model. The reactions begin with the fast formation of a pre-reactive complex (**PRC**). In the example of our ammonia addition study, the $RR'COO\cdots NH_3$ **PRC** proceeds through the **TS** to the hydroperoxide products in a second step (Equation 3.1)[85]:

$$RR'COO + NH_3 \underset{k_{-1}}{\overset{k_1}{\rightleftharpoons}} RR'COO\cdots NH_3 \xrightarrow{k_2} RR'C(OOH)(NH_2). \tag{3.1}$$

By assuming thermal equilibrium, the steady state approximation, and the condition that $k_2 << k_{-1}$, the rate may be expressed as[85]

$$\begin{aligned} \frac{d[RR'COO\cdots NH_3]}{dt} &= 0 = k_1[RR'COO][NH_3] + (k_{-1} + k_2)[RR'COO\cdots NH_3] \\ &\Longrightarrow [RR'COO\cdots NH_3] = \frac{k_1}{k_{-1} + k_2}[RR'COO][NH_3] \end{aligned} \tag{3.2}$$

$$\begin{aligned} \frac{d[RR'C(OOH)(NH_2)]}{dt} &= k_2[RR'COO\cdots NH_3] \Longrightarrow \\ \frac{d[RR'C(OOH)(NH_2)]}{dt} &= \frac{k_1 k_2}{k_{-1} + k_2}[RR'COO][NH_3] = k_{tot}[RR'COO][NH_3] \\ k_{tot} &= \frac{k_1 k_2}{k_{-1} + k_2} \approx \frac{k_1}{k_{-1}} k_2 = K_{eq} k_2. \end{aligned}$$

At the high-pressure limit, Transition State Theory should predict rate constants and equilibrium constants from the partition functions Q, and relative enthalpies E, of the system's stationary points.

The resulting expressions for K_{eq}, k_2, and k_{tot} at the high pressure limit are:

$$\begin{aligned} \mathrm{K_{eq}(T)} &= \frac{\mathrm{Q_{\mathbf{PRC}}(T)}}{\mathrm{Q_{RR'COO}(T)Q_{NH_3}(T)}}\exp\left(-\frac{\mathrm{E_{stab}}}{\mathrm{k_B T}}\right) \\ \mathrm{k_2(T)} &= \kappa\frac{\mathrm{k_B T}}{\mathrm{h}}\frac{\mathrm{Q_{\mathbf{TS}}(T)}}{\mathrm{Q_{\mathbf{PRC}}(T)}}\exp\left(-\frac{\mathrm{E_a}}{\mathrm{k_B T}}\right) \\ \mathrm{K_{tot}(T) = K_{eq}(T)k_2(T)} &= \kappa\frac{\mathrm{k_B T}}{\mathrm{h}}\frac{\mathrm{Q_{\mathbf{TS}}(T)}}{\mathrm{Q_{RR'COO}(T)Q_{NH_3}(T)}}\exp\left(-\frac{\mathrm{E_a + E_{stab}}}{\mathrm{k_B T}}\right) \end{aligned} \tag{3.3}$$

where κ is the transmission coefficient. For the addition of ammonia to stabilized formaldehyde oxide and *syn*- and *anti*-acetaldehyde oxide, the transmission coefficient, κ, was generated with an unsymmetrical Eckhart potential barrier formed from the stationary point energies and the imaginary frequency along the reactant coordinate.[12]. In our study of methanol, we note the significance that the tunneling contribution can have on accurately predicting the temperature dependence of the rate constants[7].

3.3 Partition Functions for Criegee Intermediates

For both the addition reactions of sCI with methanol and with ammonia, the partition functions, Q, were first approximated by treating each species as a Rigid Rotor Harmonic Oscillator (RRHO), which makes them separable into their rotational, vibrational, translational, and electronic degrees of freedom as $\mathrm{Q} = \mathrm{Q}_{rot}\mathrm{Q}_{vib}\mathrm{Q}_{trans}\mathrm{Q}_{elec}$. The vibrational partition function was calculated with CCSD(T)/ANO2 vibrational frequencies for the simple sCI and CCSD(T)/ANO1 frequencies for *syn*-sCI and *anti*-sCI. We chose rotational constants from the geometries optimized at the same level of theory. We examined the contribution due to hindered internal rotation using the Master Equation System Solver (MESS) partition function solver with a one-dimensional separable rotor

model.[41] For ammonia addition, energy profiles were obtained by performing a constrained optimization at six points along the selection torsional coordinate with M06-2x/def2-TZVP in ORCA 3.03.[88] Hindered-rotor partition functions were computed for each scan and the torsional degrees of freedom were projected out from the Hessian. An updated vibrational partition function was calculated from the remaining normal modes. The df-MP2 code of PSI4 [100] was evoked to scan the dihedral angles of methanol addition.

3.3.1 Hindered rotors for ammonia addition to sCI

Internal hindered rotation, improperly treated, can introduce significant error into the partition function. To analyze this effect, we examined the three hindered rotors that define torsional degrees of freedom in the pre-reactive complex, **PRC**, and transition state, **TS** for the addition of ammonia to formaldehyde oxide: D1 = ϕ(N$\cdots$H$-$O$-$O), D2 = ϕ(C$-$O$-$O$\cdots$H), and D5 = ϕ(H$-$N$\cdots$H$-$O). A fourth torsional degree of freedom, described by the intramolecular torsional angle D3 = ϕ(H$-$C$-$O$-$O), is present in all stages of the reaction. This angle is, however, the cyclization reaction coordinate to form dioxirane. With a torsional barrier of $20-44$ kcal mol^{-1}, it is effectively a rigid rotor for our temperatures.

In general, hindered rotor treatment is most necessary when the rotors have a torsional barrier height near kT and an asymmetrical potential. Criegee intermediates exist primarily in the atmosphere at 298.15 K, prescribing kT = 0.6 kcal mol^{-1}. The energy profiles for the hindered rotors in the **PRC** and **TS** have barriers of $4.8-6.3$ kcal mol^{-1}, and are displayed in Figure S3.2. With barriers within one order of magnitude of kT, we expect that separating the hindered rotors should have a modest effect on the partition function. The hindered rotor partition functions, when applied to calculate k_2 and K_{eq}, produce a value $2\times$ larger than the values computed from the

RRHO partition function. These improvements propagate, forming a k_{tot} that is $5\times$ greater when produced with the hindered rotor model, see Table 3.1. For the *anti*-single methylated sCI, we expect the methyl group to have little impact on the energy of rotation around D1, D2, and D5. We forgo treating the methyl torsion because it behaves as a symmetric rotor. For these reasons, the partition function for the *anti*-sCI is generated using the energy profiles computed formaldehyde oxide. For the *syn*-single methylated sCI, steric effects will only increase the torsional barriers. With only a $2-5\times$ improvement to the unmethylated sCI, see Table 3.1, we expect that using a one-dimension hindered rotor model for *syn*-sCI should not produce substantial improvement to the rate and equilibrium constants.

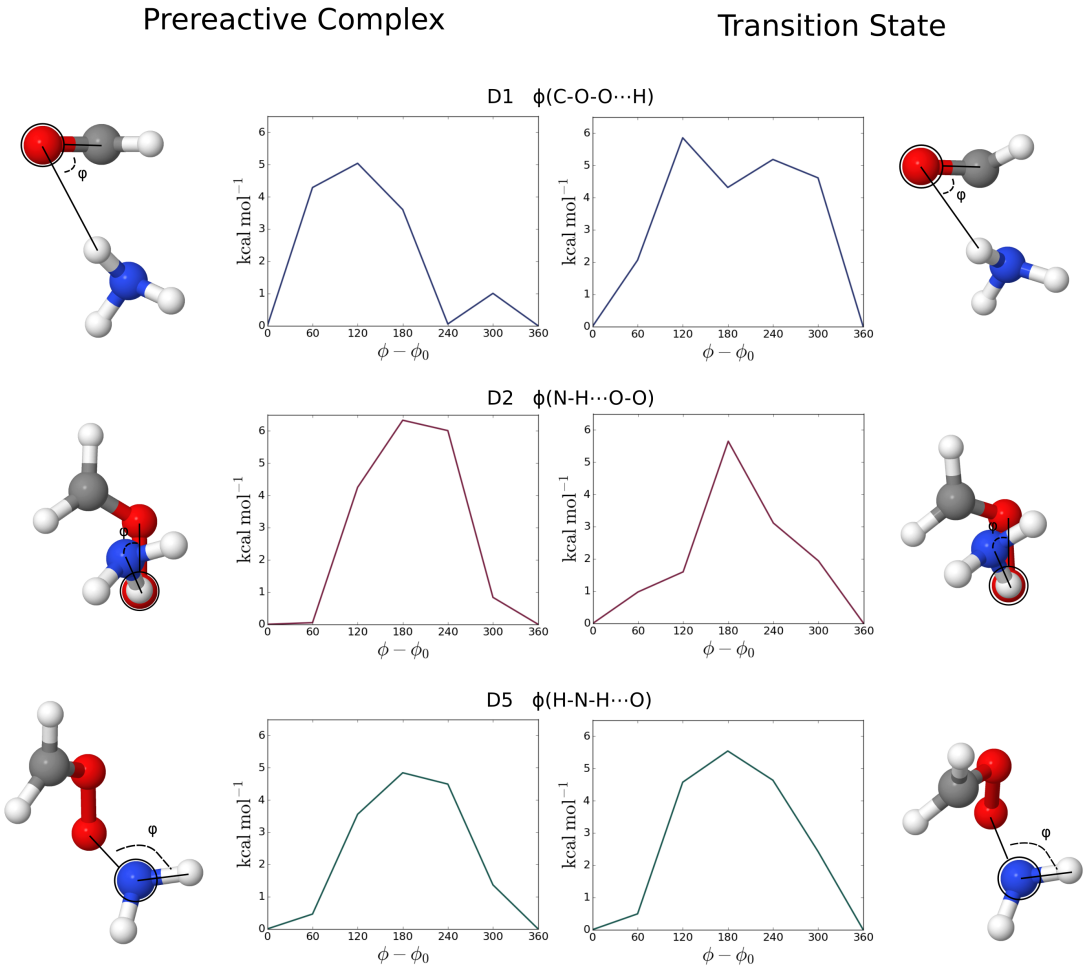

Figure 3.2: Torsional profiles for the hindered rotors of the pre-reactive complex and transition state for $CH_2OO^{\bullet+}NH_3$

Table 3.1: Kinetic properties for the reaction of $ROO + NH_3R(OOH)(NH_2)$ at 298 K. The reaction energy ΔE_0, stabilization energy, E_{stab}, activation energy E_a are presented in kcal mol^{-1}. The equilibrium constant for the first step K_{eq} is cm^3 mol^{-1}, the rate constants for the second step k_2 is s^{-1}, and the total rate constant for the reaction k_{tot} is in cm^3 $mol^{-1}s^{-1}$. *Values are computed using the hindered-rotor partition function.

SCI	ΔE_0	E_{stab}	E_a	κ	K_{eq}	k_2	k_{tot}
H_2COO	-42.11	-4.36	4.79	1.09	1.28×10^{-22}	$1.37 \times 10^{+8}$	1.76×10^{-14}
*H_2COO					3.25×10^{-22}	$2.78 \times 10^{+8}$	9.04×10^{-14}
anti$-CH_2CHCOO$	-39.64	-5.48	5.57	1.11	2.92×10^{-22}	$3.74 \times 10^{+7}$	1.09×10^{-14}
*$anti-CH_2CHCOO$					6.56×10^{-22}	$7.99 \times 10^{+7}$	5.24×10^{-14}
syn$-CH_2CHCOO$	-35.47	-4.24	9.44	1.14	1.14×10^{-22}	$2.38 \times 10^{+4}$	2.70×10^{-18}

3.4 Conclusion

We have successfully modeled the addition of both ammonia and methanol to various sCI via canonical transition state theory and with a kinetic model built by taking the steady-state approximation. Our computed rate constants for methanol addition are shown in Table 3.2, and compared to two experimental findings. Our study on methanol was able to resolve the source of the mixed temperature independence observed in experimental studies [**aroiera2019**]. Similarly, our computed rate constants for the addition of ammonia to formaldehyde oxide, displayed in Table 3.1 are within the experimental uncertainties measured in a subsequent experimental study, by Liu et al.[77].

Table 3.2: Reaction rate constants for the addition of methanol to formaldehyde oxide and acetaldehyde oxide computed using Canonical Transition State Theory (CTST) and available experimental data. In this work, uncertainties are taken as the interval between CCSD(T)/CBS+Δ and the CCSD(T)/CBS+$\Delta+\Delta_{T(Q)}$ computed rates, whereas central values are the average of them.

Ref.	Method	Temperature (K)	k_{tot} (cm^3 s^{-1})
$CH_3OH + H_2COO \longrightarrow CH_3OCH_2OOH$			
Ref. [120]	RRHO[i]	298.15	2.5×10^{-13}
Ref. [135]	RRHO[ii]	298.15	1.2×10^{-14}
This work	RRHO	298.15	$(3.0\pm1.8)\times10^{-14}$
This work	1-D HR	298.15	$(1.2\pm0.8)\times10^{-13}$
Ref. [120]	Experimental	295	$(1.4\pm0.4)\times10^{-13}$
Ref. [81]	Experimental	292.6	$(1.04\pm0.02)\times10^{-13}$
$CH_3OH + (CH_3)_2COO \longrightarrow CH_3OC(CH_3)_2OOH$			
Ref. [135]	RRHO[??]	298.15	5.68×10^{-16}
This work	RRHO	298.15	$(2.8\pm1.3)\times10^{-16}$
This work	1-D HR	298.15	$(2.8\pm1.3)\times10^{-15}$
Ref. [81]	Experimental	292.6	$(4.29\pm0.54)\times10^{-14}$

CHAPTER 4

AUTOMATED THEORETICAL CHEMICAL KINETICS: EXPLORING THE INITIAL STAGES OF PYROLYSIS[1]

[1]Elliott, S. N; Moore, K. B; Copan, A. V.; Keceli, M.; Cavallotti, C.; Georgievskii, Y.; Schaefer, H. F.; Klippenstein, S. J. *Submitted* to the *Proceedings of the Combustion Institute*. 10/8/2019

4.1 Abstract

Large scale implementation of high level computational theoretical chemical kinetics offers the prospect for dramatically improving the fidelity of combustion chemical modeling. To facilitate such efforts we have developed a set of python scripts (AutoMech) that allow for the automatic prediction of the kinetics for a large set of reactions via ab initio transition state theory based master equation calculations. The primary input is simply the mechanism (in ChemKin or JSON format), a dictionary relating chemically identifiable species descriptors (i.e., SMILES or InChIs) to species labels in the mechanism, and a specification of the electronic structure and transition state theory models to be implemented. Here we illustrate the utility of such explorations through a study of the initial stages of pyrolysis for 3 sets of fuels: sequences of alkanes, alcohols, and aldehydes. For simplicity, the analysis focuses on abstractions from the fuel by H, CH3, and OH, and the decomposition of the resulting radicals. Altogether there are a total of 200 reactions in these sets, and the code is successfully produces meaningful rate estimates for 90- 95 % of these. For the radical decomposition reactions, the analysis includes predictions for the pressure dependence of the kinetics. This wide-ranging exploration illustrates (i) the effect of different levels of prediction on the expected accuracy, (ii) the branching between abstractions at different sites for different abstractors, (iii) the dependence of the rates on the chemical structure, and (iv) the variation in radical stabilities across chemical families. These results, as well as the demonstrated feasibility of the methodology, should find further utility in the development of accurate rate exppressions for arbitrary fuels.

4.2 Introduction

The compilation of a detailed chemical kinetic mechanism for fuel combustion is a challenging task due to the vast amount of data required to represent the chemical transformation from fuel to products[24]. The decomposition and ultimate conversion to combustion end products (e.g., CO2 and H2O) and pollutants (e.g., NOx, oxygenated hydrocarbons, and soot) occurs through a bewildering array of pathways. The complete description of the transformations commonly requires the representation of the temperature and pressure dependence of rate coefficients for 103 to 104 reactions, as well as the thermochemical properties for 100 to 1,000 species. Needless to say, it is challenging to obtain well validated values for all of these properties.

Ab initio theoretical kinetics has proven to be a valuable supplement to the combustion modeling enterprise[24, 66]. Careful studies can now yield reactions rate predictions with accuracies equivalent to those of many experiments. As such, it is now fairly commonplace for modeling studies to include ab initio kinetics predictions for a limited number of the most important and/or least studied reactions.

The ever-advancing capabilities of modern computational facilities provides a new opportunity for utilizing such ab initio kinetics. In particular, there is now enough CPU power to make meaningful rate predictions for a large fraction of the reactions in a given mechanism. Ideally, one would make rate predictions for every reaction in a mechanism, thereby reducing the effect of uncertainties in the more crudely estimated reaction rates. However, reaching this ideal is severely limited by the amount of human effort involved in making a single a priori rate prediction.

In recent work, we began to address this issue by developing a procedure (EStokTP) for automatically predicting the rate constant for a single reaction from simple specifications of the molecular structure, and the electronic structure and transition state models[14]. The initial release of the

EStokTP code was limited to a modest set of reaction types: additions, abstractions, and migrations, which nevertheless allows for the treatment of a large fraction of the combustion relevant reactions. Other researchers have focused on the implementation of advanced protocols for mapping the potential energy surface[43, 78], which ultimately determines the reaction kinetics.

The extension to large numbers of reactions requires some form of chemical informatics, where simple chemical identifiers (e.g., SMILES[94]) are used to uniquely specify a chemical species. The use of chemical informatics is a central aspect of advanced combustion modeling programs such as RMG[40]. As a first step in automatically considering large sets of species, we developed a code (QTC) for predicting thermochemical properties for a large set of species[64]. In essence, this code was designed to couple chemical informatics based representations and filesystems with the EStokTP codebase.

In this work, we describe our continuing efforts to completely automate the prediction of the thermochemical kinetics for a full combustion mechanism. Our new AutoMech code[18] builds on the concepts introduced in our EStokTP and QTC efforts, but for a variety of reasons, as discussed below, involves a completely refactored codebase. It is designed to take as input an arbitrary chemical mechanism in ChemKin or JSON format, along with a dictionary relating the species labels in the mechanism to chemical identifiers (currently SMILES or InChI strings). Additional input involves a specification of the electronic structure methods and transition state theory models to be used. The final output is an updated ChemKin formatted chemical mechanism for all the reactions chosen for study. In its current state, it is essentially fully debugged for application of conventional transition state theory with one-dimensional hindered rotor corrections and arbitrary composite electronic structure models to abstractions, additions, and hydrogen migrations. Many other capabilities are in the process of being added.

The current set of capabilities for AutoMech allows for a ready examination of the initial stages of pyrolysis. In particular, the primary decomposition generally involves H-atom abstraction reactions, and the next step involves beta-scission decompositions, which may be preceded by hydrogen migrations. To test the code, and to demonstrate its utility we have applied it to the corresponding set of reactions for an alkane series (C2H6, C3H8, and n-C4H10), an alcohol series (CH3OH, C2H5OH, i-C3H7OH, n-C3H7OH, and n-C4H9OH), and an aldehyde/ketone series [H2CO, CH3CHO, and (CH3)2CO], with H, CH3, and OH as the abstractors. The latter two series are motivated by ongoing collaborations with Wooldridge, where the pyrolysis of i-C3H7OH is being examined in a rapid compression machine, and with Prozument, where the pyrolysis of (CH3)2CO is being examined with chirped pulse microwave spectroscopy in a microreactor. More generally, the data is expected to prove useful in exploring the chemical dependence of total rate constants, branching fractions, and radical stabilities.

4.3 Methodology

4.3.1 Overview of the Automated Workflow

The AutoMechanic code utilized in the present study is designed to fully automate all of the firstprinciples electronic-structure and rate theory calculations necessary to predict the kinetics and thermochemistry of gas-phase reaction mechanisms. It is essentially a refactoring and extension of the ideas introduced in the EStokTP and QTC codes. The primary purpose of the refactoring process was to adopt a functional approach with high-level driver routines working by calling several libraries of simple, low-level functions. Considerable effort was devoted to developing robust error checking versions of the low-level functions. This approach prevents the codes from

becoming monolithic and allows them to be easily extended and adapted for new situations. For example, it is now much easier to utilize arbitrary electronic structure codes and to implement novel aspects of transition state theory. Furthermore, the automated workflow of this code is now fully implemented in Python in order to take advantage its robust I/O capabilities, which is central to the whole automation process.

An illustration of the automated workflow is illustrated in 4.1. Broadly, this workflow can be viewed as a series of drivers in a top-down hierarchy, where the top levels deal with mechanism information, such as reaction channel and rate constants, and low levels deal with species electronic structure data, such as geometries and vibrational frequencies. Depending on the desired input and output, each driver can be run directly by the user, or called by a higher-level driver. To maintain a coherent flow of information, low-level drivers never call drivers above them. Specific details on the drivers are provided later, but here is a brief description:

The Mechanism Driver is a "preprocessing" utility that allows for the investigation of multiple species, reaction channels, or potential energy surfaces (PESs). It analyzes the input mechanism and determines all the unique PESs that make up the mechanism as well as the channels that make up a given PES. kTPDriver and ThermoDriver use the calculated electronic structure data to calculate rate constants and NASA polynomials. Meanwhile, Electronic Structure Driver performs all the requested/required electronic structure calculations.

Each of the drivers operate using a run-save filesystem framework. The run filesystem serves as the working directories where all the electronic structure, thermochemistry, and kinetic calculations are performed, including all of the input and output files. The save filesystem is a series of directories that contains all of the electronic structure data obtained from successful calculations that has been validated to be meaningful during the AutoMechanic run. Since all useful data is stored

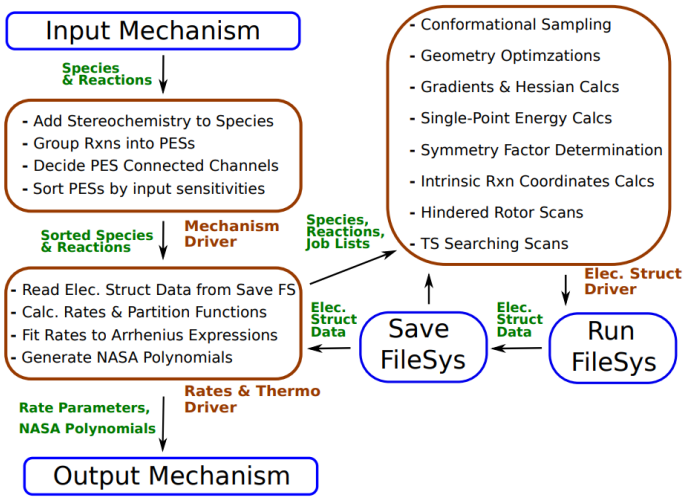

Figure 4.1: Overview of the Workflow in AutoMechanic

in the save filesystem, it can be used as a de facto local database. In contrast, the run filesystem may be safely deleted once the user is satisfied with the results. The interaction with the run-save filesystem is principally simple. Take as an example, the workflow routine gets to a task where it is set to obtain a B2PLYPD3/cc-pVTZ optimized geometry. The code will first check in the save filesystem for this information and read it in from the storage file if it exists. It will only launch a geometry optimization if the geometry does not exist in the filesystem. This feature is critical for minimizing CPU usage for systems of any appreciable size. The structure of the filesystem and the data contained within is enforced by our autofile library, whose functions also handle the creation and modification of the filesystem via calls from the workflow routine.

4.3.2 Description of Workflow Driver Routines

Central Input Information

AutoMechanic currently takes as input a list of reactions in a ChemKin or JSON-formatted file accompanied by a CSV file that relates species names in the reaction file to a unique structural iden-

tifier, such as InChI or SMILES strings. Internally, each of the species are indexed by InChI strings because this identifier allows structures to be generated and indexed with stereospecificity. By extension, this allows us to investigate reactions with proper stereoselectivity maintained throughout, which, although commonly ignored, can significantly affect the reaction rates.

In addition to species and reaction lists, the user specifies how kinetic and thermochemical parameters are calculated by selecting both kinetic "models" for constructing the partition functions, and electronic structure models for calculating the data used in the partition function evaluations. The list of kinetic models available in the program is continually-expanding. Currently, the following models are either available or nearing completion. For rotational partition functions: rigid-rotor harmonic oscillator, one-dimensional, multi-dimensional grid based hindered rotor treatments, and a new path integral based multidimensional rotor analysis. For the transition state partition functions: conventional, variational, variable-reaction coordinate, and phase space theory. For tunneling corrections, Eckart or small curvature tunneling models. For vibrational modes, harmonic or and second order vibrational perturbation theory.

Importantly, these models dictate what electronic structure calculations are required to calculate the kinetic and thermochemical parameters at the desired level of accuracy. For each electronic structure task, one need only specify two electronic structure "levels": (1) the level of theory used to generate a refence geometry used as input for the electronic structure calculation, and (2) the level of theory that the electronic structure theory task is calculated using. For example, a user may wish to do a CCSD(T) calculation on a B2PLYP-D3 optimized geometry. Here B2PLYP-D3 is the first level and CCSD(T) is the second level. These levels include the usual parameters, such as method, basis, convergence options, but also includes job parameters such as program, number of

processes, memory, etc. The user can also employ arbitrary composite methods through sums of any number of user-specified methods.

Mechanism Driver

This driver acts as a "preprocessing" driver that precedes the launching of any kinetic or electronic structure calculations via the other drivers. It is primarily useful when investigating mechanisms with larger numbers of species, reaction channels, or PESs. If multiple reactions are specified as the input, the mechanism driver will go through a two-stage grouping process, whereby reactions are grouped together into potential energy surfaces (PESs), indexed by their stoichiometry. A secondary grouping is conducted on each of these PESs to determine how all the reactions are connected together into distinct reaction channels so that they can be properly treated in the master equation simulations. An important capability afforded by this sorting process is that it allows us to build MESS[41] master equation files with all the channels on a given PES and obtain true multichannel rate-constants.

kTP and Thermo Driver

Given the partition function and electronic structure models, these drivers proceed to search the save filesystem for the required electronic structure information. This information is then collated into a MESS input file, which is then run to obtain the rate constants and/or partition functions as appropriate. This workflow, as well as the electronic structure driver, described below, has many similarities to that described in EStokTP. Due to space limitations we refer the reader to that work for a detailed description[14].

One main advance from the previous approach in EStokTP is that AutoMechanic identifies and the reaction type and generates the requisite internal coordinate descriptions by comparing the structural relationships between the reactant(s) and product(s) molecular graphs. This generalization removes the the need for separate user input for each separate reaction. In this research, we obtained results for abstractions, additions, and isomerizations, whose searching algorithms closely match those in the EStokTP code. However, we have also recently implemented TS searching algorithms for substitution, insertion, and unimolecular elimination reactions, as well as radical-radical abstractions and additions which require unique VTST/VRC-TST treatments based on multireference electronic structure calculations. In keeping with our overall design philosophy, we have made it easy to add in new reaction classes and searching algorithms.

Electronic Structure Driver

This driver executes all of the necessary electronic structure theory jobs, including writing all the input files, running the jobs, and parsing the output files. Currently, the number and order of these jobs are generated by the higher-level kTP and Thermo drivers. This driver serves as the workhorse of the automated workflow, responsible for handling the most CPU-intensive calculations.

One important novel aspect of the AutoMechanic workflow involves the inclusion of robust error checking and resolution for a variety of common electronic structure failures (e.g, failed SCF convergence, geometry convergence, or species convergence in torsional sampling). For instance, given a geometry optimization failure, we are able to launch a sequence of jobs that includes more iterations and/or Hessian calculations to help convergence. In the case of SCF failures, we can modify the SCF algorithm by adding level shifts or damping, or obtain a guess wavefunction using a different method as a guess wavefunction for the desired method.

Another important advancement in the AutoMechanic code is the development of a generalized interface to all electronic structure programs. At this stage, the electronic structure Driver largely consists of calls to this interface, followed by calls to autofile to read and write electronic structure data into the filesystem. This implementation allows the electronic structure interface to be easily extended to new electronic structure codes or new algorithms in supported codes, while simultaneously not requiring large structural changes to the workflow routines.

Currently, we have some level of interface support to the following programs: CFour, Gaussian, Molpro, MRCC, NWChem, Orca, and Psi4. In terms coverage of electronic structure jobs, we can write and read the files for most basic routines, including single-point energy calculations, gradient calculations, geometry optimizations, Hessian calculations. We are also capable of performing intrinsic reaction coordinate calculations and second-order vibrational perturbation theory for codes that support these options. Such code coverage provides intrinsic robustness and versatility to our AutoMechanic, while allowing a multitude of users the ability to use the code, since many electronic structure packages are not free or open-source.

4.4 Results and Discussion

4.4.1 Electronic Structure and Kinetic Treatments for Pyrolysis Reactions

A 200 reaction starting mechanism was generated by considering the H-abstractions by H, CH3, and OH from ethane, propane, n-butane, formaldehyde, acetaldehyde, acetone, methanol, ethanol, i- and n-propanol, and n-butanol. For acetone, we also considered the addition of CH3, H, and OH, to acetone and vinylalcohol. The complete set of reactions so generated is provided in the supplemental material.

For every PES of interest, multichannel, pressure-dependent rate constants [k(T,P)] were calculated via the Master Equation (ME) using the MESS program. The microcanonical rate constants [k(E)] required for the ME treatment were obtained using conventional transition state theory. For all species, nuclear degrees-of-freedom are all treated within the rigid-rotor, harmonic oscillator approximation, with the exception of internal rotations, which are automatically identified from the valence structure, and are modeled as one-dimensional hindered rotors. These rotors are projected out of the Hessian using our ProjRot code[14] and the projected harmonic vibrational frequencies are used in the master equation simulation. Electronic partition functions are obtained from a user specified dictionary or simply taken as the multiplicity. Tunneling effects are treated using a simple Eckart model. For simplicity, generic Lennard-Jones parameters are used to represent the collision rates and energy transfer probabilities are given standard forms.

Three separate sets of mechanism data were generated via the master equation using three different levels of electronic structure theory. This series allow us to examine the variation in the predicted rate constant with electronic structure methods of varying costs. In terms of increasing expected quality of the data, these levels are:

(L1) CCSD(T)-F12/cc-pVDZ-F12//ωB97X-D/6-31G*

(L2) CCSD(T)-F12/cc-pVTZ-F12//ωB97X-D/cc-pVTZ

(L3) CCSD(T)-F12/cc-pVQZ-F12//B2PLYP-D3/cc-pVTZ

(L4) CCSD(T)-F12/CBS(QZ,TZ)//B2PLYP-D3/cc-pVTZ

For each method listed, the given density functional was used to obtain all of the optimized geometries, harmonic vibrational frequencies, and hindered rotor potentials. The given coupled cluster method was used for all the single-point energy computations. For all of the approaches listed above, initial conformational sampling and symmetry factor determination was done at the ωB97X-

D/6-31G* level of theory. The ωB97X-D and B2PLYP-D3 calculations were all performed using Gaussian09[37], whereas CCSD(T)-F12 calculations were done using Molpro2015[137].

4.4.2 Predicted Radical Stability, Rate Constants, and Branching Ratios

One novel feature of the MESS master equation code is its automatic recognition of when the timescale for chemical transformation exceeds that for internal energy relaxation. When this occurs the species is no longer stable, and should be considered as effectively merged with the species obtained from the chemical transformation. Notably, this merging is directly related to the observation from the 1980s, that a lumping of reactions together yields an effective treatment of the decay process at high temperatures[49, 107, 134]. Wang and coworkers have recently followed up on this concept with their HyChem model[145].

In 4.1, we list this merging temperature for each of the radicals studied here. One can observe strong correlations in this temperature with chemical structure. Interestingly, the merging temperature is fairly strongly pressure dependent, suggesting that one should use caution in validating the appropriateness of a lumping scheme at low pressures and then employing it at the higher pressures of relevance to real devices.

The full set of rate constants evaluated here are reported in the Supplementary material through provision of a ChemKin style mechanism file. Overall, we had roughly 95 % success in locating the appropriate transition state with the current algorithms and a similar level of success in predicting meaningful rate coefficients from those transition states. Space limitations preclude detailed discussions of the pratfalls in the process. One simple observation though is that the greatest difficulty is maintaining chemically correct structures at the TS for torsional mappings and samplings.

Table 4.1: Radical Stability Temperatures (K)[a]

Radical	Pressure (atm)			
	P=0.1	P=1	P=10	P=100
C_2H_5	1750	1900	2000	>2000
CH_3CHCH_3	1450	1600	1750	2000
$CH_3CH_2CH_2$	1300	1400	1600	1850
$CH_2CH_2CHCH_3$	1200	1300	1500	1700
$CH_3CH_2CH_2CH_2$	1150	1300	1450	1700
HCO	1700	1750	1800	1900
CH_2OH	>2000	>2000	>2000	>2000
CH_3O	1500	1550	1650	1800
CH_3CO	950	1000	1050	1150
CH_2CHO	650	700	750	850
CH_3CHOH	1600	1750	1950	2000
CH_2CH_2OH	1150	1200	1300	1450
CH_3CH_2O	950	1000	1050	1200
$CH_2C(O)CH_3$	1600	1700	1900	>2000
CH_3CH_2CHOH	1250	1400	1550	1800
$CH_2C(OH)CH_2$	1250	1400	1550	1800
$CH_3C(OH)CH_3$	1250	1400	1550	1750
$CH_2CH_2CH_2OH$	1150	1300	1500	1800
$CH_3CH(OH)CH_2$	1100	1200	1300	1400
$CH_2CH(OH)CH_3$	1100	1200	1400	1650
CH_3CHCH_2OH	1000	1100	1200	1400
$CH_3CH(O)CH_3$	650	700	800	900
$CH_3CH_2CH_2O$	650	700	750	900
$CH_3CH_2CH_2CHOH$	1150	1300	1500	1800
$CH_3CH_2C(OH)CH_3$	1150	1250	1400	1650
$CH_3CH_2CHCH_2OH$	1050	1200	1350	1600
$CH_2CH_2CH_2CH_2OH$	750	1050	1350	1600
$CH_3C(CH_3)OCH_3$	800	850	1000	1150
$CH_3C(O)(CH_3)_2$	600	650	700	850

[a]Determined on a 50 K temperature grid.

Employing smaller torsional grid steps (e.g. 10 degrees) helps ameliorate the latter, while robust structure checking was implemented for the sampling.

Table 4.2: Molecule-Radical Abstraction (Abs) Rate Constants (at 1000 K) and Branching Fractions (BF)

Molecule	Abs	Product	Rate Constants	BF
C_2H_6	H	C_2H_5	2.50E+12	
C_2H_6	CH_3	C_2H_5		
C_2H_6	OH	C_2H_5	2.10E+13	
C_3H_8	H	CH_3CHCH_3	1.20E+12	0.59
C_3H_8	H	$CH_2CH_2CH_3$	8.10E+11	0.41
		Total	2.00E+12	
C_3H_8	CH_3	CH_3CHCH_3	3.70E+09	0.57
C_3H_8	CH_3	$CH_2CH_2CH_3$	2.80E+09	0.43
		Total	6.60E+09	
C_3H_8	OH	CH_3CHCH_3	7.00E+12	0.67
C_3H_8	OH	$CH_2CH_2CH_3$	$3.40E_{12}^{+}$	0.33
		Total	$1.00E_{13}^{+}$	
C_4H_{10}	CH_3	$CH_3CHCH_2CH_3$	$6.30E_{09}^{+}$	0.63
C_4H_{10}	CH_3	$CH_2CH_2CH_2CH_3$	$3.70E_{09}^{+}$	0.37
		Total	$1.00E_{10}^{+}$	
C_4H_{10}	H	$CH_3CHCH_2CH_3$	2.20E+12	0.72
C_4H_{10}	H	$CH_2CH_2CH_2CH_3$	8.50E+11	0.28
		Total	3.10E+12	
C_4H_{10}	OH	$CH_3CHCH_2CH_3$	4.80E+12	0.56
C_4H_{10}	OH	$CH_2CH_2CH_2CH_3$	3.70E+12	0.44
		Total	8.50E+12	
H_2CO	H	HCO	3.60E+12	
H_2CO	CH_3	HCO	5.80E+10	
CH_3CHO	H	CH_2CHO	3.10E+11	0.09
CH_3CHO	H	CH_3CO	3.10E+12	0.91
		Total	3.50E+12	
CH_3CHO	CH_3	CH_2CHO	2.60E+09	0.12
CH_3CHO	CH_3	CH_3CO	1.90E+10	0.88
		Total	2.20E+10	
CH_3CHO	OH	CH_2CHO	1.40E+12	
$CH_3C(O)CH_3$	H	$CH_2C(O)CH_3$	6.70E+11	
$CH_3C(O)CH_3$	CH_3	$CH_2C(O)CH_3$	6.10E+09	

$CH_3C(O)CH_3$	OH	$CH_2C(O)CH_3$	3.90E+12	
$CH_2C(OH)CH_3$	H	$CH_2C(OH)CH_2$	6.40E+11	0.77
$CH_2C(OH)CH_3$	H	$CH_2C(O)CH_3$	1.90E+11	0.23
$CHC(OH)CH_3$	H_2	$CH_2C(OH)CH_3$	1.10E+11	
		Total	8.20E+11	
$CH_2C(OH)CH_3$	CH_3	$CH_2C(O)CH_3$	7.80E+09	0.68
$CH_2C(OH)CH_3$	CH_3	$CH_2C(OH)CH_2$	3.70E+09	0.32
$CHC(OH)CH_3$	CH_4	$CH_2C(OH)CH_3$	1.80E+10	
		Total	1.20E+10	
$CH_2C(OH)CH_3$	OH	$CH_2C(O)CH_3$	7.30E+11	0.5
$CH_2C(OH)CH_3$	OH	$CH_2C(OH)CH_2$	6.10E+11	0.42
$CH_2C(OH)CH_3$	OH	$CHC(OH)CH_3$	1.10E+11	0.08
		Total	1.40E+12	
CH_3OH	H	CH_2OH	7.40E+11	
CH_3O	H_2	CH_3OH	1.40E+10	
CH_3OH	CH_3	CH_2OH	3.20E+09	
CH_3O	CH_4	CH_3OH	1.30E+10	
CH_3OH	OH	CH_2OH	2.00E+12	0.81
CH_3OH	OH	CH_3O	4.60E+11	0.19
		Total	2.40E+12	
C_2H_5OH	H	CH_3CHOH	1.50E+12	0.84
C_2H_5OH	H	CH_2CH_2OH	2.10E+11	0.12
C_2H_5OH	H	CH_3CH_2O	6.10E+10	0.03
		Total	1.80E+12	
C_2H_5OH	CH_3	CH_3CHOH	5.00E+09	0.65
C_2H_5OH	CH_3	CH_2CH_2OH	1.30E+09	0.16
C_2H_5OH	CH_3	CH_3CH_2O	1.50E+09	0.19
		Total	7.70E+09	
C_2H_5OH	OH	CH_3CHOH	2.00E+12	
C_2H_5OH	OH	CH_2CH_2OH	3.10E+11	
C_2H_5OH	OH	CH_3CH_2O		
		Total	5.30E+13	
iC_3H_7OH	H	$CH_3C(OH)CH_3$	2.20E+12	0.86
iC_3H_7OH	H		3.50E+11	0.14
		Total	2.60E+12	
iC_3H_7OH	CH_3	$CH_3C(OH)CH_3$	6.90E+09	
iC_3H_7OH	CH_3	$CH_3CH(OH)CH_2$	2.10E+09	
$CH_3CH(O)CH_3$	CH_4	iC_3H_7OH	1.40E+10	
		Total	9.00E+09	

iC_3H_7OH	OH	$CH_3C(OH)CH_3$	6.30E+11	0.02
iC_3H_7OH	OH	$CH_3CH(O)CH_3$	3.30E+13	0.99
iC_3H_7OH	OH	$CH_3CH(OH)CH_2$	4.60E+11	0.01
		Total	3.30E+13	
nC_3H_7OH	CH_3	$CH_2CH_2CH_2OH$	8.80E+08	0.13
nC_3H_7OH	CH_3	CH_3CH_2CHOH	4.90E+09	0.71
nC_3H_7OH	CH_3	CH_3CHCH_2OH	2.00E+09	0.29
$CH_3CH_2CH_2O$	CH_4	nC_3H_7OH	1.60E+11	
		Total	6.80E+09	
nC_3H_7OH	H	$CH_2CH_2CH_2OH$	7.90E+11	0.26
nC_3H_7OH	H	CH_3CH_2CHOH	1.70E+12	0.57
nC_3H_7OH	H	CH_3CHCH_2OH	5.30E+11	0.17
$CH_3CH_2CH_2O$	H_2	nC_3H_7OH	2.40E+10	
		Total	3.00E+12	
nC_3H_7OH	OH	CH_3CH_2CHOH	2.10E+12	0.91
nC_3H_7OH	OH	CH_3CHCH_2OH	2.10E+11	0.09
		Total	2.30E+12	
nC_4H_9OH	H	$CH_3CH_2CH_2CHOH$	8.80E+11	0.69
nC_4H_9OH	H	$CH_3CHCH_2CH_2OH$	3.40E+11	0.27
nC_4H_9OH	H	$CH_3CH_2CH_2CH_2O$	5.70E+10	0.05
		Total	1.30E+12	
nC_4H_9OH	CH_3	$CH_3CH_2CH_2CHOH$	2.20E+11	0.98
nC_4H_9OH	CH_3	$CH_3CHCH_2CH_2OH$	2.00E+09	0.01
nC_4H_9OH	CH_3	$CH_2CH_2CH_2CH_2OH$	1.30E+09	0.01
nC_4H_9OH	CH_3	$CH_3CH_2CHCH_2OH$	1.20E+09	0.01
$CH_3CH_2CH_2CH_2O$	CH_4	nC_4H_9OH	4.60E+10	
		Total	2.30E+11	
nC_4H_9OH	OH	$CH_3CH_2CH_2CHOH$	2.90E+12	0.97
nC_4H_9OH	OH	$CH_3CH_2CHCH_2OH$	9.70E+10	0.03
		Total	3.00E+12	

[a] Calculated at level L1.

A limited subset of the calculated rate constants are reported in 4.2 (for abstraction) and Table 4.3 for the remaining pressure dependent reactions. Again, there are interesting correlations in the predicted rate constants and branching fractions that can be used to refine groups and other chemistry based rate rules. In Table 4.1 we demonstrate the ability of the L1 approach to make

predictions for essentially all the abstractions of interest. The primarly difficulties encountered were for the abstractions in alcohols by OH group, since the barrier can be quite deeply submerged in those cases. For the pressure dependent reactions, similar difficulties were encountered for the OH addition to molecules with pi-bonds, which may or may not have a short-range saddle point depending on the theoretical method[67]. The VTST methods under development will improve our treatment of those channels.

Table 4.3: Pressure Dependent Rate Constants for Reactions on the Fuel Radical Potential Energy[a]

Reactants(s)		Products(s)	Pressure (Atm)[b] 1.0	10.0	100.0
		Addition			
C_2H_4	H	C_2H_5	4.7E+12	1.1E+13	1.7E+13
CO	H	HCO	1.0E+10	8.0E+10	5.6E+11
H_2CO	H	CH_2OH	6.8E+10	2.1E+11	4.4E+11
H_2CO	H	CH_3O	4.4E+10	2.4E+11	8.8E+11
$CH_3C(O)CH_3$	H	$CH_2CH(OH)CH_3$	1.2E+07	4.4E+07	7.5E+07
$CH_3C(O)CH_3$	H	$CH_3C(OH)CH_3$	5.6E+10	1.2E+11	1.8E+11
$CH_3C(O)CH_3$	H	$CH_3CH(O)CH_3$	2.3E+07	4.3E+08	5.3E+09
$CH_2C(OH)CH_3$	H	$CH_2CH(OH)CH_3$	3.9E+10	1.9E+11	4.7E+11
$CH_2C(OH)CH_3$	H	$CH_3C(OH)CH_3$	3.3E+12	1.1E+13	2.0E+13
$CH_2C(OH)CH_3$	H	$CH_3CH(O)CH_3$	2.4E+06	2.5E+07	1.8E+08
CH_2CCH_2	OH	$CH_2C(O)CH_3$	4.7E+08	1.9E+09	2.6E+09
CH_2CCH_2	OH	$CH_2C(OH)CH_2$	1.7E+12	2.4E+12	2.6E+12
CH_2CCH_2	OH	$CHC(OH)CH_3$	4.6E+07	1.1E+08	9.3E+07
CH_3CCH	OH	$CH_2C(O)CH_3$	1.6E+08	2.3E+09	5.6E+09
CH_3CCH	OH	$CH_2C(OH)CH_2$	1.4E+09	1.9E+09	9.8E+08
CH_3CCH	OH	$CHC(OH)CH_3$	7.9E+10	2.3E+11	4.2E+11
CH_2CHCH_3	OH	$CH_2CH(OH)CH_3$	4.3E+11	1.1E+12	1.9E+12
CH_2CHCH_3	OH	$CH_3C(OH)CH_3$	1.2E+08	5.1E+08	6.5E+08
CH_2CHCH_3	OH	$CH_3CH(O)CH_3$	8.4E+04	5.7E+05	3.6E+06
CH_2CO	CH_3	$CH_2C(O)CH_3$	9.9E+08	2.0E+09	2.7E+09
HCCOH	CH_3	$CH_2C(O)CH_3$	1.2E+05	1.0E+07	1.1E+08
HCCOH	CH_3	$CH_2C(OH)CH_2$	1.7E+07	5.8E+07	5.8E+07
HCCOH	CH_3	$CHC(OH)CH_3$	4.9E+07	8.3E+08	4.1E+09
CH_3CHO	CH_3	$CH_2CH(OH)CH_3$	6.0E+04	1.8E+05	3.4E+05
CH_3CHO	CH_3	$CH_3C(OH)CH_3$	4.7E+05	1.2E+06	2.1E+06
CH_3CHO	CH_3	$CH_3CH(O)CH_3$	2.7E+06	2.3E+07	1.5E+08
CH_2CHOH	CH_3	$CH_2CH(OH)CH_3$	1.8E+08	7.3E+08	1.6E+09
CH_2CHOH	CH_3	$CH_3C(OH)CH_3$	8.6E+04	5.4E+05	9.3E+05
		Isomerization			
CH_3O		CH_2OH	3.4E+04	2.2E+05	1.3E+06
$CH_2C(OH)CH_2$		$CH_2C(O)CH_3$	3.0E+01	1.5E+02	3.5E+02

$CHC(OH)CH_3$	$CH_2C(O)CH_3$	1.8E+04	3.0E+05	1.5E+06
$CHC(OH)CH_3$	$CH_2C(OH)CH_2$	3.8E+03	1.7E+04	4.1E+04
$CH_3CH(O)CH_3$	$CH_3C(OH)CH_3$	3.9E+03	9.1E+04	1.7E+06
$CH_2CH(OH)CH_3$	$CH_3C(OH)CH_3$	4.8E+02	5.4E+03	2.4E+04
$CH_3CH(O)CH_3$	$CH_2CH(OH)CH_3$	1.9E+02	6.0E+03	1.6E+05

Addition Elimination

$CH_2C(OH)CH_3$	H	CH_2CHOH	CH_3	1.5E+11	1.2E+11	5.7E+10
$CH_2C(OH)CH_3$	H	$CH_3C(O)CH_3$	H	1.4E+13	8.9E+12	3.1E+12
$CH_2C(OH)CH_3$	H	CH_3CHO	CH_3	4.7E+11	3.1E+11	1.2E+11
CH_2CCH_2	OH	CH_2CO	CH_3	3.6E+11	8.7E+10	1.0E+10
CH_2CCH_2	OH	CH_3CCH	OH	3.7E+09	1.3E+09	1.8E+08
CH_3CCH	OH	CH_2CO	CH_3	1.2E+11	6.7E+10	1.7E+10
CH_2CHCH_3	OH	$CH_2C(OH)CH_3$	H	2.5E+10	1.9E+10	7.8E+09
CH_2CHCH_3	OH	$CH_3C(O)CH_3$	H	2.7E+09	1.7E+09	5.3E+08
CH_2CHCH_3	OH	CH_3CHO	CH_3	8.8E+09	5.6E+09	2.0E+09
CH_2CHCH_3	OH	CH_2CHOH	CH_3	3.5E+11	2.4E+11	9.4E+10
CH_2CHOH	CH_3	CH_3CHO	CH_3	9.5E+06	6.8E+06	2.9E+06
HCCOH	CH_3	CH_2CO	CH_3	1.8E+09	1.6E+09	7.9E+08
HCCOH	CH_3	CH_2CCH_2	OH	7.0E+07	3.6E+07	7.6E+06
HCCOH	CH_3	CH_3CCH	OH	6.8E+09	6.2E+09	3.6E+09

[a] Calculated with level L3.

[b] Rate constants in units of s^{-1} for unimolecular reactions and $cm^3\ mol^{-1}\ s^{-1}$ for bimolecular reactions.

Performing detailed comparisons with experiment for as many reactions as were studied here is extremely time-consuming. As such, it was considered beyond the scope of this work. Nevertheless, cursory comparison with the extensive data from Michael and Sivaramakrishnan on reactions such as H, CH3 and OH with alkane and alcohols[102, 103, 113] suggest that the present CCSD(T)-F12/DZ-F12//ωB97XD6-31g* based calculations have accuracies of about a factor of 2-3 near 1000 K. Such errors are to be expected for such modest methodologies, which are readily applicable to much larger systems. More extensive comparisons of theory and experiment across a wide series of reactions is an important topic for future work.

In 4.2, we provide an illustrative comparison of the predictions obtained with levels 2 and 3 for a specific reaction. Our automated parsing routines allow us to make such comparison for the full set of reactions studied. Complete comparisons of levels 2 and 3 are provided in the supplementary material.

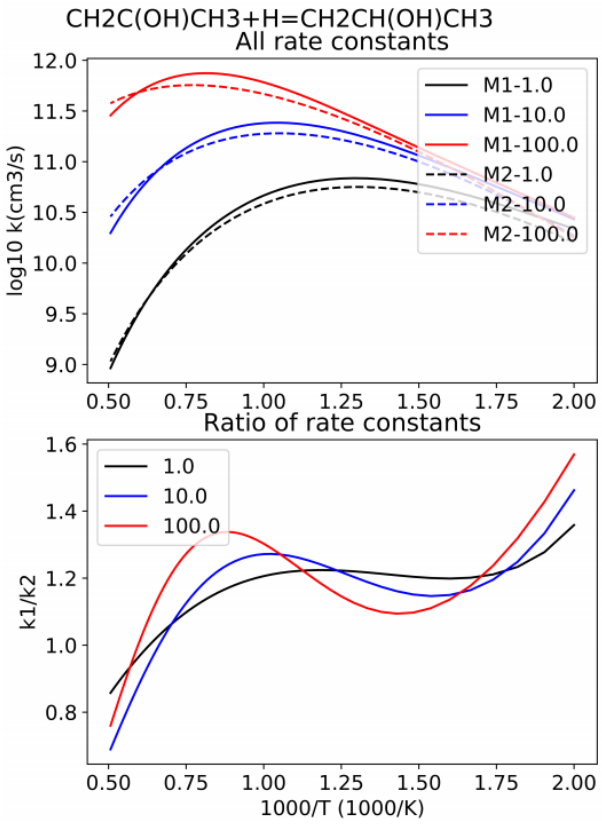

Figure 4.2: Illustration of the difference between rate predictions obtained with L2 and L3 methods (M1 and M2, respectively).

4.5 Conclusion

The automatic prediction of rate constants has been demonstrated for a set of reactions of relevance to the initial stages of pyrolysis in series of alkane, alcohol, and aldehyde fuels. The results allow for useful exploration of correlations in radical stability, chemical branching, total rate constants,

and pressure dependence rate constants. ChemKin style mechanism files are used to report the full set of calculations.

4.6 Acknowledgements

This research was supported by the Exascale Computing Project (ECP), Project Number: 17-SC20-SC, a collaborative effort of two U.S. Department of Energy (DOE) organizations, the Office of Science and the National Nuclear Security Administration, responsible for the planning and preparation of a capable exascale ecosystem including software, applications, hardware, advanced system engineering, and early test bed platforms to support the nation's exascale computing imperative. This research was conducted using the Blues and Bebop computing resources, two high-performance computing clusters operated by the Laboratory Computing Resource Center at Argonne National Laboratory. This material is based on work supported by the DOE, Office of Science, Office of Basic Energy Sciences, Division of Chemical Sciences, Geosciences, and Biosciences at Argonne under Contract No. DE-AC02-06CH11357. Several authors of this research also wish to acknowledge additional support. Kevin Moore acknowledges support from the U. S. Army Research Office under award number W911NF1710531. Lastly, Sarah Elliott gratefully acknowledges support from a DOE Computational Sciences Graduate Fellowship through grant number DE-FG02-97ER25308.

CHAPTER 5

HIGH-LEVEL THERMOCHEMISTRY FOR CORE COMBUSTION SPECIES[1]

[1]Elliott, S. N.; Keceli, M.; Cavallotti, C.; Georgievskii, Y.; Klippenstein, S. J.; and Schaefer, H. F. *To be Submitted* to the *Journal of Physical Chemistry A*.

5.1 Abstract

Recent progress in theoretical methodologies and computational capabilities make highly-predictive combustion modeling possible. These models rely heavily on the thermochemical parameters of a set of core combustion intermediates and products. We carry out high-level treatments for the partition functions of these 348 species to provide enthalpies, entropies, heat capacities, and free energies from a range of 0-3000 K. We have automated this process through Autochem, a software package we are currently developing for combustion simulation. Autochem facilitates our analysis of a series of computational protocols which involve several treatments of anharmonicities and nonlocal motions. In doing so, we build up from RRHO partition functions by including rovibrational and anharmonic constants from VPT2 analysis, and one, two, and three dimensional torsional energy and frequency profiles. Simultaneously, we examine the sensitivity of the thermochemical parameters to the selection of electronic structure method when computing the molecular geometries, harmonic and fundamental frequencies, and torsional energy profiles. Ultimately we present geometries, frequencies, anharmonic constants, and torsional profiles determined with B2PLYP-D3/cc-pVTZ and pair it with high-level 0 K heats of formation to build an *ab initio*, anharmonic, and adiabatic multicore partition function for each core combustion species. We convert these into NASA polynomials and thermochemical properties at 300, 500, 1000, 2000, and 3000 K.

5.2 Introduction

Combustion simulation demands a union of a wide range of scientific disciplines. In itself, the computational fluid dynamics (CFD) simulations require both sophisticated numerical treatment and accurate chemical parameters. These chemical parameters describe the conversion of a fuel into combustion products, and are comprised of the thermodynamic and transport properties and the rate constants for the elementary chemical reactions in a chemical mechanism. Even with the most advanced approaches to computational kinetics, CFD, and mechanism optimization, a combustion simulation will only be as reliable as the thermochemical information it is based upon.

The mechanisms for the combustion of larger fuels strongly depend on components that are described in the combustion of smaller fuels. As such, H_2/O_2 is considered the base mechanism for combustion. A core combustion mechanism can be established by including models for up to C3 hydrocarbons and oxygenated C2 hydrocarbons. We add nitrogen to this core mechanism to better describe NOx formation. In previous work [68], we studied this core combustion set, labeled **ANL0**, of 348 C, N, O, and H containing species with 34 or fewer electrons, and a subset, called **ANL1**, of 150 species. This database for core combustion species provides highly accurate electronic energies and frequencies, and ultimately 0 K heats of formation at estimated 2σ uncertainties within the range of 1.0-1.5 kJ/mol. We will extend upon the database for **ANL0** and **ANL1** to provide thermochemical properties, including enthalpies, entropies, free energies, and heat capacities up to 3000 K. This involves several treatments for the vibrational, torsional, anharmonic modes of the species, evaluation of their partition functions, and translation into NASA polynomial representation of the temperature dependence.

Well designed, high-level, *ab initio* electronic structure schemes, like those used for the **ANL0** and **ANL1** databases, can now surpass the typical goal of thermochemical accuracy, 1 kcal/mol,

for 0 K heats of formation. Such accuracy, if reached for all the parameters that make up the chemical model, make predictive combustion modeling possible. Entire combustion mechanisms, however, can become extremely large. In order to capture all of the intermediates and products formed during the conversion of a fuel to its oxidation products, and to catch the formation of any pollutants, the models need to characterize thousands of reactions and the thermochemistry for the species involved in each of them. Each reaction can require hundreds of calculations in order to to verify the location of the stationary points and to treat the energetic degrees of freedom carefully. The magnitude of this task has motivated the several efforts to automate the process[10, 63, 86, 128, 129, 151]. We are developing a large-scale, high-level, automated combustion chemistry modeling software package called Autochem, which brings together many of these efforts along with its own libraries of python functions and drivers. This goal of this software package is to provide a unified interface for mechanism generation and reduction, electronic structure theory, transition state theory, classical trajectory simulations, the master equation, and uncertainty analysis tools. We have presented the effectiveness of applying this package in the pyrolysis of arbitrary fuels to solve the thermochemistry in butane oxidation[63, 86].

We now we apply Autochem to the thermochemistry of core combustion species. The sheer volume of DFT functionals and basis sets to choose between during an *ab initio* computation leaves significant ambiguity when determining the most suitable method for combustion chemistry. Certainly different applications shift the required balance between reliability, cost, and error-cancellation. The Autochem procedures, applied to the **ANL0** and **ANL1** databases, provide an opportunity to examine various *ab initio* electronic structure schemes. In previous work**??** we compared against ATcT and experimental data to suggest where computational cost can be mitigated for the **ANL1** set of core combustion molecules. In particular, we examined the effect of electronic

structure level of theory to the fundamental properties – including rotational constants, harmonic and anharmonic frequencies, and electronic energies. For these properties, we determined that the B2PLYP-D3 functional paired with the cc-pVTZ basis set provides an affordable approximation of CCSD(T)/CBS results for the ANL1 set. Now we examine the sensitivity of partition functions and resulting thermochemistry of each molecule to these properties. We also examine several hindered rotor treatments, namely: one-dimensional, multi-dimensional, and adiabatic multi-dimensional treatments. We pair these profiles with second order vibrational perturbation theory to provide rovibrational anharmonic properties.

5.3 Theoretical Methods

High-accuracy electronic structure predictions are essential to combustion modeling, which amplifies any uncertainty in the computed heat of formation for a species. Each error of kT in the barrier height of a reaction – 0.6 kcal mol^{-1}at 298 K – impacts the rate constant by over a factor of two. Previous work found that coupled cluster theory and composite energy schemes can achieve electronic energies within chemical accuracy[68]. Frequencies and anharmonic constants must be computed carefully as well, because they contribute to the barrier height through the ZPVE. Moreover, each frequency for a molecule directly factors into its partition function, which determines the temperature dependence of its properties. The scarcity of experimental thermochemical data at combustion temperatures, however, requires that combustion models depend on theoretical predictions. Treating each energetic degree of freedom carefully comes at high computational cost. We explore high-level treatments for the geometries, frequencies, and electronic energies to establish reliable

information for the core combustion species. That information, in turn, establishes a database to assess the viability of more affordable methods.

5.3.1 0 K Heats of Formation

In our temperature independent investigation on the **ANL0** and **ANL1** sets we found 0 K heats of formation with CCSD(T)/aug-cc-pVnZ methods (n= Q, 5, or 6) towards the complete-basis-set [CBS] limit on CCSD(T)/cc-pVnZ (n=T,Q) geometries, and included corrections for anharmonic contributions to the zero point vibrational energy [ZPVE], higher-order excitations in the Coupled Cluster theory [CCSDT(Q), CCSDTQ(P)], core-valence interactions [Full], Douglass Kroll Hamiltonian relativistic effects [DKH][142], diagonal Born-Oppenheimer effects [DBOC], and spin-orbit effects [SO] with H_2, CH_4, H_2O, and NH_3 as reference molecules.

$$\begin{aligned} E_{\text{ANL0}} = & E_{\text{CCSD(T)/CBS(a'Qz,a'5z)//CCSD(T)/TZ}} + E^{\text{ZPVE,har}}_{\text{CCSD(T)/TZ}} \\ & + \left(E^{\text{ZPVE,anh}}_{\text{B3LYP/TZ}} - E^{\text{ZPVE,har}}_{\text{B3LYP/TZ}}\right) \\ & + \left(E_{\text{CCSDT(Q)/DZ}} - E_{\text{CCSD(T)/DZ}}\right) \\ & + \left(E_{\text{CCSD(T,Full)/CBS(cTZ,cQZ)}} - E_{\text{CCSD(T)/CBS(cTZ,cQZ)}}\right) \\ & + \Delta E_{\text{DKH/CCSD(T)/a'cTZ}} + \Delta E_{\text{DBOC/HF/TZ}} + \Delta E_{\text{SO}} \end{aligned} \tag{5.1}$$

$$
\begin{aligned}
E_{\text{ANL1}} = & E_{\text{CCSD(T)/CBS(a'5z,a'6z)//CCSD(T)/QZ}} + E^{\text{ZPVE,har}}_{\text{CCSD(T)/CBS(TZ,QZ)}} \\
& + (E^{\text{ZPVE,anh}}_{\text{B3LYP/TZ}} - E^{\text{ZPVE,har}}_{\text{B3LYP/TZ}}) \\
& + (E_{\text{CCSDT(Q)/TZ}} - E_{\text{CCSD(T)/TZ}}) \\
& + (E_{\text{CCSDTQ(P)/DZ}} - E_{\text{CCST(Q)/DZ}}) \\
& + (E_{\text{CCSD(T,Full)/CBS(cTZ,cQZ)}} - E_{\text{CCSD(T)/CBS(cTZ,cQZ)}}) \\
& + \Delta E_{\text{DKH/CCSD(T)/a'cTZ}} + \Delta E_{\text{DBOC/HF/TZ}} + \Delta E_{\text{SO}}
\end{aligned}
\tag{5.2}
$$

By examining the magnitudes of these corrections and comparing against ATcT[108] values, we estimated 2σ uncertainties for the **ANL1** set as 0.9 kJ/mol and for **ANL0** within 1.5 kJ/mol. We use these highly reliable values for the 0 K heat of formation for our thermochemical properties. The uncertainty in our calculations, then, largely will be determined by our partition function build.

5.3.2 Geometries and Vibrational Frequencies

Autochem affords the ability to investigate many DFT functionals compared to wavefunction based methods. We began by isolating the **ANL1** subset, containing species that have up to 22 electrons. Utilizing Autochem, we automated their geometry optimization with the following routine. Autochem achieved a starting molecular structure for each species with OpenBabel[95]. It then translated those geometries to internal coordinates and improved upon them by carrying out a conformer search through EStokTP[15]. The EStoKTP program used Gaussian09[36] to optimize starting coordinates that it chose with Monte Carlo sampling over the torsional coordinates. The number of points was the lesser of 100 and $8+1^{3n}$, where n is the number of rotors. For each unique conformer discovered, a more rigorous constrained optimization along each torsional angle reinforced the location of its minimum. In several cases, the torsional scan identified a lower energy

conformation. A subsequent vibrational frequency analysis provided a final confirmation of the geometries.

Ultimately, we carry out computations using several DFT functionals, including the most popular B3LYP [9, 74], ωb97xD of Head-Gordon [16], M06-2X of Truhlar and Zhao [149], and B2PLYP-D3 of Grimme [45]. We paired these with the 6-31G* double-zeta Pople basis set [35] and the cc-pVTZ and cc-pVQZ, triple- and quadruple-zeta, Dunning basis sets [28] to arrive at: (M1) B3LYP/6-31G*, (M2) B3LYP/cc-pVTZ, (M3) ωb97xD/cc-pVTZ, (M4) M06-2X/cc-pVTZ, (M5) B2PLYP-D3/cc-pVTZ, and (M6) B2PLYP-D3/cc-pVQZ. For X=1-4 the Monte Carlo sampling and subsequent optimization and frequency analysis all occurs at the MX level of theory, whereas for M4 and M5 the Monte Carlo sampling is at ωb97xD/cc-pVTZ while the subsequent optimization and frequency analysis is at the B2PLYP-D3/cc-pVxZ (x=T or Q). We also carried out second order vibrational perturbation theory with each M1-M5 method. Autochem then called Molpro to run f12-CCSD(T)/cc-pVTZ-f12 [69] single point energy evaluations at the geometries obtained with each of these methods to determine their suitability when compared to the **ANL0/ANL1** 0 K heats of formation from Ref. [68]. In a recent study[**part1**] we carried out an exhaustive analysis of these approaches and the sensitivity of the rotational constants, frequencies, and single point energies to the choice of optimization routine. Here we extend the analysis to discern the sensitivity of the partition function, and resulting thermochemical properties. In addition, we apply the DFT computations to the 348 **ANL0** species.

5.3.3 Partition Function

The geometries, rotational constants, fundamental frequencies, and electronic energies determined by these electronic structure methods parameterize Rigid Rotor Harmonic Oscillator partition func-

tions (Q_{RRHO}). At combustion temperatures, and when the RRHO parameters are highly reliable, the major sources of error stem from anharmonicities and high amplitude motions.

Anharmonicities

A recent study by Ahren *et. al* found that at 2500 K anharmonic corrections for each vibrational mode increased the partition function by 3% on average. We provide rovibrational, anharmonic partition functions ($Q_{RRHO,anh}$) using the approach of Wooley et. al[144] by interfacing Autochem to the Master Equation System Solver. We determine anharmonic constants, rovibrational constants, and quartic rotational distortion constants with second order vibrational perturbation theory (VPT2). Vibrational perturbation theory, while appealing for computational efficiency breaks down when there are umbrella inversion or large amplitude motions present. For this we introduce the perturbation parameter:

$$\lambda_{ij} = \frac{kTx_{ij}}{\omega_i \omega_j} \tag{5.3}$$

which comes from expanding the anharmonic constant coupling modes i and j, $x_i j$, for high T. We have chosen a threshold of $\lambda_{ij} = 0.65$, at which we zero out the corresponding row and column in the anharmonic constant matrix.

Torsions

The large amplitude modes can be treated by hindered rotor treatment. Autochem calls EStokTP[15] in order to carry out one-dimensional hindered rotor treatment (Q_{1D}). Once Autochem identifies the torsional modes, EStokTP prepare scans along them. EStokTP walks along each rotor at increments of thirty degrees from both directions from the energetic minimum geometry. It performs a geometry optimization, using Gaussian [36], at each point while constraining the dihedral

angle. The mode corresponding to that dihedral angle is projected out from the Hessian. An updated list of harmonic and anharmonic frequencies is produced, thereby removing the contribution of the torsional mode from the vibrational partition function. This mode projection procedure was introduced by Green and coworkers[143]. The energy profile obtained during the scan is then used to form a torsional partition function in MESS [41].

MESS is capable of solving a partition function for up to three coupled internal rotations. For these, EStoKTP scans two or three rotors simultaneously to provide a two or three dimensional energy profile. This allows us to compute the multidimensional partition function (Q_{MD}). Vibrational frequencies depend on the torsional angle. To determine the extent that this effects the partition function for these small combustion molecules we use EStoKTP to compute vibrational frequencies at each point on the one, two, or three dimensional profiles. Then in MESS, the fully coupled internal and external rotations are treated semiclassically and the vibrational modes are treated adiabatically to get the adiabatic multidimensional partition function (Q_{AMD}). MESS can solve the rovibrational, anharmonic partition functions alongside both the one-dimensional and multi-dimensional profiles $Q_{1D,anh}$ and $Q_{MD,anh}$. To solve the adiabatic multidimensional, rovibrational, anharmonic partition function we combine these approaches according to:

$$Q_{AMD,anh} = \frac{Q_{MD,anh} Q_{AMD}}{Q_{MD}} \tag{5.4}$$

5.4 Results and Discussion

5.4.1 Fundamental Properties

Rotational Constants

We evaluate the fundamental properties obtained by the various electronic structure methods, namely the rotational constants, frequencies and electronic energies. The rotational constants are a first indicator of the reliability of each geometry. Figure 5.1 charts a box-and-whisker plot for the percentage error of rotational constants obtained with the suite of DFT methods compared to experimental values for 132 constants. The average is represented in two ways: the median percent error is the red bar and the mean percent error is the green square. Outlying data points are shown as grey open circles, where the rejection limit is the data outside of the upper and lower whiskers, which are defined as Q1$-1.5\times$IQR (lower limit) and Q3 + $1.5\times$IQR, where Q1 and Q3 are the quartile percentages and IQR is the interquartile range. In analyzing the performance of methods, both precision and accuracy need be considered. We find that the best representation of the average is the median, because the mean essentially shifts to the position of the original median once the outlying data is rejected from the evaluation (see Table 5.1). The accuracy of each method is, then, determined by its median, and the precision by its IQR and standard deviation. The methods are arranged from left to right on the plot in the order of decreasing accuracy. We see from the numeric breakdown of the box-and-whisker plot, in Table 5.1, that the method considered to be the gold standard, CCSD(T)/cc-pVTZ, is highly accurate for rotational constants with a mean percent error post outlier rejection $\mu = +0.02$. Most surprisingly, the most computationally cheap method, B3LYP/6-31G* has only $\mu = +0.01$. The poorest performers, in terms of both accuracy and preci-

sion are M06-2X/cc-pVTZ and ωB97XD/cc-pVTZ with percents errors ($\mu \pm \sigma$) of -1.49 ± 1.08 and -1.49 ± 0.81.

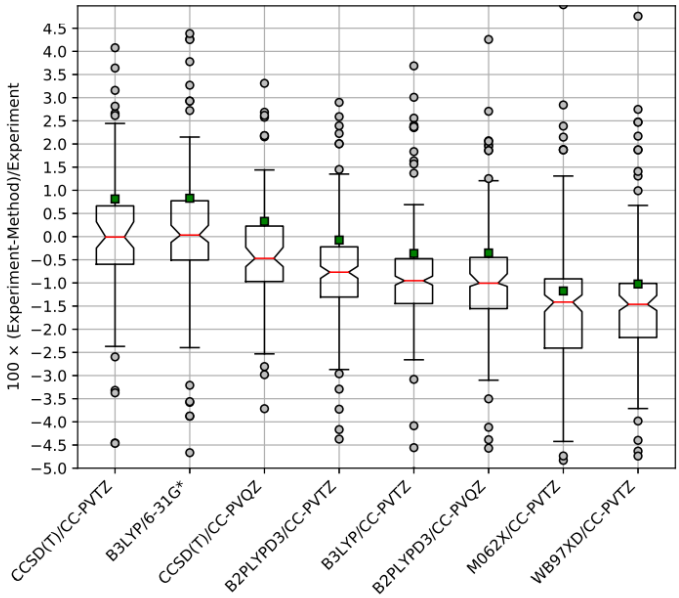

Figure 5.1: Notched box-and-whisker plot of the percentage errors in rotational constants of equilibrium geometries derived from various methods relative to experiment. The red horizontal lines within each box represent the median error, the green squares represent the mean error, and the grey open circles represent outlying data points. The lower and upper edges of the box represent the 25th (Q1) and 75th (Q3) percentiles of the data. The upper and lower whiskers represent outlier rejection limits, respectively defined as Q1 $-$ 1.5 $\times$ IQR (lower limit), and Q3 + 1.5 $\times$ IQR (upper limit)

Table 5.1: Pre- and post-outlier rejection summary statistics for the percentage errors in rotational constants of equilibrium geometries derived from various methods relative to experiment. n is the number of samples in the dataset, μ is the mean error, σ is the standard deviation, $\bar{x}$ is the median error, Q1 and Q3 are the 25th and 75th percentiles respectively, and IQR is the interquartile range.

	Pre-outlier rejection							Post-outlier rejection						
Method	n	μ	σ	$\bar{x}$	Q1	Q3	IQR	n	μ	σ	$\bar{x}$	Q1	Q3	IQR
B2PLYP-D3/cc-pVQZ	132.00	−0.35	6.47	−1.01	−1.56	−0.45	1.11	111.00	−1.01	0.75	−1.01	−1.47	−0.52	0.95
B2PLYP-D3/cc-pVTZ	132.00	−0.07	6.54	−0.77	−1.30	−0.22	1.08	109.00	−0.75	0.75	−0.78	−1.17	−0.37	0.80
B3LYP/6−31G*	132.00	0.83	6.57	0.03	−0.51	0.77	1.28	107.00	0.01	0.79	−0.06	−0.40	0.47	0.87
B3LYP/cc-pVTZ	132.00	−0.36	6.30	−0.95	−1.45	−0.48	0.97	109.00	−1.00	0.63	−0.99	−1.42	−0.56	0.86
CCSD(T)/cc-pVQZ	132.00	0.33	6.65	−0.47	−0.97	0.23	1.20	113.00	−0.45	0.76	−0.49	−0.91	0.09	1.00
CCSD(T)/cc-pVTZ	132.00	0.81	6.71	−0.01	−0.60	0.66	1.26	114.00	0.02	0.89	−0.02	−0.58	0.57	1.15
M062X/cc-pVTZ	132.00	−1.17	6.65	−1.41	−2.41	−0.91	1.50	107.00	−1.49	1.08	−1.38	−1.88	−0.96	0.92
ωB97XD/cc-pVTZ	132.00	−1.02	6.56	−1.46	−2.18	−1.01	1.17	104.00	−1.49	0.81	−1.46	−1.87	−1.07	0.80

Table 5.2: Pre- and post-outlier rejection summary statistics for errors (kJ mol^{-1}) in CCSD(T)-F12b/cc-pVQZ-F12 0 K electronic energies arising from differences in optimised geometries from a given method, relative to the corresponding CCSD(T)/CC-PVQZ geometries. n is the number of samples in the dataset, μ is the mean error, σ is the standard deviation, $\bar{x}$ is the median error, Q1 and Q3 are the 25th and 75th percentiles respectively, and IQR is the interquartile range.

	Pre-outlier rejection							Post-outlier rejection						
Method	n	μ	σ	$\bar{x}$	Q1	Q3	IQR	n	μ	σ	$\bar{x}$	Q1	Q3	IQR
B2PLYP-D3/cc-pVTZ	103.00	−0.12	0.26	−0.06	−0.16	−0.01	0.15	92.00	−0.08	0.09	−0.05	−0.11	−0.01	0.11
B2PLYP-D3/cc-pVQZ	103.00	−0.13	0.20	−0.08	−0.22	−0.02	0.19	96.00	−0.12	0.11	−0.08	−0.18	−0.02	0.16
B3LYP/6−31G*	103.00	−0.58	1.29	−0.37	−0.54	−0.24	0.30	95.00	−0.38	0.21	−0.36	−0.51	−0.24	0.27
B3LYP/cc-pVTZ	103.00	−0.38	0.94	−0.22	−0.41	−0.06	0.35	99.00	−0.24	0.21	−0.22	−0.39	−0.06	0.33
CCSD(T)/cc-pVTZ	103.00	−0.14	0.09	−0.14	−0.18	−0.10	0.09	99.00	−0.14	0.07	−0.14	−0.18	−0.10	0.08
M062X/cc-pVTZ	103.00	−0.67	0.80	−0.52	−0.87	−0.15	0.72	96.00	−0.51	0.43	−0.49	−0.77	−0.11	0.67
ωB97XD/cc-pVTZ	103.00	−0.56	0.59	−0.49	−0.72	−0.17	0.55	98.00	−0.46	0.35	−0.45	−0.69	−0.16	0.53

Electronic Energies

High-level coupled cluster electronic energies when computed on the DFT geometry compared to when computed on CCSD(T)/cc-pVQZ geometries reflects how closely the minimum on the PES between the methods resemble each other. In previous work, we computed CCSD(T)/cc-pVQZ geometries [68] for many of these species. Table 5.2 shows the energy difference in kJ mol^{-1} between F12b-CCSD(T)/cc-pVQZ-F12 electronic energies computed on CCSD(T)/cc-pVQZ geometries and DFT geometries. B2PLYP-D3/cc-PVTZ demonstrates the strongest performance with an error ($\mu \pm \sigma$) of -0.08 ± 0.09 kJ mol^{-1}. When wanting to approach the CCSD(T)/cc-pVQZ minimum geometry, in fact, we see no statistically significant improvement from using CCSD(T)/cc-pVTZ over B2PLYP-D3/cc-pVTZ in this regard.

Vibrational Frequencies

Figure 5.2 shows CCSD(T) harmonic and anharmonic frequencies compared to a set of 353 experimentally obtained values. CCSD(T)/cc-pVTZ, cc-pVQZ, and CBS harmonic frequencies have 2.93, 3.12, and 3.26% mean signed errors with 4.07, 3.72, and 3.59% 1σ deviation, respectively, for the 353 frequencies. With CCSD(T)/cc-pVTZ anharmonic correction, the frequencies at these levels of theory had 0.01, 0.11, and 0.18% mean signed error with 3.33, 3.31, and 3.33 1σ deviation, for a set of 293 frequencies. Several outliers were excluded from this data due to matrix effects on the frequencies or large experimental uncertainties. Figure 5.2 demonstrates that, even at cc-pVTZ, the CCSD(T) anharmonic frequencies are an excellent description for the **ANL1** species.

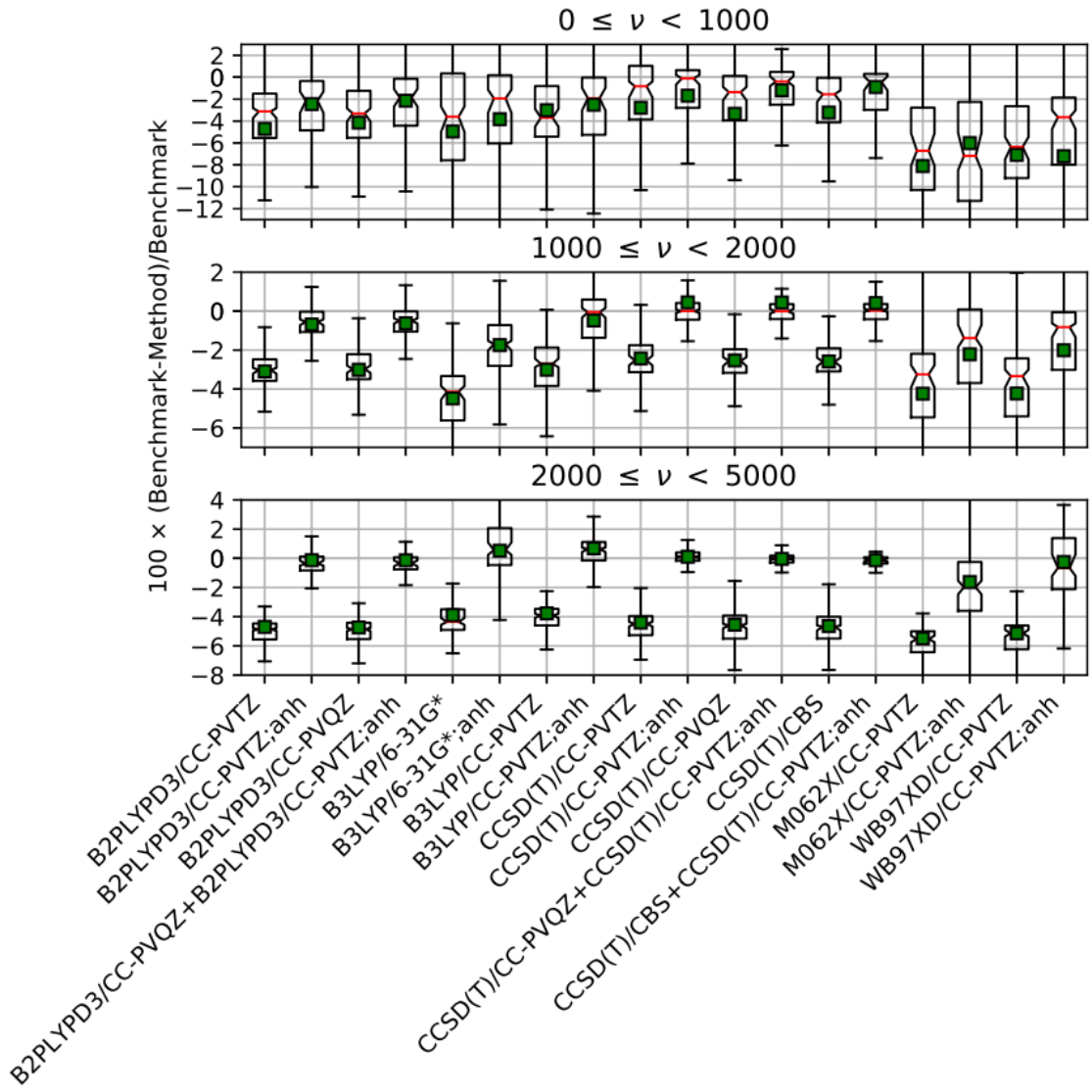

Figure 5.2: Notched box-and-whisker plot of the percentage errors in harmonic and anharmonic frequencies from various methods relative to experiment. The red horizontal lines within each box represent the median error, the green squares represent the mean error, and the grey open circles represent outlying data points. The lower and upper edges of the box represent the 25th (Q1) and 75th (Q3) percentiles of the data. The upper and lower whiskers represent outlier rejection limits, respectively defined as Q1 $-$ 1.5 $\times$ IQR (lower limit), and Q3 + 1.5 $\times$ IQR (upper limit)

Under this assumption, we use the CCSD(T)/CBS harmonic frequencies paired with CCSD(T)/cc-pVTZ anharmonic correction as a larger set of benchmark data, with 579 values, to compare the DFT methods in Figure 5.3 and Table 5.3. Strikingly, the inexpensive B3LYP/6-31G* method peforms better than M06-2X/cc-pVTZ and ωB97XD/cc-pVTZ both in terms of mean unsigned error and standard deviation. B3LYP/6-31G* diverges from CCSD(T)/CBS by $-0.76\pm2.13\%$ in fundamental frequencies compared to the $-1.55\pm3.06\%$ and $-0.82\pm2.40\%$ by M06-2X/cc-pVTZ and ωB97XD/cc-pVTZ. By increasing the basis set to cc-pVTZ from 6-31G* we find that B3LYP improves to have a $-0.47\ \pm1.49\%$ error from CCSD(T)/CBS fundamental frequencies – though it experiences a high number of outlying values than the other methods. We find that B2PLYP-D3/cc-pVTZ, at an intermediate computational cost, achieves $0.31\ \pm\ 0.87\%$ error from the CBS result. This level of accuracy is approaches the $0.15\ \pm\ 0.47\%$ error achieved using CCSD(T)/cc-pVTZ. For the system sizes in the ANL0 set of molecules, B2PLYP-D3/cc-pVTZ is affordable and can be depended on to provide frequencies within 1% of high level results.

5.4.2 Thermochemistry

Uncertainties in vibrational frequencies factor directly into a molecule's partition function. The impact of this uncertainty is obscured during the transformation of the partition function into thermochemical properties. For this reason, we have visualized mean absolute deviations (MAD) of enthalpies, entropies, and heat capacities computed with various approaches to building the partition function. In Figure 5.4, we see the MAD of enthalpies, entropies, and heat capacities from 0-2000 K. For the top row, these are solved from Q_{1D} partition functions built with B2PLYP-D3/cc-pVTZ geometries and harmonic frequencies. The charted deviation is obtained by varying the DFT method used to compute the torsional profiles [B3LYP/6-31G*, B3LYP/cc-pVTZ, ωB97xD/cc-pVTZ, and

M06-2X/cc-pVTZ] and setting the B2PLYP-D3/cc-pVTZ torsional profile as the standard. The mean is across the 153 **ANL0** species that have at least one torsion. The enthalpy shown is ΔH(T) - ΔH(0 K), where T is 300, 500, 1000, and 2000 K. The deviation in the enthalpies grows with temperature. The range in MAD at 0 K is 0.025-0.053 kcal mol^{-1} and grows by over a factor of three to 0.10-0.18 kcal mol^{-1} at 2000 K. Even at 2000 K, however, these deviations are largely within experimental uncertainties. Following the conclusions of our frequency analysis, from the previous section, ωB97xD/cc-pVTZ has the least significant deviation from B2PLYP-D3/cc-pVTZ. This pattern holds for both the entropies and heat capacities, though it becomes less significant at higher temperatures.

The deviation displayed in the bottom row of Figure 5.4 is in the enthalpies, entropies, and heat capacities from Q_{1D} partition functions built with B2PLYP-D3/cc-pVTZ geometries, frequencies, and torsional profiles from those built with B3LYP/6-31G*, B3LYP/cc-pVTZ, ωB97xD/cc-pVTZ, and M06-2X/cc-pVTZ geometries, frequencies, and torsional profiles. With rotational and vibrational partition functions now impacted by choice of DFT method, the range of MAD in enthalpies is twice that found by only changing the torsional profile. At 0 K the deviations in enthalpies range from 0.035-0.048 kcal mol^{-1} and from 0.21-0.32 kcal mol^{-1} at 2000 K. We conclude that, espcially at low temperatures, this sensitivity is minor enough to make B2PLYP-D3/cc-pVTZ a suitable choice for the geometries, frequencies, and torsional profiles – and, advise that ωB97xD/cc-pVTZ is a satisfactory, affordable alternative.

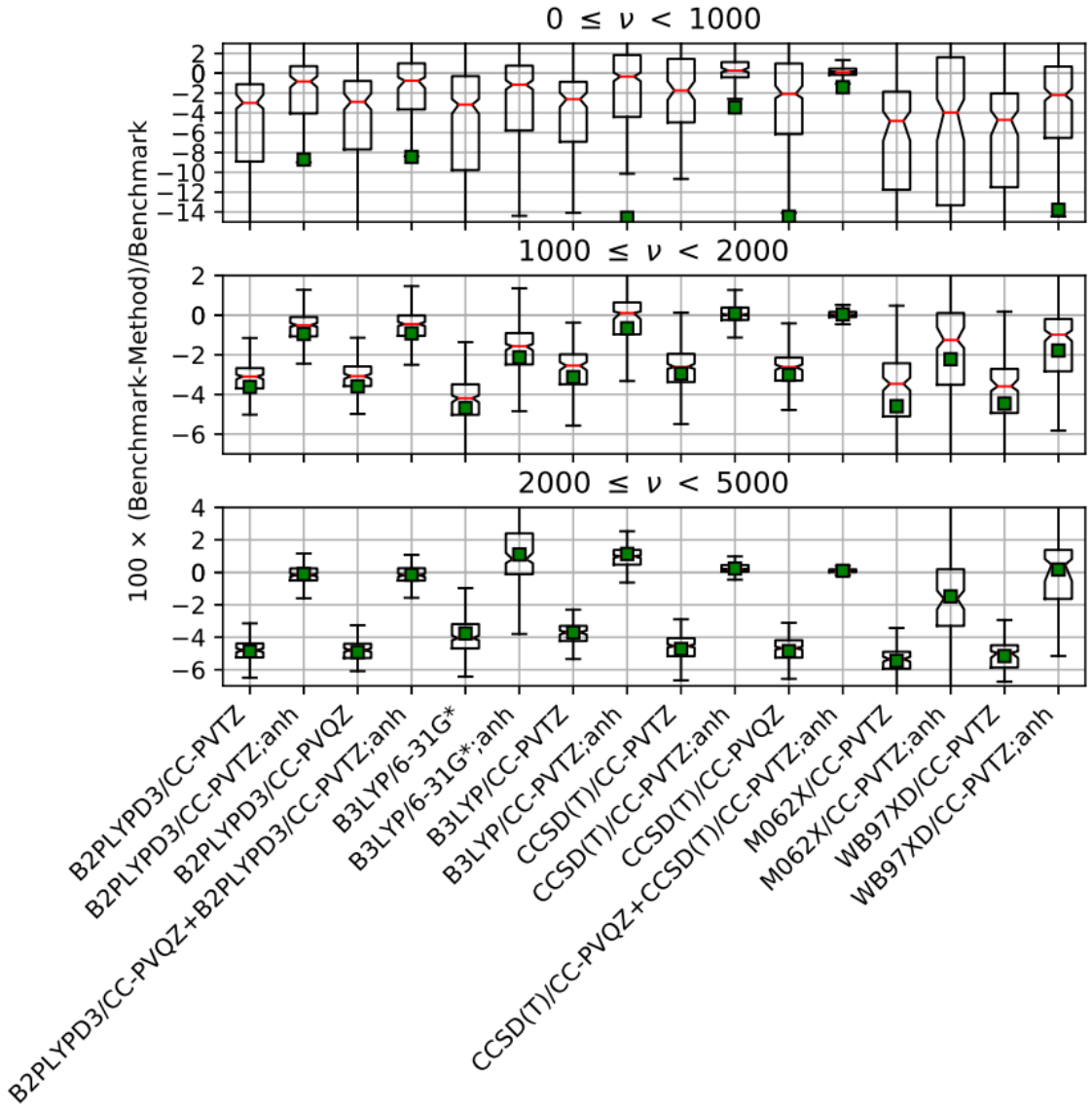

Figure 5.3: Notched box-and-whisker plot of the percentage errors in harmonic and anharmonic frequencies from various methods relative to CCSD(T)/CBS+CCSD(T);anh. The red horizontal lines within each box represent the median error, the green squares represent the mean error, and the grey open circles represent outlying data points. The lower and upper edges of the box represent the 25th (Q1) and 75th (Q3) percentiles of the data. The upper and lower whiskers represent outlier rejection limits, respectively defined as Q1 $-$ 1.5 $\times$ IQR (lower limit), and Q3 + 1.5 $\times$ IQR (upper limit)

Table 5.3: Pre- and post-outlier rejection summary statistics for the percentage errors in harmonic and anharmonic frequencies relative to CCSD(T)/CBS + CCSD(T)/CC-PVTZ;anh. n is the number of samples in the dataset, μ is the mean error, σ is the standard deviation, $\bar{x}$ is the median error, Q1 and Q3 are the 25th and 75th percentiles respectively, and IQR is the interquartile range.

	Pre-outlier rejection							Post-outlier rejection						
Method	n	μ	σ	$\bar{x}$	Q1	Q3	IQR	n	μ	σ	$\bar{x}$	Q1	Q3	IQR
B2PLYP-D3/cc-pvTZ (M1)	579	−8.08	40.34	−3.70	−5.01	−2.61	2.40	493	−3.68	1.61	−3.58	−4.74	−2.68	2.05
B2PLYP-D3/cc-pVQZ (M2)	579	−7.79	36.09	−3.64	−4.99	−2.58	2.41	499	−3.64	1.62	−3.50	−4.72	−2.61	2.11
B3LYP/6−31G* (M3)	579	−8.79	45.84	−4.06	−5.14	−2.76	2.39	477	−3.91	1.53	−4.00	−4.72	−2.99	1.73
B3LYP/cc-pVTZ (M4)	579	−7.05	44.74	−3.23	−4.23	−2.06	2.17	494	−3.10	1.39	−3.15	−3.93	−2.18	1.74
CCSD(T)/cc-pVTZ (M5)	579	−7.15	50.26	−3.15	−4.59	−1.82	2.77	494	−3.14	1.79	−3.11	−4.43	−2.00	2.43
CCSD(T)/cc-pVQZ (M6)	579	−6.61	34.04	−3.20	−4.73	−2.00	2.73	501	−3.29	1.76	−3.15	−4.56	−2.16	2.40
CCSD(T)/CBS (M7)	579	−6.24	25.52	−3.15	−4.83	−2.13	2.70	501	−3.34	1.70	−3.14	−4.63	−2.25	2.38
M062X/cc-pVTZ (M8)	579	−11.07	69.03	−4.88	−6.24	−2.91	3.33	498	−4.56	2.18	−4.66	−5.64	−2.91	2.74
ωB97XD/cc-pVTZ (M9)	579	−9.41	52.39	−4.55	−6.03	−2.94	3.09	503	−4.40	1.97	−4.46	−5.51	−2.94	2.57
M1;anh	579	2.33	79.40	−0.38	−1.13	0.19	1.32	455	−0.34	0.87	−0.31	−0.72	0.10	0.82
M3;anh	579	−7.61	113.81	−0.93	−2.23	0.79	3.02	490	−0.60	2.13	−0.76	−1.82	0.67	2.49
M4;anh	579	14.99	416.88	0.42	−0.97	1.20	2.17	473	0.21	1.49	0.47	−0.44	1.07	1.51
M5;anh	579	−0.91	32.70	0.15	−0.13	0.52	0.65	503	0.18	0.47	0.15	−0.08	0.47	0.56
M8;anh	576	−2.25	84.58	−1.75	−4.38	0.28	4.66	488	−1.89	3.06	−1.55	−3.67	0.16	3.83
M9;anh	579	1.68	94.51	−0.88	−2.79	0.77	3.55	498	−1.08	2.40	−0.82	−2.30	0.52	2.82

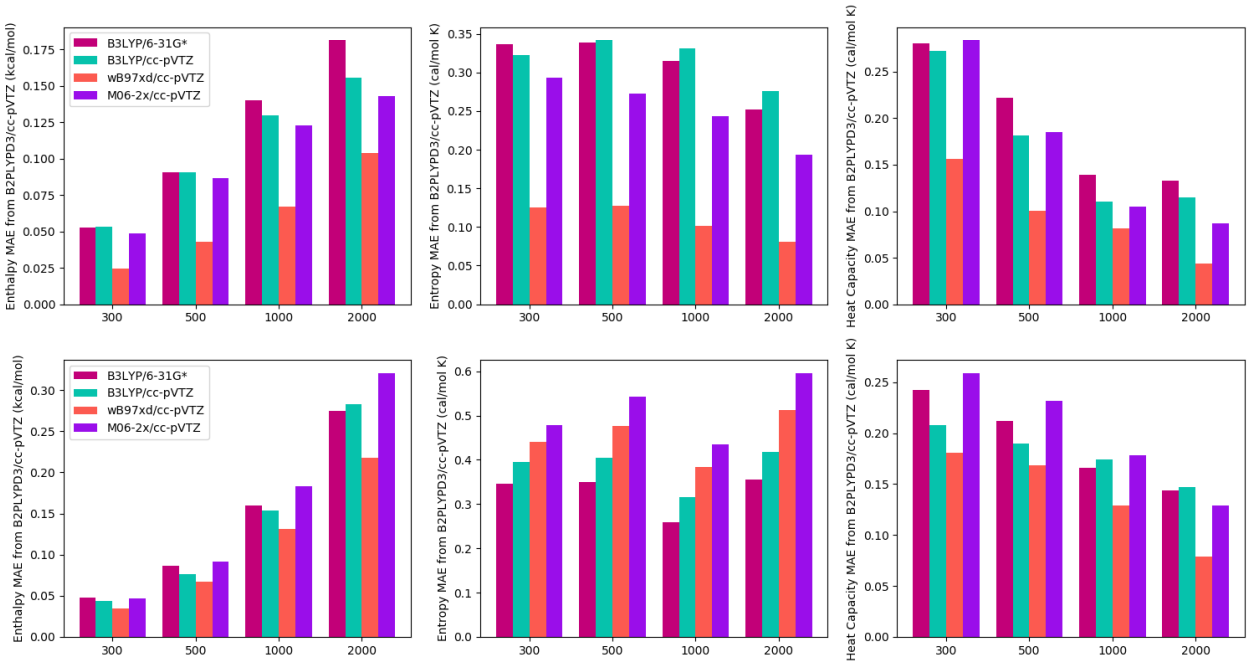

Figure 5.4: Mean absolute deviation (MAD) of enthalpies[a], entropies, and heat capacities from 0-2000 K of (Top) 153[b] species computed with partition functions that have geometry and frequencies at B2PLYP-D3/cc-pVTZ but varied torsional profiles at B3LYP/6-31G*, B3LYP/cc-pVTZ, ωB97xD/cc-pVTZ, and M06-2X/cc-pVTZ from torsional profile at B2PLYP-D3/cc-pVTZ. (Bottom) 302 species computed with partition functions built with B3LYP/6-31G*, B3LYP/cc-pVTZ, ωB97xD/cc-pVTZ, and M06-2X/cc-pVTZ geometries, frequencies, and torsional profiles from those computed with B2PLYP-D3/cc-pVTZ.

[a] Each enthalpy is $\Delta H(T) - \Delta H(0\ K)$

[b] Species have at least one torsional angle

Through the interface in Autochem to MESS, we were able to build partition functions based on the RRHO approximation (Q_{RRHO}), with one-dimensional hindered rotor treatment (Q_{1D}), and with multi-dimensional hindered rotors (Q_{MD}). The multi-dimensional energy profiles ranged from manipulating one rotor at a time to three simultaneously, based on the number of rotors present in each molecule. No molecules in the **ANL0** species set had more than three rotors. By computing frequencies at each point on the multidimensional profile, we can solve an adiabatic multi-dimensional partition function (Q_{AMD}). We built Q_{RRHO}, Q_{1D}, Q_{MD}, and Q_{AMD} with B2PLYP-D3/cc-pVTZ geometries, frequencies, and torsional profiles. The top row of Figure 5.5 shows the mean absolute deviation (MAD) of enthalpies [ΔH(T) - ΔH(0 K)], entropies, and heat capacities from 0-2000 K computed with Q_{RRHO}, Q_{1D}, Q_{MD}, from those computed with Q_{AMD}. This represents 53 species that have at least one torsion. Not surprisingly, QMD has the lowest deviation compared to QRRHO and Q1D. At 1000 K the deviation of the latter two partition functions already produces large uncertainties, with a MAD in enthalpies over 0.5 kcal mol^{-1}. In contrast, the MAD in enthalpies at 2000 K for QMD is only 0.28 kcal mol^{-1}.

By employing second order vibration perturbation theory, computed with B2PLYP-D3/cc-pVTZ we can build rovibrational anharmonic partition functions: $Q_{1D,anh}$ and $Q_{MD,anh}$. The difference between properties calculated with $Q_{1D,anh}$ against Q_{1D}, and $Q_{MD,anh}$ against Q_{MD} are shown in the bottom of Figure 5.5. As temperature increases, anharmonicity becomes increasingly important for enthalpy [ΔH(T) - ΔH(0 K)], entropy, and heat capacity. The enthalpy, at 2000 K, both the 1D and MD harmonic partition functions have a MAD of 1.7 kcal mol^{-1} from the anharmonic partition functions. We note, however, that the MAD between $Q_{1D,anh}$ and Q_{1D} is not noteably higher than the MAD between $Q_{MD,anh}$ and Q_{MD}. We expect that Equation 5.4 should be a good representation of the rovibrational, anharmonic, adiabatic, multidimensional partition function.

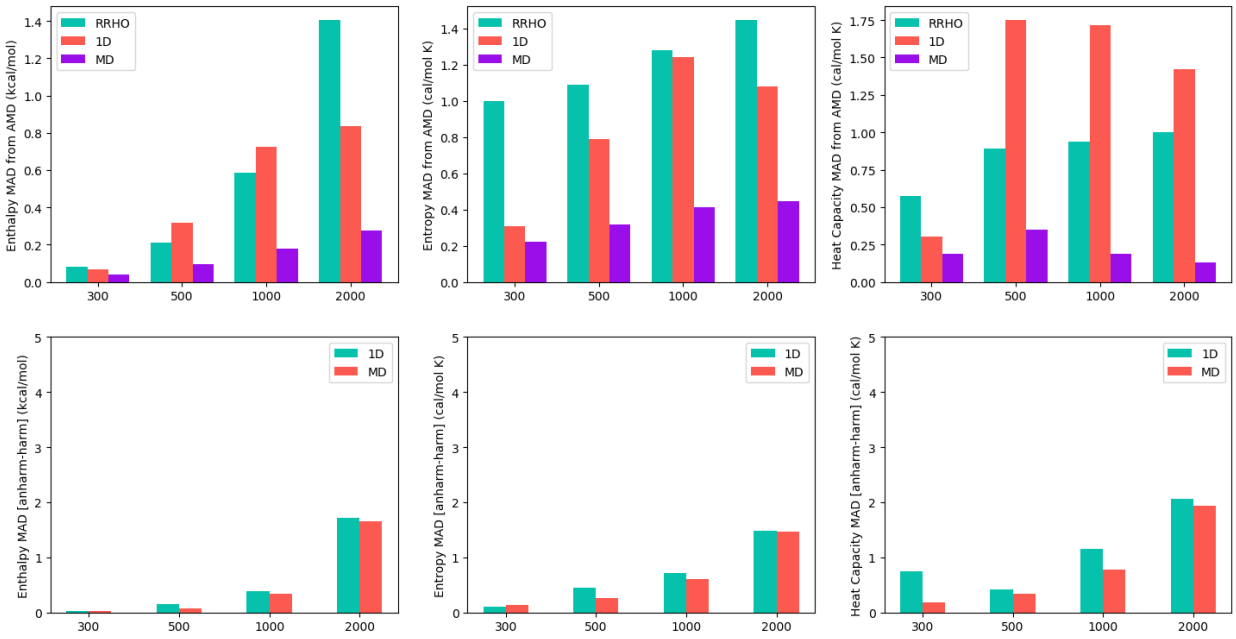

Figure 5.5: Mean average deviation (MAD) of enthalpies, entropies, and heat capacities from 0-2000 K of (Top) 54 species[b] computed with RRHO, 1D, and MD partition functions from those computed with adiabatic MD partition functions, and (Bottom) 262 species computed with anharmonic 1D and MD partitions functions from those computed with harmonic 1D and MD partition functions, respectively.

[a] Each enthalpy is ΔH(T) - ΔH(0 K)

[b] Species have at least one torsional angle

Table 5.4: Enthalpies (Δ H), Entropies (S), Gibb's Free Energies (Δ G), and Heat Capacities (C) for molecules in the **ANL0** set that have zero torsional angles. Properties are derived from anharmonic partition functions and 0 K heats of formation are from the **ANL0** database.

	Δ H (kcal mol^{-1})				S (cal K^{-1}mol^{-1})				Δ G (kcal mol^{-1})				C (cal K^{-1}mol^{-1})			
Species	300 K	500 K	1000 K	2000 K	300 K	500 K	1000 K	2000 K	300 K	500 K	1000 K	2000 K	300 K	500 K	1000 K	2000 K
NH_3	-6.94	96.11			60.71	303.83			-25.16	-55.81			115.35	1047.95		
CH_4	-17.78	-15.56	-5.54	26.64	44.57	50.14	63.55	85.42	-31.15	-40.63	-69.09	-144.20	8.94	13.67	25.60	36.61
H_2O	-57.79	-56.17	-51.70	-40.95	45.02	49.16	55.29	62.66	-71.29	-80.74	-106.99	-166.27	7.97	8.30	9.58	11.71
H_2	0.06	1.45	4.95	12.39	31.08	34.63	39.47	44.60	-9.26	-15.86	-34.52	-76.81	6.95	6.96	7.08	7.80
H	52.13	53.12	55.61	60.57	27.42	29.96	33.40	36.84	43.90	38.14	22.21	-13.11	4.97	4.97	4.97	4.97
C	171.27	172.26	174.75	179.71	35.61	38.15	41.59	45.03	160.59	153.19	133.16	89.65	4.97	4.97	4.97	4.97
CH	142.58	143.98	147.58	155.58	42.30	45.85	50.83	56.34	129.89	121.05	96.75	42.89	6.95	6.99	7.50	8.36
N	112.86	113.86	116.34	121.31	36.64	39.18	42.62	46.06	101.87	94.27	73.72	29.18	4.97	4.97	4.97	4.97
CH_2	93.59	95.27	99.99	111.20	46.45	50.74	57.22	64.92	79.65	69.90	42.76	-18.64	8.15	8.73	10.12	12.03
CH_2	102.67	104.32	109.02	120.53	45.10	49.31	55.75	63.65	89.14	79.67	53.27	-6.76	8.02	8.52	10.28	12.37
NH	85.84	87.23	90.79	98.61	43.25	46.80	51.72	57.11	72.86	63.83	39.07	-15.60	6.95	6.97	7.34	8.22
CH_3	35.09	37.14	43.51	59.99	46.54	51.75	60.45	71.71	21.13	11.27	-16.94	-83.44	9.48	11.04	14.29	18.10
O	59.75	60.79	63.32	68.31	38.43	41.10	44.61	48.06	48.22	40.24	18.71	-27.82	5.39	5.12	5.01	4.98
NH_2	44.51	46.14	50.70	61.81	46.43	50.59	56.85	64.46	30.58	20.85	-6.15	-67.11	7.99	8.38	9.88	12.04
OH	9.19	10.61	14.15	21.83	43.84	47.46	52.37	57.66	-3.96	-13.12	-38.21	-93.48	7.15	7.03	7.24	8.07
C_2	197.10	198.52	202.37	210.84	45.56	49.18	54.47	60.32	183.44	173.93	147.90	90.20	6.98	7.24	8.09	8.69
CCH	135.42	137.09	134.18	-26.54	50.60	54.91	52.16	-46.06	120.24	109.64	82.02	65.59	9.13	6.86	-27.59	-376.73
CN	104.86	106.27	110.04	118.39	48.43	52.02	57.22	62.98	90.33	80.26	52.82	-7.57	6.96	7.14	7.94	8.60
CH_2C	98.59	101.16	111.36	172.75	53.59	60.07	73.68	113.10	82.52	71.12	37.68	-53.45	11.26	14.46	28.21	110.50
CNH	45.94	47.97	53.64	66.62	49.08	54.25	62.05	70.98	31.21	20.85	-8.41	-75.33	9.59	10.58	12.03	13.67
CH_2CH	70.92	73.32	81.61	103.02	55.82	61.87	73.16	87.83	54.18	42.39	8.45	-72.64	10.26	13.66	18.88	23.12
CO	-26.43	-25.03	-21.27	-12.95	47.25	50.83	56.00	61.74	-40.61	-50.44	-77.27	-136.43	6.96	7.11	7.89	8.60
N_2	-0.07	1.33	5.04	13.28	45.80	49.37	54.48	60.16	-13.80	-23.35	-49.44	-107.04	6.96	7.06	7.78	8.54

CH_2N	57.16	59.16	65.82	83.16	53.54	58.60	67.67	79.54	41.10	29.86	-1.85	-75.92	8.93	11.10	15.16	18.94
CHNH	65.00	67.13	74.77	100.41	54.53	59.91	70.25	87.42	48.64	37.18	4.52	-74.43	9.29	12.05	18.44	33.93
CH_3CH	87.47	110.99			72.17	128.91			65.82	46.54			51.50	209.90		
CH_2CH_2	12.36	14.82	24.29	50.58	52.34	58.53	71.36	89.32	-3.35	-14.45	-47.07	-128.05	10.08	14.61	22.40	29.02
HCO	9.83	11.53	16.51	28.15	53.36	57.69	64.51	72.53	-6.17	-17.31	-48.00	-116.91	8.13	8.92	10.82	12.07
COH	52.17	53.93	59.17	71.52	53.76	58.24	65.42	73.91	36.04	24.82	-6.25	-76.30	8.29	9.38	11.34	13.08
NNH	59.49	61.22	66.33	78.67	53.57	57.96	64.97	73.44	43.42	32.24	1.37	-68.21	8.22	9.10	11.21	13.13
CH_2NH	21.11	23.21	31.00	52.56	54.27	59.58	70.13	84.86	4.83	-6.58	-39.13	-117.16	9.00	12.17	18.36	23.87
CH_3N	75.51	77.74	85.95	108.92	54.89	60.48	71.62	87.29	59.05	47.49	14.33	-65.65	9.39	12.88	19.35	25.87
NO	21.80	23.22	27.05	35.49	49.08	52.68	57.96	63.79	7.08	-3.12	-30.91	-92.08	6.97	7.21	8.06	8.68
CH_2O	-26.17	-24.31	-17.96	-0.93	52.24	56.94	65.56	77.21	-41.84	-52.78	-83.52	-155.35	8.41	10.30	14.72	18.67
CHOH	25.98	27.91	34.47	51.46	53.77	58.67	67.59	79.23	9.85	-1.42	-33.13	-107.00	8.63	10.82	14.94	18.46
NHNH	47.76	49.62	56.27	76.59	52.14	56.85	65.85	79.60	32.11	21.19	-9.59	-82.60	8.37	10.43	15.90	24.73
NH_2N	71.73	73.62	79.98	96.87	52.10	56.87	65.52	77.08	56.10	45.18	14.45	-57.29	8.54	10.43	14.66	18.45
HNO	25.52	27.20	32.23	44.49	52.73	57.01	63.89	72.31	9.70	-1.30	-31.66	-100.13	8.05	8.85	11.10	13.04
NOH	51.38	53.17	58.46	70.71	55.15	59.69	66.96	75.39	34.84	23.32	-8.50	-80.06	8.37	9.54	11.37	12.90
CH_3O	5.33	8.78	31.61	197.53	57.00	65.57	95.33	201.82	-11.77	-24.00	-63.73	-206.11	11.73	23.78	72.30	292.99
O_2	-0.10	1.35	5.31	13.93	49.05	52.72	58.18	64.14	-14.81	-25.01	-52.87	-114.35	7.02	7.43	8.31	8.79
NH_2O	15.54	17.71	24.57	42.32	56.50	62.00	71.36	83.50	-1.41	-13.29	-46.80	-124.68	9.96	11.74	15.42	19.69
HO_2	2.87	4.63	9.82	21.93	54.69	59.15	66.27	74.61	-13.53	-24.94	-56.45	-127.28	8.27	9.32	11.21	12.74
c−CCCH	170.98	175.63	248.76	1581.37	57.86	69.21	159.90	984.44	153.62	141.03	88.86	-387.52	12.93	38.59	322.56	2943.91
c−CHCCH	118.47	121.00	130.11	153.98	56.53	62.91	75.31	91.63	101.51	89.55	54.80	-29.29	10.50	14.77	20.82	26.39
CH_2CC	132.57	135.32	143.27	133.54	58.91	65.87	76.91	72.63	114.90	102.38	66.37	-11.71	12.39	15.04	14.25	-51.37
CH_2CCH	83.97	87.35	98.07	123.50	60.71	69.26	83.92	101.45	65.76	52.72	14.15	-79.40	14.79	18.66	23.59	25.94
c−CHCHCH	116.24	119.23	129.99	157.44	60.39	67.91	82.57	101.39	98.12	85.27	47.42	-45.35	12.13	17.55	24.46	29.49
c−CH_2CHC	124.86	127.83	138.45	165.67	60.56	68.05	82.51	101.17	106.69	93.81	55.95	-36.67	12.21	17.33	24.18	29.24
CHCHCH	156.07	159.34	170.46	198.01	63.18	71.43	86.62	105.53	137.11	123.62	83.85	-13.05	13.67	18.73	24.85	29.37
CCO	91.05	93.26	99.61	113.71	55.78	61.38	70.12	79.85	74.32	62.57	29.49	-45.99	10.26	11.67	13.47	14.46
CH_2CN	62.53	65.81	80.07	165.37	59.88	68.15	87.11	142.02	44.57	31.74	-7.03	-118.68	13.68	19.27	40.13	149.95
CHCNH	96.70	112.91			71.77	111.38			75.17	57.22			44.04	128.67		
CH_3CCH	44.76	51.60	122.76	1118.27	61.24	78.07	167.98	788.83	26.39	12.56	-45.22	-459.39	21.18	51.00	280.94	2103.22
CH_2CCH_2	45.33	48.76	60.94	92.99	58.25	66.91	83.47	105.42	27.85	15.31	-22.53	-117.84	14.30	19.82	27.98	34.87

C−CHCH$_2$CH	67.76	70.88	82.89	115.25	58.05	65.89	82.18	104.32	50.34	37.94	0.71	-93.38	12.31	18.77	28.03	35.41
NCNH	81.56	110.36			82.76	152.95			56.73	33.89			74.34	233.04		
CHNN	110.74	113.82	127.66	206.05	59.03	66.78	85.15	135.94	93.03	80.43	42.51	-65.83	12.67	18.27	39.16	130.66
c−CHN$_2$	116.15	118.47	126.03	144.15	58.06	63.93	74.26	86.72	98.73	86.51	51.77	-29.30	10.12	12.97	16.65	19.11
CH$_3$CN	17.48	20.42	30.68	57.66	58.16	65.57	79.52	97.99	0.04	-12.36	-48.84	-138.32	12.60	16.71	23.58	29.28
CH$_3$NC	42.39	45.32	55.53	82.55	58.94	66.35	80.23	98.73	24.70	12.14	-24.70	-114.90	12.75	16.58	23.56	29.37
c−CH$_2$CHN	65.13	67.88	78.22	105.79	58.81	65.71	79.75	98.62	47.49	35.02	-1.53	-91.45	11.11	16.29	24.02	30.06
CH$_2$CHN	86.49	89.54	100.37	128.44	62.43	70.12	84.86	104.09	67.76	54.48	15.51	-79.74	12.68	17.68	24.70	30.52
CH$_2$CHCH$_2$	40.11	43.78	57.52	94.44	61.54	70.76	89.41	114.67	21.64	8.40	-31.89	-134.89	14.67	21.74	31.94	40.44
c−CH$_2$CHCH$_2$	69.72	73.19	87.02	125.54	61.53	70.21	88.94	115.23	51.26	38.08	-1.92	-104.92	13.29	21.18	32.66	43.08
NCO	30.23	32.30	38.48	52.46	54.15	59.39	67.87	77.51	13.99	2.61	-29.39	-102.56	9.42	11.11	13.25	14.40
CNO	93.37	95.57	101.97	116.29	55.05	60.64	69.44	79.32	76.85	65.25	32.53	-42.34	10.24	11.68	13.62	14.74
CH$_2$CO	-11.61	-8.77	0.62	27.08	57.85	65.03	77.82	95.75	-28.96	-41.28	-77.20	-164.42	12.42	15.79	21.43	32.01
CHCOH	24.63	42.25			70.99	113.91			3.34	-14.70			45.74	143.83		
CHCHO	61.68	64.54	74.51	103.82	62.12	69.34	82.89	102.70	43.05	29.87	-8.38	-101.58	12.22	16.24	23.20	36.10
CH$_2$CHNH	49.78	53.07	65.26	97.81	62.07	70.35	86.91	109.17	31.16	17.89	-21.65	-120.53	13.34	19.41	28.22	35.69
CH$_2$NCH$_2$	57.68	61.09	73.48	106.15	61.16	69.75	86.59	108.96	39.33	26.22	-13.10	-111.76	14.02	19.90	28.58	35.49
c−CH$_2$CH$_2$CH$_2$																
NCOH	-3.09	2.17	46.57	555.58	60.36	73.38	130.08	450.03	-21.19	-34.52	-83.51	-344.47	17.74	36.94	163.45	1024.64
NHCO	-28.24	-24.67	-2.69	201.57	58.00	66.93	95.46	224.66	-45.64	-58.13	-98.15	-247.75	13.62	22.80	73.42	397.35
CH$_3$CO	-2.50	0.66	12.45	53.32	64.69	72.64	88.57	115.85	-21.90	-35.66	-76.12	-178.38	13.37	18.17	28.76	55.90
CH$_2$CHO	3.83	6.86	17.65	46.56	61.98	69.62	84.29	104.04	-14.77	-27.95	-66.64	-161.51	12.70	17.47	24.85	32.23
c−CHOCH$_2$	39.41	42.17	52.66	80.57	60.38	67.31	81.55	100.65	21.30	8.52	-28.89	-120.74	11.04	16.48	24.36	30.43
OCO	-94.10	-92.13	-86.15	-72.41	51.13	56.12	64.32	73.79	-109.44	-120.19	-150.47	-219.99	8.91	10.65	12.91	14.25
NNO	19.60	21.61	27.68	41.53	52.55	57.67	65.99	75.54	3.83	-7.22	-38.31	-109.55	9.17	10.88	13.05	14.31
CH$_2$NO	36.69	39.31	48.22	70.73	60.54	67.16	79.29	94.74	18.53	5.74	-31.08	-118.74	11.28	14.83	20.10	24.16
NH$_2$CO	-3.42	-0.57	8.70	32.42	62.61	69.84	82.48	98.71	-22.21	-35.49	-73.79	-165.00	12.68	15.78	20.76	26.23
c−CH$_2$CH$_2$O	-12.54	-9.65	2.01	34.18	57.97	65.21	80.99	102.98	-29.93	-42.25	-78.98	-171.78	11.21	17.66	27.63	35.33
OCOH	-44.11	-41.72	-34.15	-15.63	60.12	66.17	76.53	89.23	-62.14	-74.80	-110.67	-194.09	10.62	13.15	16.67	20.06
OCHO	-31.77	-29.58	-22.60	-6.13	58.27	63.80	73.35	84.69	-49.25	-61.48	-95.95	-175.51	9.73	12.07	15.29	17.26
NHNO	48.29	50.53	57.93	76.61	59.35	65.03	75.12	87.92	30.48	18.02	-17.20	-99.22	9.91	12.52	16.54	20.52
ONO	8.10	10.00	15.75	28.74	57.34	62.18	70.06	79.03	-9.11	-21.09	-54.31	-129.31	8.81	10.24	12.36	13.33

c−CH_2OO	0.28	2.70	11.51	34.29	57.52	63.62	75.60	91.22	-16.98	-29.11	-64.09	-148.14	10.06	14.14	20.22	24.52
ONHO	-10.38	-8.28	-1.20	16.51	56.95	62.24	71.90	84.06	-27.46	-39.40	-73.10	-151.61	9.20	11.76	15.98	18.84
O_3	33.68	35.71	41.78	55.05	57.02	62.15	70.50	79.67	16.58	4.63	-28.72	-104.29	9.20	10.98	12.86	13.48
CHCHCCH	130.23	134.22	147.57	181.85	67.61	77.68	95.90	119.35	109.95	95.38	51.67	-56.85	16.94	22.55	30.01	37.79
c−CHCHCHC	155.96	160.04	173.97	210.00	66.45	76.74	95.73	120.36	136.03	121.68	78.24	-30.72	16.99	23.32	31.40	40.03
NCCN	73.70	76.62	85.12	104.41	57.55	64.96	76.64	89.94	56.43	44.14	8.48	-75.47	13.42	15.52	18.16	19.97
CH_2CCN	99.13	102.68	114.30	144.79	67.04	76.01	91.86	112.67	79.02	64.68	22.44	-80.55	15.56	19.69	26.21	34.45
CHCHCN	106.32	109.80	121.23	149.45	66.31	75.12	90.73	110.10	86.42	72.24	30.50	-70.75	15.05	19.51	25.44	30.13
CHCCHN	118.68	122.24	133.75	162.30	66.82	75.80	91.53	111.11	98.64	84.34	42.22	-59.92	15.46	19.77	25.56	30.82
CH_2CHCCH	69.07	73.17	87.47	124.26	66.36	76.67	96.15	121.36	49.16	34.83	-8.68	-118.47	17.03	23.55	32.52	39.72
CH_2CCCH_2	81.14	105.53			83.98	143.55			55.95	33.76			65.62	193.62		
c−$C(CH_2)CHCH$	92.67	96.67	111.27	149.34	63.11	73.17	93.01	119.09	73.74	60.09	18.26	-88.84	16.06	23.55	33.46	41.32
c−CHCHCHCH	101.83	105.74	120.72	160.25	61.45	71.25	91.59	118.66	83.40	70.12	29.13	-77.06	15.07	23.64	34.61	43.12
CCCHO	112.49	115.61	125.56	151.17	67.89	75.78	89.37	106.86	92.13	77.72	36.19	-62.56	14.05	17.05	22.26	28.80
NCCHN	98.14	101.20	110.80	133.69	65.80	73.53	86.67	102.42	78.40	64.43	24.13	-71.15	13.62	16.74	21.08	24.02
CHCNN	134.77	138.10	148.20	172.33	65.96	74.40	88.25	104.82	114.98	100.90	59.96	-37.30	14.97	18.02	21.94	25.90
CH_2CHCN	44.70	48.28	60.83	93.18	65.28	74.30	91.37	113.55	25.12	11.13	-30.55	-133.92	15.03	20.54	28.62	34.88
c−$CH_2CHCHCH$	78.80	82.96	99.16	142.31	64.05	74.47	96.44	125.98	59.59	45.73	2.72	-109.66	16.00	25.24	37.72	46.88
CHCCHO	31.81	35.29	46.71	75.28	65.65	74.44	90.04	109.63	12.11	-1.94	-43.33	-143.99	15.12	19.43	25.53	30.84
c−CH_2CH_2CHCH	38.42	42.51	59.52	106.68	62.62	72.84	95.84	128.08	19.63	6.09	-36.32	-149.49	15.25	25.47	40.48	51.75
CH_2CHCO	23.24	27.22	40.47	73.61	68.30	78.34	96.41	119.16	2.75	-11.95	-55.95	-164.71	17.01	22.37	29.70	35.49
CH_2CCHO	41.32	45.19	58.53	93.20	69.29	79.06	97.23	120.95	20.53	5.66	-38.69	-148.71	16.49	22.00	30.38	38.00
c−$CH_2CH_2CH_2CH$	54.82	59.83	81.83	166.17	72.46	84.99	114.53	170.51	33.08	17.34	-32.70	-174.84	18.85	31.24	55.89	120.43
OCCO	4.09	7.15	15.87	35.38	61.89	69.66	81.65	95.11	-14.48	-27.68	-65.78	-154.84	14.36	16.07	18.51	20.11
c−$CH_2C(O)CH_2$	4.92	8.88	23.53	61.91	63.66	73.60	93.51	119.80	-14.18	-27.92	-69.98	-177.69	15.83	23.41	33.74	41.60
c−CH_2OCHCH	12.63	16.23	30.39	68.27	62.97	71.97	91.17	117.10	-6.26	-19.76	-60.78	-165.94	13.84	21.90	33.07	41.20
c−$CH_2CH_2CH_2CH_2$	6.69	12.85	47.61	228.81	63.89	79.16	125.09	243.57	-12.47	-26.73	-77.49	-258.34	20.52	41.57	99.39	282.04
CHCOO	86.51	89.87	100.20	125.17	66.58	75.07	89.24	106.36	66.54	52.33	10.97	-87.54	14.85	18.35	22.47	27.24
OCCHO	-15.47	-12.38	-2.60	20.68	67.20	75.01	88.40	104.42	-35.63	-49.89	-90.99	-188.16	13.75	16.96	21.51	24.33
OCCOH	5.04	9.90	35.37	190.62	67.33	79.50	113.04	213.60	-15.16	-29.85	-77.66	-236.58	18.68	30.43	75.75	256.58
c−CH_2CH_2CHO	24.02	28.00	43.93	87.07	66.30	76.26	97.83	127.36	4.13	-10.13	-53.91	-167.65	15.26	24.35	37.49	46.96
c−CH_2CHCH_2O	30.62	34.75	50.99	94.85	67.79	78.16	100.17	130.18	10.28	-4.33	-49.18	-165.52	16.20	25.04	38.10	47.85

$CH_3CH_2CHCH_3$	16.30	22.12	45.55	118.94	78.26	92.87	124.49	174.07	-7.18	-24.32	-78.94	-229.20	23.21	34.98	57.05	90.11
NCOO	67.09	69.88	78.15	96.44	65.36	72.44	83.80	96.44	47.48	33.66	-5.66	-96.44	12.68	15.04	17.55	18.65
c−C(O)OCH_2	-41.08	-37.93	-26.71	1.87	63.14	71.06	86.34	105.94	-60.02	-73.46	-113.05	-210.01	12.95	18.30	25.50	30.71
c−$CH_2CH_2CH_2O$	-18.66	-13.64	14.80	211.72	69.04	81.52	118.93	244.99	-39.37	-54.40	-104.13	-278.25	17.76	33.02	85.58	358.98
c−CH(O)CH_2O	-10.21	-6.41	6.93	40.75	68.79	78.37	96.53	119.73	-30.84	-45.59	-89.60	-198.70	15.81	21.92	30.20	36.34
c−CHOOCH_2	46.07	49.62	62.89	97.33	65.69	74.62	92.65	116.25	26.36	12.31	-29.76	-135.18	14.21	21.15	30.47	37.25
$OCHCH_2O$	-18.69	-14.95	-1.61	33.08	69.06	78.49	96.62	120.38	-39.41	-54.19	-98.23	-207.69	15.64	21.62	30.53	37.80
c−C(O)OO	-39.26	-36.60	-28.21	-8.79	61.10	67.82	79.32	92.69	-57.59	-70.51	-107.53	-194.18	11.58	14.74	18.17	20.33
CH_2CCCCH																
CHCCHCCH	137.78	142.73	158.63	197.54	72.19	84.72	106.45	133.16	116.12	100.38	52.18	-68.77	21.33	27.57	35.07	41.78
CCCCO	146.70	150.58	162.38	192.96	68.23	78.06	94.22	115.03	126.23	111.54	68.16	-37.11	17.61	20.85	26.03	35.76
CH_3CCCCH	98.88	103.96	121.09	165.00	70.60	83.40	106.75	136.83	77.71	62.26	14.34	-108.66	21.65	28.63	38.76	47.62
$CH_2CCHCCH$	104.35	109.44	127.21	175.93	72.55	85.40	109.57	142.74	82.58	66.74	17.64	-109.55	21.29	29.18	40.82	56.09
CH_2CCCCH_2																
$CHCCH_2CCH$	108.64	113.71	131.20	178.37	71.51	84.31	108.10	140.27	87.19	71.56	23.09	-102.17	21.33	28.90	40.01	53.33
c−CHCHCHCHC	123.46	127.95	145.10	189.70	66.86	78.13	101.42	131.99	103.40	88.89	43.67	-74.27	17.26	27.19	39.42	48.26
CHCCCOH																
c−CHCHCHCHN	25.88	30.43	48.50	96.45	64.69	76.09	100.59	133.43	6.47	-7.61	-52.09	-170.42	17.11	27.99	42.06	51.96
OCCCO	-21.39	-17.80	-6.99	17.97	66.30	75.39	90.22	107.42	-41.28	-55.50	-97.21	-196.87	16.16	19.37	23.34	25.95
c−CHCHCHCHO	-8.33	-4.23	12.15	55.45	63.75	74.02	96.22	125.89	-27.46	-41.24	-84.08	-196.34	15.37	25.31	38.09	46.86
CH_3CCCH_2																
CH_3CC																
CCCN	172.80	175.77	184.26	203.49	61.26	68.81	80.48	93.73	154.42	141.37	103.78	16.02	13.82	15.65	18.08	19.93
OC(O)O	-35.78	-33.12	-24.71	-5.13	61.10	67.83	79.34	92.83	-54.11	-67.03	-104.06	-190.78	11.58	14.76	18.23	20.61

Table 5.5: Enthalpies (Δ H), Entropies (S), Gibb's Free Energies (Δ G), and Heat Capacities (C) for molecules in the **ANL0** set that have zero torsional angles. Properties are derived from anharmonic partition functions and 0 K heats of formation are from the **ANL0** database.

	Δ H (kcal mol^{-1})				S (cal K^{-1}mol^{-1})				Δ G (kcal mol^{-1})				C (cal K^{-1}mol^{-1})			
Species	300 K	500 K	1000 K	2000 K	300 K	500 K	1000 K	2000 K	300 K	500 K	1000 K	2000 K	300 K	500 K	1000 K	2000 K
CH_3CH_2	28.66	31.60	42.64	73.26	59.24	66.66	81.61	102.53	10.89	-1.72	-38.97	-131.79	12.26	17.21	26.07	33.77
CH_2NH_2	35.71	38.67	48.53	74.14	58.93	66.39	79.84	97.37	18.03	5.47	-31.31	-120.59	12.80	16.55	22.36	27.95
CH_3NH	42.64	45.19	54.61	80.52	58.82	65.26	78.03	95.74	24.99	12.56	-23.42	-110.96	10.88	14.79	22.16	28.52
CH_3CH_3	-20.17	-17.09	-4.87	30.09	54.87	62.62	79.12	102.98	-36.63	-48.40	-83.99	-175.88	12.51	18.41	29.40	38.76
CH_2OH	-4.06	-1.47	7.03	28.32	57.73	64.30	75.90	90.50	-21.38	-33.61	-68.87	-152.68	11.41	14.46	18.98	22.94
$NHNH_2$	53.32	55.74	63.83	85.04	58.13	64.24	75.26	89.77	35.89	23.62	-11.43	-94.50	10.85	13.43	18.47	23.18
CH_3NH_2	-5.24	-2.53	8.13	38.78	57.25	64.07	78.47	99.37	-22.42	-34.56	-70.34	-159.96	11.12	16.12	25.60	34.33
NHOH	22.46	24.57	31.76	49.80	55.85	61.18	70.96	83.36	5.71	-6.02	-39.20	-116.92	9.27	11.84	16.32	19.03
CH_3OH	-48.09	-45.62	-36.45	-10.91	57.35	63.57	75.99	93.44	-65.30	-77.41	-112.45	-197.79	10.54	14.26	21.70	28.23
NH_2NH_2	23.13	25.81	35.51	62.41	55.81	62.58	75.73	94.09	6.38	-5.48	-40.23	-125.76	11.41	15.41	22.71	30.15
NH_2OH	-10.47	-8.03	0.22	21.59	56.33	62.49	73.73	88.36	-27.37	-39.27	-73.51	-155.13	10.62	13.72	18.71	23.34
OHOH	-32.38	-30.19	-23.39	-6.78	56.02	61.58	70.88	82.28	-49.19	-60.98	-94.27	-171.34	10.03	11.89	14.95	17.84
CH_3CCH_2	60.41	64.06	77.52	114.29	65.52	74.69	92.95	118.08	40.76	26.71	-15.43	-121.87	15.19	21.19	31.57	40.42
CH_3CHCH	63.99	67.68	81.22	117.94	64.96	74.25	92.62	117.72	44.50	30.56	-11.40	-117.50	15.28	21.46	31.61	40.34
CH_3CHN	47.90	51.13	62.85	94.34	64.29	72.43	88.33	109.87	28.62	14.92	-25.48	-125.41	13.65	18.63	27.30	34.33
CH_3CNH	53.39	56.62	68.34	99.81	64.35	72.47	88.39	109.92	34.09	20.38	-20.05	-120.03	13.51	18.67	27.27	34.38
CH_2CNH_2	68.16	71.62	83.66	115.31	65.46	74.19	90.57	112.23	48.52	34.52	-6.92	-109.15	14.67	19.74	27.55	34.65
CH_3CHCH_2	4.67	8.47	23.15	63.92	63.75	73.28	93.15	121.01	-14.45	-28.17	-70.00	-178.11	15.29	22.57	34.81	44.84
CH_3CH_2CH	80.13	84.09	99.03	140.01	69.67	79.64	99.89	127.89	59.23	44.27	-0.86	-115.78	16.17	23.36	35.11	45.12
CNOH	55.37	57.75	65.06	82.06	59.00	65.05	75.07	86.77	37.67	25.23	-10.01	-91.48	10.86	12.96	15.79	17.90
CH_2COH	27.46	30.74	41.53	68.70	64.50	72.79	87.52	106.14	8.11	-5.65	-45.99	-143.58	14.15	18.36	24.13	29.40
CHCHOH	31.39	34.92	46.22	73.35	63.25	72.17	87.66	106.29	12.41	-1.17	-41.43	-139.23	15.04	19.81	24.67	28.93
CH_2CHNH_2	12.94	16.59	30.09	66.33	63.66	72.86	91.19	115.97	-6.16	-19.84	-61.09	-165.61	14.86	21.47	31.35	39.69

CH_3CHNH	9.90	13.29	26.29	62.27	63.31	71.84	89.44	114.03	-9.09	-22.63	-63.14	-165.78	13.89	20.03	30.79	39.53
CH_3NCH_2	19.24	22.67	35.78	72.07	62.66	71.29	89.03	113.84	0.44	-12.98	-53.26	-155.61	14.06	20.22	31.05	39.87
CH_3CHCH_3	20.86	24.89	40.82	85.74	70.51	80.64	102.17	132.85	-0.29	-15.43	-61.35	-179.96	16.30	24.11	38.10	49.57
$CH_3CH_2CH_2$	24.03	28.28	44.46	88.97	69.39	80.07	102.00	132.42	3.21	-11.76	-57.53	-175.88	17.22	25.14	38.17	48.73
$CHNOH$	60.10	63.29	73.25	96.72	62.16	70.22	83.87	100.00	41.46	28.18	-10.62	-103.28	13.84	17.65	21.52	25.09
CH_3CHO	-39.53	-36.43	-24.92	6.41	63.04	70.84	86.44	107.87	-58.44	-71.85	-111.37	-209.34	13.00	18.01	27.04	34.22
CH_2CHOH	-29.85	-26.25	-13.79	17.90	62.03	71.11	88.09	109.81	-48.46	-61.80	-101.88	-201.72	14.97	20.70	28.12	34.23
CH_3COH	14.13	17.46	29.76	62.05	63.38	71.76	88.48	110.59	-4.89	-18.42	-58.71	-159.13	13.62	19.63	28.34	35.08
CH_3OCH	28.53	31.69	43.78	76.12	63.05	71.01	87.40	109.54	9.61	-3.81	-43.62	-142.96	12.96	18.77	28.25	35.14
CH_3CHNH_2	27.87	31.90	46.70	86.85	68.23	78.38	98.45	125.90	7.40	-7.29	-51.75	-164.96	16.81	23.41	34.57	44.00
CH_3CH_2NH	36.06	40.03	54.83	95.28	68.85	78.85	98.92	126.57	15.40	0.60	-44.09	-157.86	16.49	23.22	34.75	44.40
CH_3NHCH_2	36.38	40.33	54.99	95.13	68.29	78.25	98.12	125.56	15.89	1.21	-43.13	-156.00	16.51	23.00	34.46	44.03
$CH_2CH_2NH_2$	37.86	41.93	56.78	97.12	69.75	79.99	100.14	127.71	16.94	1.93	-43.36	-158.30	16.84	23.64	34.60	44.49
$CH_3CH_2CH_3$	-25.19	-20.75	-3.12	46.64	64.85	75.97	99.81	133.79	-44.64	-58.74	-102.93	-220.94	17.58	26.68	42.17	54.95
NH_2CHO	-46.32	-43.21	-32.71	-5.30	63.37	71.23	85.53	104.29	-65.33	-78.83	-118.24	-213.88	13.69	17.39	23.94	29.93
CH_3NO	17.12	20.01	30.25	57.32	62.41	69.71	83.62	102.15	-1.61	-14.85	-53.37	-146.99	12.43	16.51	23.64	29.47
CH_3CHOH	-13.46	-9.76	3.63	39.13	68.74	78.07	96.25	120.55	-34.08	-48.79	-92.62	-201.97	15.47	21.47	30.92	38.70
CH_2CH_2OH	-5.82	-2.00	11.30	46.62	69.99	79.61	97.70	121.87	-26.81	-41.81	-86.40	-197.11	16.49	21.62	30.67	38.60
CH_3CH_2O	-2.95	0.79	14.64	52.52	65.78	75.20	93.98	119.86	-22.68	-36.81	-79.34	-187.19	15.46	21.83	32.42	41.91
CH_3NHCH_3	-3.80	0.37	16.56	62.08	65.58	76.07	97.97	129.05	-23.48	-37.66	-81.41	-196.02	16.85	24.81	38.53	50.48
$CH_3CH_2NH_2$	-11.89	-7.71	8.49	53.80	66.77	77.26	99.19	130.12	-31.92	-46.34	-90.70	-206.45	16.76	24.90	38.43	50.21
$OCHOH$	-90.42	-87.80	-78.39	-54.78	59.53	66.12	78.93	95.16	-108.28	-120.87	-157.32	-245.10	10.92	15.19	21.46	24.84
CH_2OO	24.34	27.08	36.46	59.61	59.84	66.76	79.55	95.45	6.39	-6.30	-43.09	-131.29	11.57	15.67	20.99	24.62
$NHNOH$	18.61	21.46	31.00	55.09	60.06	67.25	80.27	96.78	0.59	-12.16	-49.26	-138.46	12.21	16.06	21.44	26.14
NH_2NO	19.26	22.23	31.77	56.53	63.41	70.92	83.95	100.87	0.24	-13.24	-52.18	-145.20	13.30	16.30	21.42	27.71
CH_3CH_2OH	-56.22	-52.38	-37.78	2.39	67.42	77.08	96.85	124.31	-76.44	-90.91	-134.63	-246.22	15.70	22.68	34.39	44.20
CH_3OCH_3	-43.86	-40.07	-25.71	14.47	64.09	73.62	93.06	120.51	-63.09	-76.88	-118.77	-226.54	15.78	22.13	34.16	44.30
$ONOH$	-19.10	-16.65	-8.81	10.03	60.71	66.91	77.63	90.58	-37.31	-50.10	-86.44	-171.14	10.79	13.55	17.26	19.89
OCH_2OH	-40.33	-37.21	-26.34	1.38	64.85	72.71	87.52	106.52	-59.78	-73.56	-113.86	-211.66	13.08	17.94	24.60	30.00
CH_3OO	3.05	5.88	16.03	42.89	64.58	71.70	85.49	103.89	-16.32	-29.97	-69.46	-164.88	12.05	16.25	23.49	29.18
$OHCH_2OH$	-93.69	-89.87	-77.47	-46.58	63.45	73.08	90.05	111.22	-112.72	-126.41	-167.52	-269.02	16.02	21.55	27.46	33.45
CH_3OOH	-30.51	-27.09	-15.13	16.09	66.14	74.77	91.04	112.42	-50.35	-64.48	-106.17	-208.75	14.60	19.52	27.39	33.92

OOOH	5.73	8.39	15.98	33.20	66.20	72.98	83.41	95.27	-14.13	-28.10	-67.43	-157.35	12.77	13.93	16.15	17.96
OHOOH	-21.70	-18.30	-7.99	14.73	62.71	71.29	85.50	101.16	-40.51	-53.95	-93.48	-187.58	14.62	18.87	21.59	23.74
NCNCH	122.49	125.53	135.07	158.15	66.19	73.88	86.93	102.79	102.63	88.59	48.13	-47.44	13.64	16.61	21.02	24.53
CH_3CHCCH	76.51	81.00	96.87	138.45	71.92	83.24	104.83	133.30	54.93	39.38	-7.96	-128.16	18.77	25.82	36.45	45.06
$CH_2CHCHCH$	86.34	91.04	107.88	150.55	69.04	80.86	103.81	133.08	65.63	50.61	4.07	-115.60	18.82	27.69	38.03	45.97
CH_2CHCHN	72.35	76.63	91.53	129.00	68.62	79.37	99.70	125.40	51.77	36.94	-8.17	-121.81	17.50	24.78	33.54	40.17
CH_3CCCH_3	34.93	39.39	56.08	101.52	67.72	78.96	101.58	132.67	14.61	-0.09	-45.50	-163.82	18.54	26.09	39.25	49.39
CH_2CCHCH_3	38.90	43.53	60.75	107.30	69.90	81.54	104.89	136.74	17.93	2.76	-44.14	-166.17	18.97	27.13	40.24	50.86
CH_3CH_2CCH	39.81	44.54	61.83	107.98	69.46	81.38	104.85	136.44	18.97	3.85	-43.02	-164.89	19.42	27.62	40.10	50.27
$CH_2CHCHCH_2$	26.39	31.19	49.33	96.53	66.58	78.62	103.29	135.62	6.42	-8.12	-53.95	-174.72	18.73	28.88	41.66	51.04
CHCHCHO	44.31	48.31	61.93	95.81	68.62	78.73	97.30	120.55	23.72	8.95	-35.38	-145.30	16.85	22.87	30.46	36.40
$CH_2CHCHCH_3$	33.16	38.11	57.08	108.99	72.11	84.56	110.25	145.74	11.53	-4.16	-53.17	-182.49	19.90	29.45	44.60	57.05
$CH_3CHCHCH_2$	33.08	37.94	56.84	108.72	72.27	84.47	110.07	145.53	11.40	-4.29	-53.22	-182.34	19.18	29.18	44.55	56.98
CH_3CCHCH_3	53.79	58.69	77.15	128.04	74.37	86.70	111.70	146.48	31.48	15.34	-34.55	-164.93	20.32	28.68	43.59	55.91
$CH_3C(CH_2)_2$	33.23	37.67	55.41	105.71	70.52	81.67	105.64	139.98	12.07	-3.17	-50.23	-174.26	17.45	26.78	42.53	55.61
$(CH_3)_2CCH$	56.31	61.39	80.20	131.41	73.09	85.87	111.37	146.39	34.38	18.45	-31.18	-161.36	20.87	29.66	44.02	56.28
$CH_2CHCH_2CH_2$	50.18	55.17	73.92	124.67	76.89	89.46	114.88	149.59	27.11	10.45	-40.96	-174.51	20.31	29.46	43.82	55.53
CH_3CH_2CHCH	59.09	64.14	83.05	134.38	75.11	87.82	113.46	148.56	36.55	20.23	-30.41	-162.73	20.53	29.74	44.23	56.29
CH_3CHCO	-14.99	-11.08	2.90	39.82	68.78	78.65	97.64	122.92	-35.63	-50.40	-94.74	-206.02	16.55	22.50	32.27	40.09
CH_2CHCHO	-15.61	-11.51	3.25	41.21	67.14	77.46	97.53	123.56	-35.75	-50.24	-94.28	-205.92	16.86	23.87	33.76	40.75
$(CH_3)_2CCH_2$	-3.97	1.25	21.22	76.36	70.04	83.13	110.18	147.87	-24.98	-40.32	-88.96	-219.38	20.98	30.90	47.21	60.55
$CH_3CHCHCH_3$	-2.62	2.50	22.29	77.30	70.83	83.69	110.46	148.06	-23.87	-39.34	-88.17	-218.81	20.75	30.36	46.98	60.48
$CH_2CHCH_2CH_3$	0.07	5.22	25.27	80.67	73.63	86.58	113.72	151.59	-22.02	-38.07	-88.45	-222.50	20.53	30.86	47.43	60.85
CCOOH	43.06	46.51	56.64	81.20	70.69	79.47	93.36	110.18	21.85	6.78	-36.73	-139.16	16.12	18.30	21.90	27.23
CH_2CHNO	39.56	43.38	57.13	91.15	66.10	75.70	94.43	117.81	19.74	5.53	-37.30	-144.47	15.61	22.38	31.00	36.04
$CH_3C(O)CH_2$	-7.51	-3.18	12.62	54.37	71.25	82.15	103.60	132.19	-28.88	-44.25	-90.98	-210.02	17.74	25.27	36.52	45.31
$CH_2C(OH)CH_2$	-2.32	2.44	19.03	61.01	70.52	82.52	105.12	133.91	-23.48	-38.82	-86.10	-206.81	19.47	27.56	37.37	45.23
$CH_3C(OH)CH$	21.28	26.24	43.16	86.38	71.28	83.77	106.86	136.44	-0.11	-15.65	-63.70	-186.51	20.60	28.42	37.99	47.46
CH_3CCHOH	21.87	26.55	42.94	84.64	72.33	84.11	106.45	135.04	0.18	-15.50	-63.51	-185.44	19.46	27.05	37.05	45.01
$c-CH(CH_2)OCH_2$	25.45	29.92	46.33	89.24	70.21	81.44	103.75	133.14	4.39	-10.80	-57.42	-177.04	18.00	26.35	37.69	46.63
$CH_2CHCHOH$	-2.36	2.33	18.83	61.18	70.78	82.58	105.05	134.07	-23.59	-38.96	-86.22	-206.96	19.40	27.08	37.48	45.80
CH_2CH_2CHO	5.42	9.81	25.48	66.88	76.08	87.16	108.44	136.79	-17.40	-33.76	-82.96	-206.70	18.79	25.20	36.19	44.98

CH_2OCHCH_2	21.30	25.97	42.39	84.65	72.78	84.55	106.91	135.86	-0.53	-16.30	-64.52	-187.08	19.51	26.93	37.34	45.78
CH_2CHCH_2O	23.82	28.24	44.41	87.03	72.98	84.12	106.08	135.26	1.92	-13.82	-61.67	-183.50	18.18	25.87	37.32	46.28
CH_2CCH_2OH	27.23	31.89	48.01	91.22	76.17	87.93	109.86	139.37	4.38	-12.08	-61.85	-187.53	20.15	26.35	37.09	48.13
$(CH_3)_3C$	12.37	17.54	38.37	97.42	76.97	89.96	118.08	158.41	-10.72	-27.43	-79.71	-219.41	20.71	31.18	50.06	65.13
$(CH_3)_2CHCH_2$	17.69	23.41	45.17	104.56	76.40	90.76	120.25	160.86	-5.23	-21.97	-75.08	-217.17	22.98	33.92	51.11	65.06
$CH_3CH_2CH_2CH_2$	19.07	24.71	46.45	106.29	79.12	93.28	122.73	163.64	-4.67	-21.93	-76.28	-220.98	22.59	33.61	51.31	65.70
OHCHCO	-35.89	-32.28	-20.85	6.73	68.27	77.42	93.06	112.01	-56.37	-70.99	-113.91	-217.28	15.94	19.93	25.09	29.34
OHCCOH	-5.48	-1.81	9.39	36.14	68.46	77.78	93.12	111.51	-26.02	-40.70	-83.73	-186.87	16.71	19.85	24.42	28.36
OCHCHO	-51.02	-47.62	-35.81	-7.17	65.08	73.64	89.74	109.45	-70.54	-84.44	-125.55	-226.07	14.41	19.46	26.43	30.06
CH_3CHNO	27.02	30.94	44.96	81.87	69.38	79.26	98.29	123.58	6.21	-8.69	-53.34	-165.29	16.58	22.51	32.37	39.96
$CH_3C(O)CH_3$	-51.82	-47.43	-30.81	14.66	70.58	81.60	104.11	135.21	-72.99	-88.23	-134.93	-255.76	17.93	25.82	39.15	49.76
$CH_3C(OH)CH_2$	-40.33	-35.32	-17.49	28.76	69.72	82.34	106.60	138.28	-61.25	-76.49	-124.09	-247.80	20.50	29.12	40.69	50.16
$c-CH_2CH_2CH(OH)$	-24.04	-19.45	-1.98	44.89	68.35	79.86	103.56	135.63	-44.54	-59.38	-105.54	-226.37	18.06	27.44	40.67	51.22
$c-CH(CH_3)CH_2O$	-22.34	-17.94	-0.78	46.14	68.69	79.72	102.96	135.05	-42.94	-57.80	-103.74	-223.96	17.34	26.42	40.46	51.35
CH_3CH_2CHO	-44.41	-39.80	-22.92	23.00	72.81	84.43	107.31	138.71	-66.25	-82.01	-130.23	-254.42	19.59	26.56	39.58	50.23
CH_2CHCH_2OH	-29.58	-24.80	-7.63	38.18	73.95	86.00	109.32	140.67	-51.77	-67.80	-116.96	-243.16	20.01	27.57	39.75	50.05
$(CH_3)_2CHCH_3$	-32.09	-26.20	-3.00	61.53	70.86	85.63	117.02	161.12	-53.34	-69.02	-120.02	-260.71	23.24	35.42	55.10	70.96
$CH_3CH_2CH_2CH_3$	-30.20	-24.41	-1.32	63.18	74.50	89.02	120.26	164.33	-52.55	-68.92	-121.57	-265.47	22.73	35.02	55.02	70.96
CH_2COO	26.27	30.22	43.66	76.76	69.26	79.22	97.56	120.29	5.49	-9.39	-53.90	-163.83	16.69	22.53	30.01	35.22
CHCHOOH	53.44	57.81	71.52	104.19	73.26	84.31	103.08	125.53	31.47	15.66	-31.56	-146.87	19.17	24.06	29.91	34.68
$CH_2C(O)OH$	-56.03	-52.05	-38.10	-3.05	67.71	77.73	96.71	120.79	-76.34	-90.91	-134.82	-244.63	16.54	22.89	31.62	37.30
$c-CH(CH_2)OO$	36.30	40.23	53.63	86.58	68.00	77.90	96.19	118.83	15.90	1.28	-42.56	-151.08	16.44	22.50	29.90	34.99
CH_3OCO	-38.39	-34.86	-22.21	10.64	71.39	80.29	97.49	120.02	-59.81	-75.01	-119.70	-229.39	14.96	20.32	29.16	35.25
CH_2OCHO	-37.47	-33.33	-19.16	16.02	71.05	81.49	100.81	124.96	-58.78	-74.07	-119.97	-233.90	17.70	23.57	31.76	37.79
CH_3CH_2NO	10.63	14.87	30.35	71.82	72.93	83.62	104.62	133.00	-11.25	-26.94	-74.28	-194.18	17.80	24.58	36.01	45.24
$CH_3CH(O)CH_3$	-10.91	-5.74	13.69	67.51	72.49	85.49	111.83	148.55	-32.65	-48.48	-98.13	-229.59	20.92	30.48	45.61	60.26
$CH_3CH(OH)CH_2$	-14.69	-9.39	9.45	59.41	77.26	90.61	116.23	150.41	-37.87	-54.70	-106.77	-241.42	22.27	30.47	43.45	54.52
CH_3CH_2CHOH	-18.10	-13.04	5.66	55.81	78.82	91.54	116.92	151.23	-41.74	-58.81	-111.26	-246.65	20.67	29.66	43.47	54.80
CH_3CHCH_2OH	-13.68	-8.74	9.55	59.57	81.19	93.62	118.42	152.61	-38.04	-55.55	-108.87	-245.65	20.82	28.66	42.95	54.99
$CH_2CH_2CH_2OH$	-11.73	-6.69	11.95	61.83	79.95	92.65	117.95	152.09	-35.72	-53.01	-106.00	-242.34	20.84	29.55	43.31	54.45
$CH_3CH_2OCH_2$	-7.38	-2.30	16.56	67.32	76.62	89.40	114.99	149.72	-30.37	-47.00	-98.43	-232.12	20.96	29.74	44.01	55.43
$CH_3CH_2CH_2O$	-7.55	-2.47	16.78	69.73	75.19	87.95	114.05	150.22	-30.11	-46.45	-97.27	-230.70	20.51	30.06	45.23	58.71

$CH_2CH_2OCH_3$	-0.90	4.18	22.72	72.99	78.22	91.03	116.18	150.55	-24.37	-41.33	-93.46	-228.12	21.41	29.36	43.33	55.08
CH_2CHOOH	-9.15	-4.69	10.28	47.55	71.57	82.82	103.25	128.83	-30.62	-46.10	-92.97	-210.11	18.96	25.21	33.50	39.92
$CH_3C(O)OH$	-103.08	-99.20	-84.68	-46.40	68.41	78.15	97.85	124.09	-123.60	-138.28	-182.53	-294.59	15.73	22.82	33.82	41.07
$CH_2C(OH)_2$	-76.40	-71.86	-56.74	-20.05	69.65	81.09	101.77	126.97	-97.29	-112.41	-158.51	-273.98	18.91	25.90	33.31	39.17
CH_3OCHO	-85.63	-81.86	-67.57	-29.43	68.77	78.23	97.60	123.74	-106.26	-120.98	-165.17	-276.91	15.56	22.15	33.54	40.99
$OCHCH_2OH$	-75.61	-70.88	-55.24	-17.74	68.45	80.34	101.82	127.56	-96.14	-111.05	-157.06	-272.86	18.89	27.59	33.99	40.21
CH_3OCOH	-43.77	-39.80	-25.33	13.11	70.38	80.40	100.04	126.36	-64.89	-80.00	-125.38	-239.62	16.61	23.09	33.51	41.71
CH_3CHOO	8.20	11.58	25.31	64.40	64.66	73.14	91.67	118.35	-11.20	-24.99	-66.36	-172.31	13.36	20.45	33.05	43.49
$NH_2C(O)NH_2$	-55.22	-50.71	-35.85	1.15	65.68	77.05	97.35	122.73	-74.93	-89.24	-133.21	-244.32	18.88	25.45	33.06	39.79
$(CH_3)_2CH(OH)$	-64.93	-59.60	-39.47	15.28	74.48	87.88	115.16	152.60	-87.27	-103.53	-154.63	-289.92	21.58	31.50	47.16	60.00
$CH_3CH_2CH_2OH$	-60.86	-55.71	-35.77	19.00	77.22	90.17	117.17	154.62	-84.03	-100.79	-152.94	-290.23	20.65	30.77	47.03	60.13
$CH_3CH_2OCH_3$	-51.96	-46.91	-27.09	27.92	75.41	88.11	114.98	152.57	-74.58	-90.96	-142.06	-277.23	21.23	30.27	47.17	60.40
$OHC(O)O$	-87.81	-84.82	-75.33	-53.58	66.70	74.26	87.27	102.26	-107.82	-121.95	-162.60	-258.10	12.94	16.67	20.46	22.67
$OCHOO$	-25.15	-21.86	-11.24	13.32	67.02	75.35	89.88	106.82	-45.26	-59.53	-101.12	-200.31	14.29	18.42	23.11	25.50
CH_3ONO	-15.68	-11.86	1.12	34.81	69.25	78.91	96.57	119.65	-36.45	-51.31	-95.45	-204.50	16.83	21.36	29.67	36.45
CH_3OON	16.76	20.80	34.68	70.05	69.74	79.94	98.81	123.12	-4.16	-19.17	-64.13	-176.18	17.59	22.65	31.92	37.58
$CH_3N(O)O$	-17.76	-14.42	-2.14	30.08	67.27	75.67	92.34	114.43	-37.94	-52.26	-94.49	-198.77	13.75	19.53	28.38	34.81
$OHCHCH_2OH$	-50.28	-44.88	-28.14	13.66	75.75	89.42	112.32	140.95	-73.00	-89.59	-140.45	-268.24	23.75	29.43	36.99	45.54
CH_3OCHOH	-44.04	-39.18	-23.31	17.70	75.73	88.03	109.66	137.74	-66.76	-83.20	-132.97	-257.77	21.55	26.77	35.92	44.72
$OHCH_2OCH_2$	-43.15	-38.28	-22.17	18.77	75.80	88.13	110.09	138.16	-65.89	-82.34	-132.26	-257.54	21.30	27.12	36.31	44.20
$OHCH_2CH_2O$	-38.91	-33.91	-17.29	25.50	73.11	85.72	108.38	137.68	-60.84	-76.77	-125.68	-249.86	21.02	28.16	37.50	46.73
CH_3OCH_2O	-35.06	-30.69	-14.84	27.38	73.53	84.54	106.06	134.95	-57.12	-72.96	-120.90	-242.53	18.21	25.34	36.73	46.10
CH_3CH_2OO	-5.25	-1.00	14.58	56.03	74.32	85.03	106.18	134.56	-27.55	-43.51	-91.60	-213.08	17.66	24.78	36.13	45.14
$OC(OH)_2$	-146.16	-142.44	-130.32	-101.25	64.05	73.44	90.00	110.02	-165.37	-179.16	-220.32	-321.28	15.81	20.84	26.80	30.34
c−$CH(OH)OO$	-54.20	-50.69	-38.37	-9.40	64.34	73.16	89.98	109.94	-73.50	-87.27	-128.35	-229.28	14.26	20.51	27.12	30.28
$OCHOOH$	-68.80	-64.84	-52.27	-23.07	66.53	76.52	93.79	113.88	-88.76	-103.10	-146.06	-250.83	16.55	22.46	27.02	30.76
$NH_2N(O)O$	1.01	4.37	16.00	46.17	66.03	74.49	90.33	110.97	-18.79	-32.88	-74.33	-175.76	14.14	19.20	26.36	33.47
$NHN(O)OH$	9.85	13.29	25.17	54.14	66.61	75.29	91.49	111.41	-10.13	-24.35	-66.32	-168.68	14.34	19.79	26.54	30.59
NH_2ONO	20.26	24.11	36.23	65.91	68.41	78.15	94.73	115.10	-0.26	-14.97	-58.50	-164.28	17.09	21.09	26.72	31.94
$CH_3N(O)OH$	-6.85	-2.49	12.54	50.86	70.94	81.92	102.41	128.67	-28.13	-43.46	-89.86	-206.48	18.43	24.84	34.02	41.53
CH_3OOCH_3	-28.87	-24.21	-7.18	38.77	73.43	85.16	108.27	139.70	-50.90	-66.79	-115.45	-240.63	19.53	26.99	39.73	50.25
CH_3CH_2OOH	-38.26	-33.65	-16.45	29.40	76.72	88.32	111.67	143.05	-61.28	-77.81	-128.12	-256.71	18.77	27.20	39.95	49.93

$ON(OH)O$	-31.97	-28.91	-18.74	5.26	65.26	73.00	86.90	103.43	-51.55	-65.41	-105.64	-201.59	13.03	17.36	22.36	25.06
$ONOOH$	-3.43	0.31	11.47	37.18	67.39	76.87	92.19	109.88	-23.65	-38.13	-80.72	-182.58	16.81	20.17	23.87	27.21
$C(OH)_3$	-98.28	-93.93	-80.62	-49.35	72.62	83.62	101.88	123.38	-120.07	-135.75	-182.51	-296.11	19.29	23.78	28.71	33.26
$OOCH_2OH$	-39.53	-35.44	-22.26	10.03	72.40	82.75	100.75	122.92	-61.25	-76.81	-123.01	-235.81	17.87	22.68	29.16	34.53
OCH_2OOH	-21.18	-16.92	-3.11	30.36	72.29	83.06	101.95	124.93	-42.87	-58.45	-105.05	-219.51	18.34	23.86	30.42	35.70
CH_3OOO	4.09	7.95	20.69	52.86	72.82	82.61	99.97	122.03	-17.76	-33.35	-79.29	-191.21	17.13	21.45	28.66	34.70
$CH(OH)_3$	-144.24	-139.85	-125.29	-89.18	74.16	85.24	105.13	129.90	-166.49	-182.47	-230.42	-348.98	18.73	24.76	32.38	38.89
$OHCH_2OOH$	-75.00	-70.52	-55.38	-18.13	73.78	85.11	105.78	131.35	-97.14	-113.07	-161.16	-280.83	19.05	25.55	33.67	39.88
CH_3OOOH	-20.42	-15.72	-0.23	37.42	72.48	84.33	105.53	131.37	-42.16	-57.89	-105.75	-225.33	19.85	26.65	34.10	40.33
$OHOOOH$	-10.65	-6.42	6.43	35.16	72.86	83.57	101.23	121.04	-32.51	-48.20	-94.80	-206.92	18.60	23.24	27.23	29.90
$CHCNCH$	134.34	137.97	149.51	178.08	67.55	76.74	92.52	112.11	114.08	99.60	56.99	-46.13	16.01	20.01	25.55	30.89
CH_2CH_2OOH	12.29	16.94	33.06	74.47	79.04	90.77	112.73	141.11	-11.43	-28.45	-79.67	-207.74	19.71	26.58	36.61	44.83

In Tables 5.4 and 5.5 we present enthalpies, entropies, Gibb's free energies, and heat capacities for the species in the **ANL1** and **ANL0** sets of core combustion molecules. These properties are calculated with NASA polynomials which are transformed from the anharmonic, adiabatic, multidimensional partition functions (WILL BE UPDATED, currently not adiabatic). Geometries, frequencies, and torsional profiles are obtained with B2PLYP-D3/cc-pVTZ and the 0 K heats of formation are taken from the **ANL1** and **ANL0** databases, corresponding to Equations 5.2 and 5.1, for Tables 5.4 and 5.5, respectively. In Figure **??** we compare to the ATcT values for 121 species that overlap the databases. Here we find 298 K heats of formation in good agreement, with a mean average deviation of 0.18 kcal mol^{-1} and where only 3% of species differ from ATcT results outside of the sum of the species specific ATcT uncertainty and the general ANL0 0 K heat of formation uncertainty.

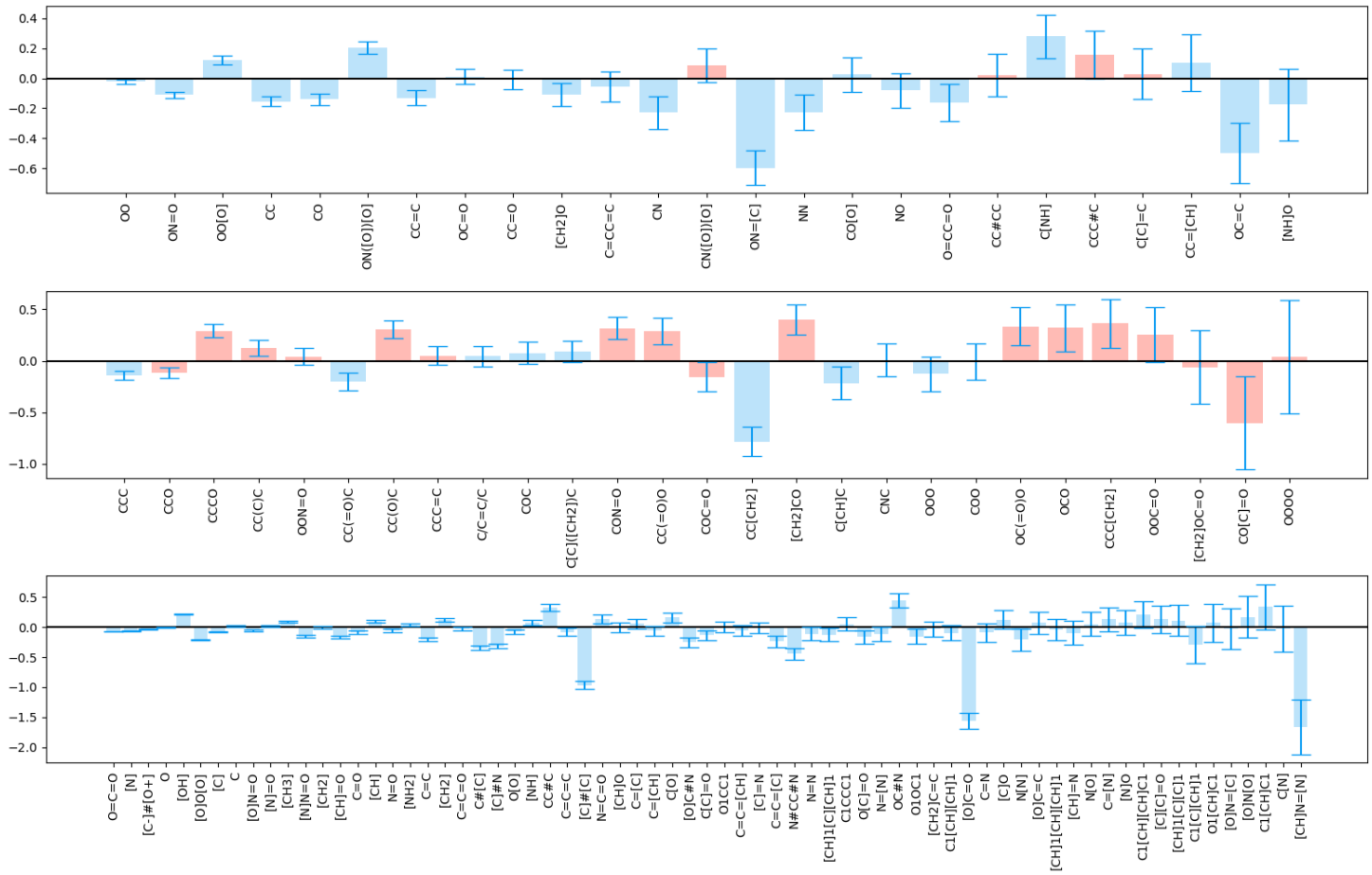

Figure 5.6: The difference (in kcal mol^{-1}) of 298 K Heats of Formation calculated with (Blue) rovibrational, anharmonic, adiabatic multidimensional partition functions and (Red) rovibrational, anharmonic, one-dimensional partition functions from those listed in the ATcT database for (Bottom) 69 molecules containing zero rotors, (Middle) 25 molecules containing one rotor, and (Top) and 27 molecules containing two rotors. Error bars represent the uncertainty reported by the ATcT database for each species.

5.5 Conclusion

We have carried out high-level treatments for the partition functions for 348 core combustion species to provide enthalpies, entropies, heat capacities, and free energies from a range of 0-3000 K. The molecular geometries for each species was established through Monte Carlo sampling and subsequent geometry optimization with an arbitrary DFT method. A torsional energy profile and VPT2 anharmonic vibrational frequency analysis were preformed at the same level of theory. We carried out this procedure using the following five methods on a subset of the species: (M1) B3LYP/6-31G*, (M2) B3LYP/cc-pVTZ, (M3) ωb97xD/cc-pVTZ, (M4) M06-2X/cc-pVTZ, (M5) B2PLYP-D3/cc-pVTZ, and (M6) B2PLYP-D3/cc-pVQZ. We find that B2PLYP-D3/cc-pVTZ has a 0.31 $\pm$0.87% error from CCSD(T)/CBS for 579 anharmonic frequencies, making it a reliable, affordable choice for the larger set of species.

We also examine the mean average deviation between enthalpies, entropies, and heat capacities solved for with RRHO partition functions with one-dimensional hindered rotor treatment (Q_{1D}) and methods M1-M5. We find that at 300 K, these methods predict the temperature dependence of the enthalpy between 0.05 kcal mol^{-1} of B2PLYP-D3/cc-pVTZ. At 2000 K, this value is still under 0.35 kcal mol^{-1}. The thermochemical properties show a greater sensitivity, however, to the treatment of the partition function. At 2000 K, the RRHO partition function has a mean average deviation of over 1.4 kcal mol^{-1} for the temperature dependence of the enthalpy from the adiabatic multidimensional partition function. For the same property, neglecting rovibrational anharmonic effects results in a mean average deviation of 1.7 kcal mol^{-1} at 2000 K. With these considerations we report final results by transforming rovibrational anharmonic, adiabatic multidimensional partition functions into NASA polynomials where our multidimensional energy profiles rotate up to three dihedral

angles simultaneously and our fundamental properties were established with with B2PLYP-D3/cc-pVTZ (M5) and high-level energies from previous work.

5.6 Acknowledgements

This research was supported by the Exascale Computing Project (ECP), Project Number: 17-SC20-SC, a collaborative effort of two U.S. Department of Energy (DOE) organizations, the Office of Science and the National Nuclear Security Administration, responsible for the planning and preparation of a capable exascale ecosystem including software, applications, hardware, advanced system engineering, and early test bed platforms to support the nation's exascale computing imperative. This research was conducted using the Blues and Bebop computing resources, two high-performance computing clusters operated by the Laboratory Computing Resource Center at Argonne National Laboratory. This material is based on work supported by the DOE, Office of Science, Office of Basic Energy Sciences, Division of Chemical Sciences, Geosciences, and Biosciences at Argonne under Contract No. DE-AC02-06CH11357. Several authors of this research also wish to acknowledge additional support. Sarah Elliott gratefully acknowledges support from a DOE Computational Sciences Graduate Fellowship through grant number DE-FG02-97ER25308.

CHAPTER 6

CONCLUSION

Combustion chemistry is an important field of study to atmospheric and fuel science. Both the high temperature and pressure experimental conditions and the transient nature of those species involved in combustion reactions cause combustion studies to heavily depend on computational modeling. This dissertation work features several combustion systems: the formylperoxy radical and two addition reactions of stabilized Criegee intermediates. The quantum, thermochemistry, and kinetics computational methods involved in these studies are tedious. We have developed Autochem, a software that automates these procedures. With Autochem, we carry out AUTOMATED COMPUTATIONAL THERMOCHEMISTRY AND KINETICS FOR COMBUSTION on several fuels and core combustion species.

CHAPTER 1 describes common approaches to solving the thermochemical and kinetic parameters of a combustion system. These parameters are built upon the underlying, fundamental properties of each species that make up the chemical mechanism – including the reactive intermediates and products that a fuel proceeds through during its combustion process. The introductory chapter noted that rotational constants, frequencies, and electronic energies computed with quantum chemistry methods, are the properties that parameterize a molecular partition function. As such,

it described (1-a) several approaches to stationary point localization and geometry optimization including steepest descent and Monte Carlo sampling, (1-b) the computation of harmonic frequencies from the Hessian matrix and the approximation of fundamental frequencies via second order vibrational perturbation theory, and (1-c) the calculation of electronic energies with composite and extrapolation schemes and several high-order corrections to approach full treatment of electron correlation and the complete basis set limit.

CHAPTER 1 then described how to use the fundamental properties that were computed with quantum chemistry methods to parameterize partition functions. The partition functions can be built by (2-a) in the most simple form, taking the Rigid Rotor Harmonic Approximation, (2-b) treating vibrational anharmonicities, and (2-c) treating the torsional motions as hindered rotors. Those partition functions, in turn, determine the temperature dependence of properties like enthalpies, entropies, heat capacities, and Gibb's Free Energies. Additionally, the partition functions go into rate constant computations. CHAPTER 1 explained that computational kinetics also (3-a) determines the mean energy path, (3-b) locates a dividing surface, situationally by using Variational Transition State theory, or treats a barrierless reaction, (3-c) finds any long range transition states such as Van der Waal complexes, (3-d) carries out tunneling corrections, and (3-f) reports pressure dependence through classical trajectory simulations and the Master Equation.

In CHAPTER 2, we see approaches for 1-a through 1-c put into action. We characterized the ground and first excited state of formylperoxy radical, which is an important combustion intermediate in atmospheric chemistry. We used the Focal Point Approach, mentioned in CHAPTER 1, to determine the adiabatic excitation energy and the energy barrier for the energy conversion between the ground state *cis* and *trans* isomers to within 0.10 kcal mol^{-1}. This is well within the uncertainty of both experimental study and that required for kinetic modeling. This study additionally eluci-

dated fundamental frequencies for the ground state, excited state, and five isotopologues of both the *cis* and *trans* ground state isomers. This investigation showcased the ability of computational quantum chemistry to resolve disagreements in experimental studies.

CHAPTER 3 demonstrates computational kinetics (3-a through 3-f) on addition reactions of stabilized Criegee Intermediates. For ammonia addition to formaldehyde oxide and *cis*- and *trans*-acetaldehyde oxide and methanol addition to formaldehyde oxide and acetone oxide, we found a pre-reactive complex along the mean energy path to a transition state structure and to unimolecular product. For all of these structures, the studies used coupled cluster theory to obtain reliable geometries and rotational constants, the Focal Point Approach and high-level corrections to extrapolate electronic energies, and VPT2 anharmonic analysis to compute fundamental frequencies and zero-point vibrational energies. Both studies carried out constrained optimizations along the torsional angles of each structure to obtain torsional energy profiles. With these parameters, they built RRHO partition functions with one-dimensional hindered rotor treatment. They, then, took the steady state approximation and used Canonical Transition State Theory to compute temperature independent rate constants. The frequencies and rate constants agree well with available experimental measurements.

CHAPTER 4 describes Autochem, a combustion chemistry modeling program we are developing, which automates these quantum chemistry, thermochemistry, and kinetics computations. From CHAPTER 2 and CHAPTER 3 it is apparent that to obtain reliable fundamental and thermochemical properties we must carry out large numbers of calculations. This effort is magnified when applied to all of the reactants, products, and intermediates in a combustion mechanism. Autochem must have a careful workflow that considers the reaction types, conditions, and can catch and correct any failures. It must have rigid databasing to keep track of the enormous amount of data produced

during its run, and to save cost in future runs. To be applicable to any arbitrary fuel, it should have wide range of quantum chemistry methods and kinetics treatments. For portability, it should be able to use a variety of softwares and queuing systems. CHAPTER 4 addresses how we have built these considerations into Autochem. It then demonstrates the functionality of the code when used to predict rate constants for the initial stages of pyrolysis for several alkanes, alcohols, and aldehydes. In total it investigated 200 reactions, including abstractions, additions, isomerizations, and addition-eliminations, and produced meaningful rate estimates for 90- 95 % of these. The code also let us look at merging temperatures and branching ratios for these fuel systems and the sensitivity of the results to several electronic structure schemes.

In CHAPTER 5, we focus our attention on the thermochemical properties of core combustion species. We investigated various approaches to building a partition function (as in 2-a though 2-c), automating the computations through the Autochem program. For 150 small species, we contrasted the fundamental properties and resulting thermochemical properties obtained by using six pairings of DFT methods and basis sets against those from coupled cluster methods. Based on the conclusions of these comparisons, we used B2PLYPD3/cc-pVTZ to optimize geometries, obtain vibrational frequencies, and determine torsional energy profiles for the larger set of 348 combustion molecules. We then examined the impact of including anharmonic and rovibrational effects into the partition function, and found that enthalpies at 2000 K had a mean absolute deviation (MAD) of 1.7 kcal mol^{-1} from the enthalpies computed harmonically. At 2000 K, the enthalpies had another 1.4 kcal mol^{-1} MAD when taking the RRHO approximation instead of building adiabatic, multi-dimensional partition functions. These insights motivated us to report final thermochemical properties for the core combustion species with rovibrational, anharmonic, adiabatic, multidimensional partition functions.

Computational quantum chemistry, thermochemistry, and kinetics are, individually, demanding tasks when done at levels that can be considered predictive or within experimental uncertainty. This was demonstrated in CHAPTERS 1- CHAPTERS 3. We have presented our Autochem program in CHAPTERS 4- CHAPTERS 5, which provides a seamless interface for a wide variety of user specified approaches to computing the thermochemical and kinetic parameters for all of the reactions within a combustion mechanism. The studies in CHAPTERS 4- CHAPTERS 5 and Ref. [63] validate that the code is capable of providing both reliable data and important method analysis to the combustion community. Autochem is still under development – we are currently equipping Autochem to handle more exceptional reaction types and preparing it to use more affordable approaches for larger fuels. We are also currently writing documentation to make the program more widely accessible. In its current state, however, it is a power tool for studying combustion. We look forward to future applications of Autochem for AUTOMATED COMPUTATIONAL THERMOCHEMISTRY AND KINETICS FOR COMBUSTION.

BIBLIOGRAPHY

(1) CFOUR, a quantum chemical program package written by J.F. Stanton, J. Gauss, J.D. Watts, P.G. Szalay, R.J. Bartlett with contributions from A.A. Auer, D.E. Bernholdt, O.Christiansen, M.E. Harding, M. Heckert, O. Heun, C. Huber, D. Jonsson, J. Jusélius, W.J. Lauderdale, T. Metzroth, C. Michauk, D.P. O'Neill, D.R. Price, K. Ruud, F. Schiffmann, A. Tajti, M.E. Varner, J. Vázquez and the integral packages: MOLECULE (J. Almlöf and P.R. Taylor), PROPS (P.R. Taylor), ABACUS (T. Helgaker, H.J. Aa. Jensen, P. Jørgensen, and J. Olsen), and ECP routines by A.V. Mitin and C. van Wüllen. For the current version see, http://www.cfour.de.

(2) Agarwal, J.; Simmonett, A.; Schaefer, H. F. *Mol. Phys.* **2012**, *110*, 2419–2427.

(3) Allen, T. L.; Fink, W. H.; Volman, D. H. **1996**, *100*, 5299–5302.

(4) Allen, T. L.; Fink, W. H.; Volman, D. H. *J. Photochem. Photobiol. A* **1995**, *85*, 201–205.

(5) Allinger, N. L.; Fermann, J. T.; Allen, W. D.; Schaefer, H. F. **1997**, *106*, 5143–5150.

(6) Almlöf, J.; Taylor, P. R. *J. Chem. Phys.* **1987**, *86*, 4070–4077.

(7) Aroeira, G. J. R.; Abbott, A. S.; Elliott, S. N.; Turney, J. M.; Schaefer, H. F. *Phys. Chem. Chem. Phys.* **2019**, *21*, 17760–17771.

(8) Bauschlicher, C. W.; Martin, J. M. L.; Taylor, P. R. **1999**, *103*, 7715–7718.

(9) Becke, A. D. *J. Chem. Phys* **1993**, *98*, 5648–5652.

(10) Bhoorasingh, P. L.; Slakman, B. L.; Seyedzadeh Khanshan, F.; Cain, J. Y.; West, R. H. *The Journal of Physical Chemistry A* **2017**, *121*, 6896–6904.

(11) Bomble, Y. J.; Stanton, J. F.; Kállay, M.; Gauss, J. **2005**, *123*, 054101.

(12) Brown, R. *J. Res. Natl. Bur. Stand* **1981**, *86*, 357–359.

(13) Caravan, R. L.; Khan, M. A. H.; Rotavera, B.; Papajak, E.; Antonov, I. O.; Chen, M.-W.; Au, K.; Chao, W.; Osborn, D. L.; Lin, J. J.-M.; Percival, C. J.; Shallcross, D. E.; Taatjes, C. A. *Faraday Discuss.* **2017**, *200*, 313–330.

(14) Cavallotti, C.; Pelucchi, M.; Georgievskii, Y.; Klippenstein, S. *Journal of chemical theory and computation* **2018**, *15*, 1122–1145.

(15) Cavallotti, C.; Pelucchi, M.; Georgievskii, Y.; Klippenstein, S. J. *J. Chem. Theory Comput.* **2019**, *15*, 1122–1145.

(16) Chai, J.-D.; Head-Gordon, M. *Physical Chemistry Chemical Physics* **2008**, *10*, 6615–6620.

(17) Chiles, R. A.; Dykstra, C. E. *J. Chem. Phys.* **1981**, *74*, 4544–4556.

(18) Copan, A. V.; Elliott, S. N.; Keceli, M.; Moore, K. B.; Klippenstein, S. J.; Georgievskii, Y.; Cavallotti, C. PACChem, `https://github.com/PACChem`, 2019.

(19) Copan, A. V.; Schaefer, H. F.; Agarwal, J. *Mol. Phys.* **2015**, DOI: `10.1080/00268976.2015.1063729`.

(20) Copan, A. V.; Wiens, A. E.; Nowara, E. M.; Schaefer, H. F.; Agarwal, J. **2015**, *142* 054303, 055303.

(21) Cówan, R. D.; Griffin, D. C. **1976**, *66*, 1010–1014.

(22) Császár, A. G.; Demaison, J., Boggs, J. E., Császár, A. G., Eds.; CRC Press: Boca Raton, FL, 2011, pp 233–262.

(23) Császár, A. G.; Allen, W. D.; Schaefer, H. F. **1998**, *108*, 9751–9764.

(24) Curran, H. J. *Proceedings of the Combustion Institute* **2019**, *37*, 57–81.

(25) Davidson, E. R.; Ishikawa, Y.; Malli, G. L. **1981**, *84*, 226–227.

(26) Dixon, D. J.; Skirrow, G., *The Gas Phase Combustion of Aldehydes*; Bamford, C. H., Tipper, C. F. H., Eds.; Comprehensive Chemical Kinetics, Vol. 17; Elsevier: Amsterdam, 1977, pp 369–439.

(27) Drozd, G. T.; Donahue, N. M. *The Journal of Physical Chemistry A* **2011**, *115*, PMID: 21476564, 4381–4387.

(28) Dunning, T. H. **1989**, *90*, 1007–1023.

(29) East, A. L. L.; Allen, W. D. **1993**, *99*, 4638–4650.

(30) Fang, Y.; Liu, F.; Klippenstein, S. J.; Lester, M. I. *The Journal of Chemical Physics* **2016**, *145*, 044312.

(31) Finlayson, B. J.; Pitts, J. N. J. *Science* **1976**, *192*, 111–119.

(32) Finlayson-Pitts, B.; Pitts, J., *Chemistry of the Upper and Lower Atmosphere: Theory, Experiments, and Applications*; Elsevier Science: 1999.

(33) Francisco, J. S.; Willams, I. H. **1988**, *92*, 5347–5352.

(34) Francisco, J. S.; Eisfeld, W. *The Journal of Physical Chemistry A* **2009**, *113*, 7593–7600.

(35) Francl, M. M.; Pietro, W. J.; Hehre, W. J.; Binkley, J. S.; Gordon, M. S.; DeFrees, D. J.; Pople, J. A. *The Journal of Chemical Physics* **1982**, *77*, 3654–3665.

(36) Frisch, M. J. et al. Gaussian~16 Revision B.01, Gaussian Inc. Wallingford CT, 2016.

(37) Frisch, M.; Trucks, G.; Schlegel, H.; Scuseria, G.; Robb, M.; Cheeseman, J.; Scalmani, G.; Barone, V.; Mennucci, B.; Petersson, G., et al. *Wallingford CT* **2009**, *93*.

(38) Froman, N. .; Froman, P., *Wkb approximation, contributions to the theory*; 12; North-Holland Publishing Company: Amsterdam, 1965, pp 5955–5976.

(39) Fukui, K. *J. Phys. Chem.* **1970**, *74*, 4161–4163.

(40) Gao, C. W.; Allen, J. W.; Green, W. H.; West, R. H. *Computer Physics Communications* **2016**, *203*, 212–225.

(41) Georgievskii, Y.; Miller, J. A.; Burke, M. P.; Klippenstein, S. J. *J. Phys. Chem. A* **2013**, *117*, PMID: 24053787, 12146–12154.

(42) Gonzales, J. M.; Pak, C.; Cox, R. S.; Allen, W. D.; Schaefer, H. F.; Császár, A. G.; Tarczay, G. **2003**, *9*, 2173–2192.

(43) Grambow, C. A.; Jamal, A.; Li, Y.-P.; Green, W. H.; Zador, J.; Suleimanov, Y. V. *Journal of the American Chemical Society* **2018**, *140*, 1035–1048.

(44) Greenwald, E. E.; North, S. W.; Georgievskii, Y.; Klippenstein, S. J. *J. Phys. Chem. A* **2005**, *109*, PMID: 16833939, 6031–6044.

(45) Grimme, S.; Antony, J.; Ehrlich, S.; Krieg, H. *The Journal of chemical physics* **2010**, *132*, 154104.

(46) Handy, N. C.; Yamaguchi, Y.; Schaefer, H. F. **1986**, *84*, 4481–4484.

(47) Harding, M. E.; Metzroth, T.; Gauss, J.; Auer, A. A. **2008**, *4*, 64–74.

(48) Harding, M. E.; Vázquez, J.; Ruscic, B.; Wilson, A. K.; Gauss, J.; Stanton, J. F. *J. Chem. Phys.* **2008**, *128*, 114111.

(49) Held, T.; Marchese, A.; Dryer, F. *Combustion Science and Technology* **1997**, *123*, 107–146.

(50) Hsu, C. C.; Mebel, A. M.; Lin, M. C. **1996**, *105*, 2346–2352.

(51) Huang, H.-L.; Chao, W.; Lin, J. J.-M. *Proceedings of the National Academy of Sciences* **2015**, *112*, 10857–10862.

(52) Ignatyev, I. S.; Xie, Y.; Allen, W. D.; Schaefer, H. F. **1997**, *107*, 141–155.

(53) Ilias, M.; Saue, T. *J. Chem. Phys.* **2007**, *126*, 064102.

(54) Jacox, M. E. *Chem. Phys.* **1994**, *189*, 149–170.

(55) Jacox, M. E. *Chem. Soc. Rev.* **2002**, *31*, 108–115.

(56) Jaeger, H. M.; Schaefer, H. F.; Demaison, J.; Császár, A. G.; Allen, W. D. *J. Chem. Theory Comput.* **2010**, *6*, PMID: 26616770, 3066–3078.

(57) Jasper, A. W.; Gruey, Z. B.; Harding, L. B.; Georgievskii, Y.; Klippenstein, S. J.; Wagner, A. F. *J. Phys. Chem. A* **2018**, *122*, PMID: 29356534, 1727–1740.

(58) Jayatilaka, D.; Lee, T. J. **1993**, *98*, 9734–9747.

(59) Johnston, H. S.; Heicklen, J. *J. Phys. Chem.* **1962**, *66*, 532–533.

(60) Kállay, M.; Gauss, J. **2005**, *123*, 214105.

(61) Kállay, M.; Gauss, J. **2008**, *129*, 144101.

(62) Karton, A.; Daon, S.; Martin, J. M. *Chem. Phys. Lett.* **2011**, *510*, 165–178.

(63) Keceli, M.; N. Elliott, S.; Li, Y.-P.; S. Johnson, M.; Cavallotti, C.; Georgievskii, Y.; H. Green, W.; Pelucchi, M.; M. Wozniak, J.; W. Jasper, A.; J. Klippenstein, S. *Proc. Combustion Institute* **2018**, DOI: 10.1016/j.proci.2018.07.113.

(64) Keçeli, M.; Elliott, S. N.; Li, Y.-P.; Johnson, M. S.; Cavallotti, C.; Georgievskii, Y.; Green, W. H.; Pelucchi, M.; Wozniak, J. M.; Jasper, A. W., et al. *Proceedings of the Combustion Institute* **2019**, *37*, 363–371.

(65) Klippenstein, S.; Cavollotti, C. In *Mathematical Modelling of Gas-Phase Complex Reaction Systems: Pyrolysis and Combustion, Volume 45*, Ranzi, T. F. F. M. E., Ed.; Elsevier: 2019; Chapter 1.

(66) Klippenstein, S. J. *Proceedings of the Combustion Institute* **2017**, *36*, 77–111.

(67) Klippenstein, S. J.; Cavallotti, C. In *Computer Aided Chemical Engineering*; Elsevier: 2019; Vol. 45, pp 115–167.

(68) Klippenstein, S. J.; Harding, L. B.; Ruscic, B. *J. Phys. Chem. A* **2017**, *121*, PMID: 28758403, 6580–6602.

(69) Knizia, G.; Adler, T. B.; Werner, H.-J. *The Journal of chemical physics* **2009**, *130*, 054104.

(70) Kuchitsu, K.; Demaison, J., Hargittai, I., Eds.; Oxford University Press: Oxford, UK, 1992, pp 14–43.

(71) Kutzelnigg, W.; Ottschofski, E. **1995**, *102*, 1752–1757.

(72) Kuwata, K. T.; Guinn, E. J.; Hermes, M. R.; Fernandez, J. A.; Mathison, J. M.; Huang, K. *The Journal of Physical Chemistry A* **2015**, *119*, PMID: 26397164, 10316–10335.

(73) Langford, A. O.; Moore, C. B. *J. Chem. Phys.* **1984**, *80*, 4211–4221.

(74) Lee, C.; Yang, W.; Parr, R. *Phys. Rev, vol. B* **1988**, *37*, 785–789.

(75) Lee, T. J.; Taylor, P. R. **1989**, *36*, 199–207.

(76) Li, A.; Xie, D.; Dawes, R.; Jasper, A. W.; Ma, J.; Guo, H. *J. Chem. Phys.* **2010**, *133*, 144306.

(77) Liu, Y.; Yin, C.; Smith, M. C.; Liu, S.; Chen, M.; Zhou, X.; Xiao, C.; Dai, D.; Lin, J. J.-M.; Takahashi, K.; Dong, W.; Yang, X. *Phys. Chem. Chem. Phys.* **2018**, *20*, 29669–29676.

(78) Maeda, S.; Harabuchi, Y. *Journal of chemical theory and computation* **2019**, *15*, 2111–2115.

(79) Mauldin Iii, R.; Berndt, T.; Sipilä, M.; Paasonen, P.; Petäjä, T.; Kim, S.; Kurtén, T.; Stratmann, F.; Kerminen, V.-M.; Kulmala, M. *Nature* **2012**, *488*, 193.

(80) McCaslin, L.; Stanton, J. *Mol. Phys.* **2013**, *111*, 1492–1496.

(81) McGillen, M. R.; Curchod, B. F.; Chhantyal-Pun, R.; Beames, J. M.; Watson, N.; Khan, M. A. H.; McMahon, L.; Shallcross, D. E.; Orr-Ewing, A. J. *ACS Earth Sp. Chem.* **2017**, *1*, 664–672.

(82) Miller, J. A.; Kee, R. J.; Westbrook, C. K. *Annu. Rev. Phys. Chem.* **1990**, *41*, 345–387.

(83) Jr-Min Lin, J.; Chao, W. *Chem. Soc. Rev.* **2017**, *46*, 7483–7497.

(84) Misiewicz, J. P.; Elliott, S. N.; Moore, K. B.; Schaefer, H. F. *J. Chem. Chem. Phys.* **2018**, *20*, 7479–7491.

(85) Misiewicz, J. P.; Elliott, S. N.; Moore, K. B.; Schaefer, H. F. *Phys. Chem. Chem. Phys.* **2018**, *20*, 7479–7491.

(86) N. Elliott, S.; B. Moore, K.; V. Copan, A.; Keceli, M.; Cavallotti, C.; Georgievskii, Y.; F. Schaefer, H.; J. Klippenstein, S. Automated Theoretical Chemical Kinetics: Exploring the Initial Stages of Pyrolysis, unpublished, N.D.

(87) Neeb, P.; Sauer, F.; Horie, O.; Moortgat, G. K. *Atmospheric Environment* **1997**, *31*, 1417–1423.

(88) Neese, F. *WIREs: Comp. Mol. Sci.* **2012**, *2*, 73–78.

(89) Nguyen, T. L.; Lee, H.; Matthews, D. A.; McCarthy, M. C.; Stanton, J. F. *The Journal of Physical Chemistry A* **2015**, *119*, PMID: 25945650, 5524–5533.

(90) Nguyen, T. B. et al. *Phys. Chem. Chem. Phys.* **2016**, *18*, 10241–10254.

(91) Nickel, A. A.; Lanorio, J. G.; Ervin, K. M. **2013**, *117*, 1021–1029.

(92) Nielsen, H. H. **1951**, *23*, 90–136.

(93) Nielsen, H. H. *Phys. Rev.* **1941**, *60*, 794–810.

(94) O'Boyle, N. M.; Banck, M.; James, C. A.; Morley, C.; Vandermeersch, T.; Hutchison, G. R. *Journal of cheminformatics* **2011**, *3*, 33.

(95) O'Boyle, N. M.; Banck, M.; James, C. A.; Morley, C.; Vandermeersch, T.; Hutchison, G. R. *J. Cheminformatics* **2011**, *3*, 33.

(96) Okabe, H., *Photochemistry of Small Molecules*; Wiley Interscience Publications; Wiley: New York, 1978.

(97) Orlando, J. J.; Tyndall, G. S. **2012**, *41*, 6294–6317.

(98) Osborn, D. L.; Taatjes, C. A. *International Reviews in Physical Chemistry* **2015**, *34*, 309–360.

(99) Osif, T. L.; Heicklen, J. **1976**, *80*, 1526–1531.

(100) Parrish, R. M. et al. *J. Chem. Theory Comput.* **2017**, *13*, PMID: 28489372, 3185–3197.

(101) Percival, C. J. et al. *Faraday Discuss.* **2013**, *165*, 45–73.

(102) Peukert, S. L.; Sivaramakrishnan, R.; Michael, J. V. *Proceedings of the Combustion Institute* **2015**, *35*, 171–179.

(103) Peukert, S.; Labbe, N.; Sivaramakrishnan, R.; Michael, J. *The Journal of Physical Chemistry A* **2013**, *117*, 10228–10238.

(104) Pollard, R. T., *Hydrocarbons*; Bamford, C., Tipper, C., Eds.; Comprehensive Chemical Kinetics, Vol. 17; Elsevier: Amsterdam, 1977, pp 249–367.

(105) Radford, H. E.; Evenson, K. M.; Howard, C. J. **1974**, *60*, 3178–3183.

(106) Ramabhadran, R. O.; Raghavachari, K. *J. Phys. Chem. A* **2012**, *116*, PMID: 22571375, 7531–7537.

(107) Ranzi, E.; Dente, M.; Pierucci, S.; Biardi, G. *Industrial & Engineering Chemistry Fundamentals* **1983**, *22*, 132–139.

(108) Ruscic, B.; Pinzon, R. E.; von Laszewski, G.; Kodeboyina, D.; Burcat, A.; Leahy, D.; Montoy, D.; Wagner, A. F. *J. Phys.: Conference Series* **2005**, *16*, 561–570.

(109) Sadezky, A.; Winterhalter, R.; Kanawati, B.; Römpp, A.; Spengler, B.; Mellouki, A.; Le Bras, G.; Chaimbault, P.; Moortgat, G. K. *Atmospheric Chemistry and Physics* **2008**, *8*, 2667–2699.

(110) Schuurman, M. S.; Muir, S. R.; Allen, W. D.; Schaefer, H. F. **2004**, *120*, 11586–11599.

(111) Sellers, H.; Pulay, P. **1984**, *103*, 463–465.

(112) Sellers, H.; Pulay, P. *Chem. Phys. Lett.* **1984**, *103*, 463–465.

(113) Sivaramakrishnan, R.; Su, M.-C.; Michael, J.; Klippenstein, S.; Harding, L.; Ruscic, B. *The Journal of Physical Chemistry A* **2010**, *114*, 9425–9439.

(114) Skodje, R. T.; Truhlar, D. G.; Garrett, B. C. *J. Chem. Phys.* **1982**, *77*, 5955–5976.

(115) Stanton, J. F.; Gauss, J.; Bartlett, R. J. *J. Chem. Phys.* **1992**, *97*, 5554–5559.

(116) Strickler, S. J.; Berg, R. A. **1962**, *37*, 814–822.

(117) Szalay, P. G.; Gauss, J.; Stanton, J. F. **1998**, *100*, 5–11.

(118) Taatjes, C. A. *Annual Review of Physical Chemistry* **2017**, *68*, PMID: 28463651, 183–207.

(119) Taatjes, C. A.; Shallcross, D. E.; Percival, C. J. *Phys. Chem. Chem. Phys.* **2014**, *16*, 1704–1718.

(120) Tadayon, S. V.; Foreman, E. S.; Murray, C. *J. Phys. Chem. A* **2018**, *122*, 258–268.

(121) Takeno, T., *Turbulence and Molecular Processes in Combustion*; Elsevier Science: 2012.

(122) Truhlar, D. G.; Garrett, B. C.; Klippenstein, S. J. *J. Phys. Chem.* **1996**, *100*, 12771–12800.

(123) Tso, T. L.; Diem, M.; Lee, E. K. C. **1982**, *91*, 339–342.

(124) Tso, T. L.; Lee, E. K. C. **1984**, *88*, 5465–5474.

(125) Tso, T.-L.; Lee, E. K. C. **1984**, *88*, 5475–5482.

(126) Tuckett, R.; Freedman, P.; Jones, W. *Mol. Phys.* **1979**, *37*, 403–408.

(127) Turney, J. M. et al. **2011**, *2*, 556–565.

(128) Van de Vijver, R.; Van Geem, K. M.; Marin, G. B. *Proceedings of the Combustion Institute* **2019**, *37*, 283–290.

(129) Van de Vijver, R.; Zádor, J. *Submitted*.

(130) Vereecken, L.; Nguyen, H. M. T. *International Journal of Chemical Kinetics* **2017**, *49*, 752–760.

(131) Vereecken, L.; Francisco, J. S. *Chem. Soc. Rev.* **2012**, *41*, 6259–6293.

(132) Villano, S. M.; Eyet, N.; Wren, S. W.; Ellison, G. B.; Bierbaum, V. M.; Lineberger, W. C. **2010**, *114*, 191–200.

(133) Volman, D. H. *J. Photochem. Photobiol. A* **1996**, *100*, 1–3.

(134) Warnatz, J. In *Symposium (International) on Combustion*, 1985; Vol. 20, pp 845–856.

(135) Watson, N. A. I.; Black, J. A.; Stonelake, T. M.; Knowles, P. J.; Beames, J. M. *J. Phys. Chem. A* **2018**, *123*, 218–229.

(136) Watts, J. D.; Urban, M.; Bartlett, R. J. **1995**, *90*, 341–355.

(137) Werner, H.; Knowles, P.

(138) Wheeler, S. E.; Houk, K. N.; Schleyer, P. v. R.; Allen, W. D. *J. Amer. Chem. Soc.* **2009**, *131*, PMID: 19182999, 2547–2560.

(139) Whitehead, R.; Handy, N. *J. Molec. Spec.* **1975**, *55*, 356–373.

(140) Wigner, E. *Phys. Rev.* **1932**, *40*, 749–759.

(141) Winter, N. W.; Goddard, W. A. **1975**, *33*, 25–29.

(142) Wolf, A.; Reiher, M.; Hess, B. A. *J. Chem. Phys.* **2002**, *117*, 9215–9226.

(143) Wong, B.; Green, W. *Mol. Phys.* **2005**, *103*, 1027–1034.

(144) Woolley, H. W. *J. Res. Natl. Bur. Stand.* **1956**, *56*, 105–110.

(145) Xu, R.; Wang, K.; Banerjee, S.; Shao, J.; Parise, T.; Zhu, Y.; Wang, S.; Movaghar, A.; Lee, D. J.; Zhao, R., et al. *Combustion and Flame* **2018**, *193*, 520–537.

(146) Yang, H.-C.; Chen, H.-L.; Ho, J.-J. **2006**, *774*, 35–41.

(147) Yang, R.; Yu, L.; Zeng, A.; Zhou, M. **2004**, *108*, 4228–4231.

(148) Zádor, J.; Taatjes, C. A.; Fernandes, R. X. **2011**, *37*, 371–421.

(149) Zhao, Y.; Truhlar, D. G. *Accounts of chemical research* **2008**, *41*, 157–167.

(150) Zhao, Y.; Wingen, L. M.; Perraud, V.; Greaves, J.; Finlayson-Pitts, B. J. *Phys. Chem. Chem. Phys.* **2015**, *17*, 12500–12514.

(151) Zimmerman, P. *Journal of chemical theory and computation* **2013**, *9*, 3043–3050.